AN ABSTRACT OF THE THESIS OF

Paul R. Collins for the degree of Doctor of Philosophy in Chemistry presented on December 7, 1983

Title: An Investigation of the Clustering of Divalent Cations in Potassium Bromide

Abstract approved: Redacted for privacy
William J. Fredericks

Single crystals of pure KBr, and KBr doped with Ca^{2+}, Cd^{2+}, and Pb^{2+}, were grown for this investigation. Distribution coefficients were estimated from the melt and crystal dopant concentrations.

The Mandel'shtam-Brillouin scattering spectrum of the crystals was resolved, and the ratio of the unshifted central peak to the MB shifted peaks was used as a measure of the scattering power of the crystals. For a perfect, pure crystal this ratio would be the Landau-Placzek intrinsic ratio. The effects of thermal history on the scattering power of the doped crystals were investigated; a slow anneal to room temperature greatly increased the scattering. From the scattering concentration dependence of the annealed crystals, solubilities

were determined. Precipitate particle sizes were estimated assuming two different models for the precipitate particles: Model 1, the pure halide; and Model 2, a collection of divalent cation-vacancy pairs.

Ultraviolet absorption spectra of the crystals were measured. Ultraviolet irradiation of the crystals produced electron-hole and electron-excess centers typical of higher-energy X- and γ-irradiation.

The distribution coefficients were estimated to be Ca: >0.13, Cd: >.0025, and Pb: >.0185.

From the frequency shift of the MB spectrum, the transverse and longitudinal <1,1,0> velocities were determined: $\rho v_L^2 = 26.0 \pm 0.7$GPa; $\rho v_{T_2}^2 = 5.1 \pm 0.3$GPa .

The solubilities estimated at near room temperature were Ca: 360 ± 30 mppm, Cd: 0.7 ± 0.5 mppm, and Pb: 86 ± 5 mppm.

Oscillator strengths for the A-, B-, and C-bands of Pb^{2+} in KBr were determined by peak deconvolution, yielding A-band: 0.12 ± .01, B-band: 0.04, and C-band: 0.77 .

An Investigation of the Clustering of Divalent Cations in Potassium Bromide

by

Paul R. Collins

A THESIS

submitted to

Oregon State University

in partial fulfillment of
the requirements for the
degree of

Doctor of Philosophy

Completed December 7, 1983

Commencement June 1984

APPROVED:

Redacted for privacy

Professor of Chemistry in charge of major

Redacted for privacy

Chairman of the department of Chemistry

Redacted for privacy

Dean of Graduate School

Date thesis is presented December 7, 1983

Typed by Frances Gallivan for Paul R. Collins

TABLE OF CONTENTS

LIST OF FIGURES

LIST OF TABLES

AN INVESTIGATION OF THE CLUSTERING OF DIVALENT CATIONS IN POTASSIUM BROMIDE

I. INTRODUCTION

The light absorption spectrum of potassium bromide consists of electronic absorptions for wavelengths less than ~200 nm, and vibrational absorptions for wavelengths greater than ~20 μm. Between ~200 nm and ~20 μm, KBr is nominally transparent. The causes and character of light transmission losses in this wavelength regime is the subject of this thesis.

Transmission losses are caused by either scattering or absorption. Impurity absorption is discussed in chapter VII, and an interesting optical bleaching effect in Pb^{2+} doped samples is presented. The bulk of this thesis, however, is devoted to scattering losses.

The phenomenon of light scattering has been extensively studied for many years. Rayleigh (1871) gave the first complete description of light scattering from small particles. Rayleigh correctly attributed the blue color of the sky to an inverse fourth power dependence of the scattering intensity on wavelength. In 1908 Mie developed an exact mathematical treatment for the scattering from arbitrarily sized spherical particles.

For larger particles, Rayleigh's inverse fourth power law was shown to be invalid. Among others, books by Van de Hulst (1957), Fabelinski (1968), and Kerker (1969) are useful references on particle scattering; the rudiments of the theories are discussed in chapter III of this thesis.

Inelastic scattering processes were discovered during the 1920's. An inelastic scattering process involves an energy transfer between the incident light and the scattering material; this results in a frequency shift in the scattered light. Mandel'shtam (1924) and Brillouin (1922) predicted inelastic scattering from acoustic waves in fluids and solids. The Mandel'shtam-Brillouin (MB) scattering was observed in 1930 by Gross.

The frequency shifts associated with MB scattering in solids can yield accurate values for elastic constants. Benedek and Fritsch (1966) give a detailed discussion of the angular dependence of the MB shift and of the methodology for determining elastic constants in cubic crystals. Four MB spectral studies have been performed on KBr: Matsura and Miyazawa (1973), Kaplan et al. (1970), Braul and Plint (1981), and Cummins and Schoen (1972). Some useful reviews of MB scattering are given by Cummins and Schoen (1972), Vacher and Boyer (1972), and Fabelinski and Chistyi (1976).

In addition to the MB scattering in KBr, there is also a very small amount of intrinsic elastic scattering. The relative magnitudes of these two intrinsic scattering mechanisms is discussed in chapter III. In real crystals, however, nearly all elastic scattering is from extrinsic sources (i.e., impurities and defects).

Figure 1.1 shows a two-dimensional view of a KBr lattice with some common defects and a substituted divalent cation. The point defects shown are cation and anion vacancies (a Schottky defect). These are the most common defects in alkali-halides. Also shown is a line dislocation; this defect extends in a line above and below the plane of the paper.

Vacancy defects and substituted divalent ions have an excess charge relative to the expected charge at that site; cation vacancies have an excess negative charge, and anion vacancies and divalent cations have an excess positive charge. In order to maintain charge neutrality in the crystal, the number of excess positively charged species must equal the number of excess negatively charged species. This means that for every substitutional divalent cation, a charge-compensating cation vacancy must be formed. Further, the charged nature of these species causes positive and negative species to attract one another, resulting in the formation of impurity vacancy complexes. Larger numbers of impurities and

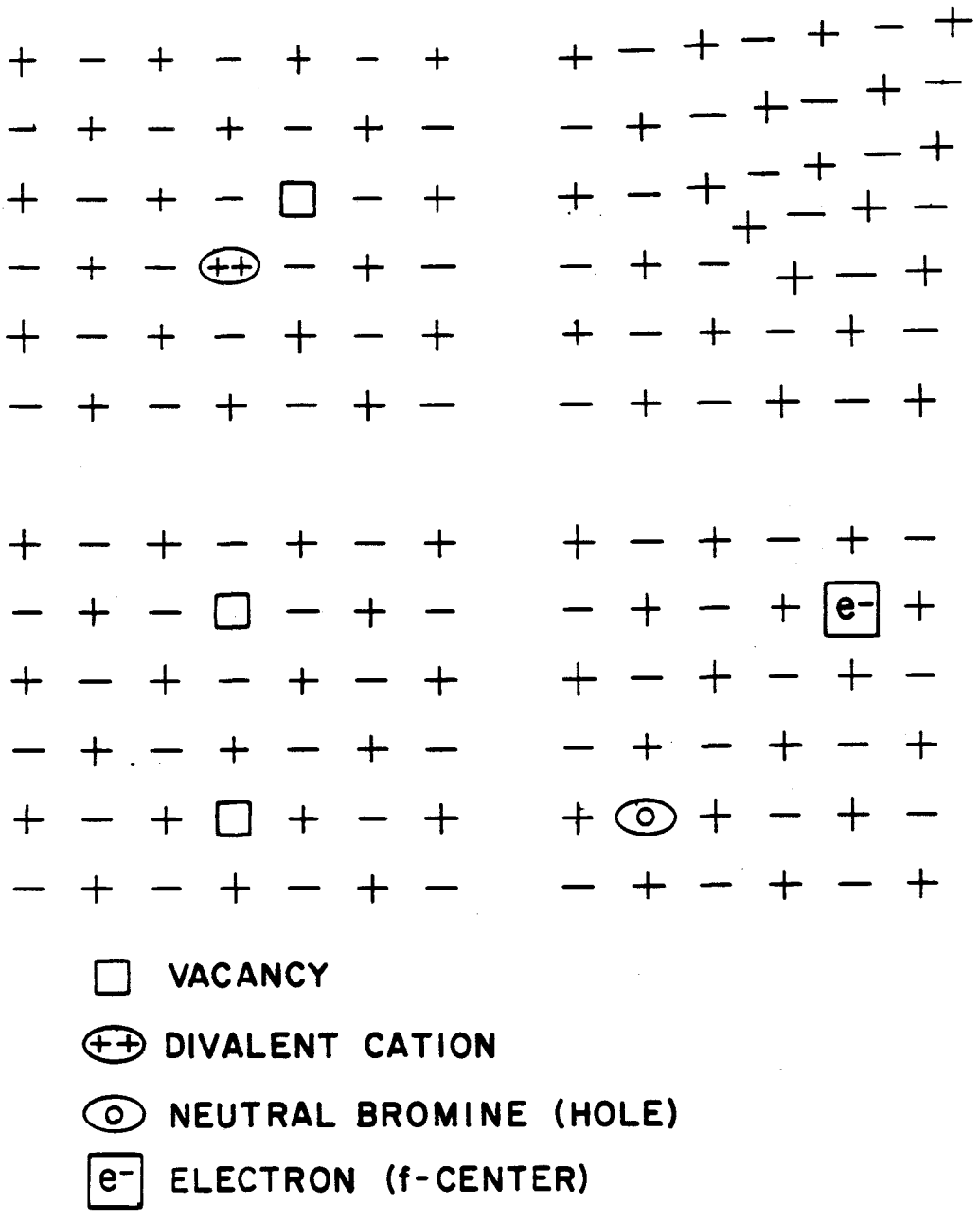

Figure 1.1 Defects in alkali halides.

vacancies can form larger clusters and precipitate as separate phases within the lattice.

The extrinsic scattering in alkali-halides has been studied since the early 1950's. In these early studies, the extrinsic scattering was about 40 times greater than the intrinsic scattering in nominally pure alkali-halides. Humphreys-Owen (1954) explained these results in terms of an intrinsic mosaic dislocation network. Theimer and Plint (1958) performed detailed calculations of the scattering power of dislocation lines and point defects. Theimer and Plint conjectured that point defects were not homogeneously distributed, but were located preferentially along, or near, dislocation lines. These ideas were further examined by Plint et al. (1958) and Theimer et al. (1960). Bansiger and Schneider (1962) performed scattering studies on NaCl and KCl doped with divalent cations; they also reached the conclusion that a semi-organized dislocation network existed in the crystals, and that divalent cation impurities tended to lie along these dislocation lines. Plint and Sibley (1965) also studied doped NaCl and KCl crystals. They investigated the anisotropic character of scattering centers by analyzing depolarization ratios of the scattered light. Their results indicated that Pb^{2+} ions tended to lie along dislocation lines, while

Ca^{2+} and Sr^{2+} ions tended to form spherical precipitate particles.

In most of these early studies, commercially grown crystals were used; when crystals were locally grown, no special purification was performed. In the present investigation, special purification and growth procecures were used to produce the crystals. Thus a scattering intensity closer to the intrinsic level could be attained.

In previous studies of extrinsic scattering, the scattered light has not been spectrally resolved. In studies of MB scattering, the MB peak intensities and frequency shifts have been extensively investigated, but the extrinsic elastic scattering has largely been ignored. In the present study, the MB scattering has been resolved, and the ratio of the elastic scattering to the MB scattering has been calculated. The MB scattering provides an internal intensity standard for the determination of the elastic scattering intensity.

II. CRYSTAL GROWTH AND SAMPLE PREPARATION

A. Materials Preparation

Both pure KBr cyrstals and KBr crystals intentionally doped with divalent cation impurities were grown for this study. In this thesis, the term dopant will refer to an intentionally added impurity; the term impurity will refer to an unintentional contamination of the KBr.

The divalent cation dopants were Ca^{2+}, Cd^{2+}, and Pb^{2+}. All of these were added as the dibromide salt. The $CdBr_2$ and $CaBr_2$ salts were produced from Mallinckrodt S.L. grade $CdCO_3$ and $CaCO_3$. The carbonates were added to aqueous HBr which was produced from gaseous HBr and 16 M-ohm deionized water. The slightly acidic solution was then evaporated to dryness in a teflon coated vacuum oven. The resulting cadmium salt was recrystallized from water.

The highly deliquescent nature of $CaBr_2$ resulted in the production of a hydrated form. From Ca atomic emission analysis, the hydration formula after vacuum drying at ~120°C was $CaBr_2 \cdot 3.7\ H_2O$.

The $PbBr_2$ used was BDH® 98% $PbBr_2$ which was recrystallized three times from ~0.01M HBr. The $PbBr_2$ was

then dried in the teflon-coated vacuum oven.

The KBr used for these crystals was Baker Analyzed®. For the doped crystals, no special purification of the KBr was performed. The KBr used in the pure crystals was purified using selective ion filters to remove aliovalent cation and anion impurities. This procedure is discussed by Fredericks (1978).

B. Crystal Growth

The KBr crystals were pulled from the melt using the Czochralski method. The growth apparatus is described by Fredericks (1977). The essential features are shown in Figure 2.1.

The KBr was contained in a quartz crucible 6½ cm in diameter and 8 cm in height. The crucible rested on a quartz stand inside a large quartz tube 8 cm in diameter and 45 cm in height. The top of the quartz tube was fitted with a monel cap which was sealed to the quartz tube with a Viton® O-ring. The quartz tube was seated in a carbon-element resistance furnace with the top ~17 cm of the tube extending out of the furnace. The quartz tube was sealed to the furnace case with an external Viton® O-ring to allow evacuation of the heating-element chamber. The furnace housing was water cooled as was the monel cap on the quartz tube.

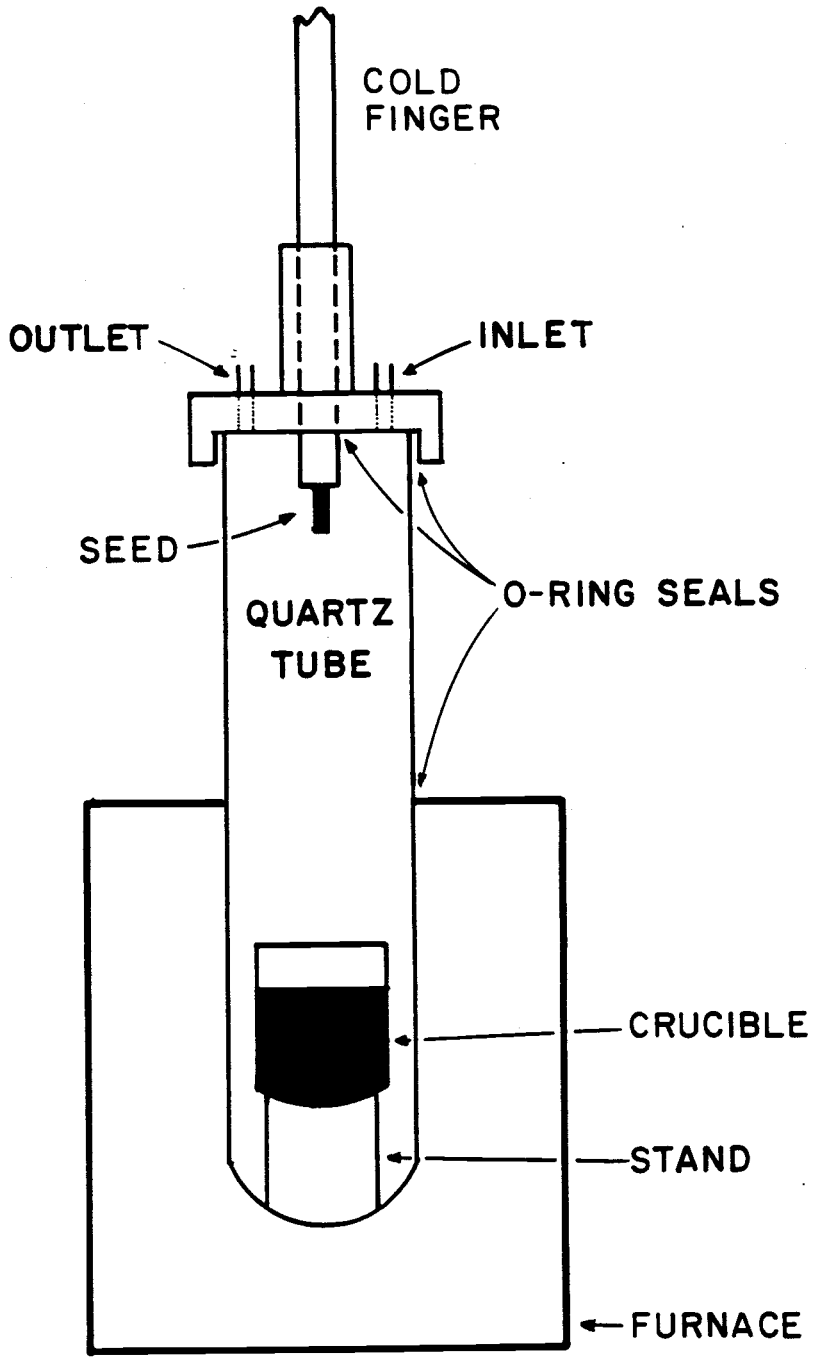

Figure 2.1 Crystal growth apparatus.

A water-cooled cold finger passed through the cap on the quartz tube. A Kal-Rez® O-ring which was lubricated with Krytox® fluorinated grease allowed rotation and vertical motion of the cold finger. The rotation and vertical motion was controlled with two d. c. motor controllers. The cold finger was fabricated of nickel and plated with rhodium. A seed crystal was attached to the cold finger with a rhodium-plated screw.

The rhodium-plated monel cap on the quartz tube was fitted with two ports. One port was connected via polyethylene tubing to a Pyrex® manifold with greaseless valves through which various gasses could be added to the growth chamber. The other port was connected to a second manifold through which the growth chamber could be evacuated. This arrangement allowed the treatment of the KBr with reactive gasses and the evacuation of any volatile contaminants without contamination of the gas-adding manifold.

The crystal growth procedure was similar for all crystals used in the present investigation. The growth tube was loaded with the KBr and assembled to the furnace. Any dopants were mixed with the KBr at this time. The growth tube was evacuated and heated at ~150°C for ~12 hours to remove any adsorbed water from the KBr. The temperature was then slowly increased, and the growth tube was flushed with argon. When the temperature

reached ~250°C, electronic-grade HBr was introduced to the growth tube. As the temperature was increased to the melting point of the KBr (734°C), the HBr was removed and replaced with fresh HBr a minimum of nine times. After the KBr had melted, at least three additional HBr exchanges were performed. The HBr treatments remove hydroxide ion impurities from the KBr by forming H_2O and Br^-.

The HBr treatment sequence was interrupted at various times to add Cl_2 or O_2 to the growth tube. The Cl_2 and O_2 treatment sequences varied for each set of crystals and is given explicitly in Table 2.1. In general, the use of an oxidizing gas removes organic impurities from the KBr.

After the three final HBr exchanges were made on the molten salt, the melt was placed under vacuum for ~45 min at ~30°C above the melting point to remove any dissolved HBr. Then ~$\frac{3}{4}$ atm of argon was introduced to the growth tube.

The crystal was seeded by lowering the seed into the KBr while the cold finger rotated at ~6 RPM. When the seed had partially melted, pulling was begun. The pull rate was maintained at ~1 cm/hour for the duration of the growth period. The furnace temperature was lowered to increase the diameter of the crystal to ~3 cm, and minor temperature adjustments were made

Table 2.1 Crystal Growth Parameters.

I.D. Number	Dopant	Conc. in Melt(mppm)	Reactive Gas Treatment	Cooling Time(hrs)	Comments
408	Pure	----	284-9HBr-M-3HBr-Ar	0.5	
413	Pure	----	342-7HBr-M-5HBr-Ar	0.5	
451	Pure	----	342-9HBr-M-3HBr-Ar	0.5	Frozen in melt
751	Pure	----	266-9HBr-M-$2Cl_2$-3HBr-Ar	1	Frozen in melt
834	Pure	----	275-9HBr-M-$2Cl_2$-3HBr-Ar	1	
841	Pure	----	290-9HBr-M-$2Cl_2$-3HBr-Ar	23	
232-79	*	*	275-$2O_2$-6HBr-$2O_2$-$2Cl_2$-M-4HBr-$2Cl_2$-3HBr-Ar	1.5	Reseeded once
235-79	*	*	212-6HBr-$3O_2$-$4Cl_2$-4HBr-M-3HBr-Ar	12	Frozen in melt
224-80	Pure	----	253-3HBr-$3O_2$-8HBr-M-3HBr-Ar	1	
34-82	Ca^{++}	1934	257-9HBr-$3Cl_2$-M-3HBr-Ar	18	
37-82	Ca^{++}	893	257-8HBr-$4Cl_2$-M-4HBr-Ar	7.5	
316-81	Cd^{++}	316	235-8HBr-$3Cl_2$-M-Cl_2-3HBr-Ar	18.5	
342-81	Cd^{++}	1065	264-7HBr-$4Cl_2$-M-Cl_2-4HBr-Ar	19	Poorly seeded
365-81	Cd^{++}	342	264-6HBr-$4Cl_2$-3HBr-M-3HBr-Ar	19	
116-82	Cd^{++}	1034	254-8HBr-$3Cl_2$-M-4HBr-Ar	19	
123-82	Cd^{++}	1604	260-8HBr-$3Cl_2$-M-4HBr-Ar	20	
247-80	Pb^{++}	20	235-4HBr-$4Cl_2$-5HBr-M-4HBr-Ar	14.5	
281-80	Pb^{++}	106	238-3HBr-$3Cl_2$-7HBr-M-3HBr-Ar	17	
291-80	Pb^{++}	7.6	242-4HBr-$3Cl_2$-8HBr-M-3HBr-Ar	9	
304-80	Pb^{++}	200	256-4HBr-$4Cl_2$-5HBr-M-4HBr-Ar	17	
228-81	Pb^{++}	5230	252-4HBr-$3Cl_2$-6HBr-M-2HBr-Ar	17	
127-82	Pb^{++}	2711	256-8HBr-$3Cl_2$-M-5HBr-Ar	17	

* Fe^{2+} was added to the melt in these crystals, but a flame atomic absorption analysis of the crystals yielded no detectable level of iron. The detection limit of the analysis places an upper limit of 0.7 mppm on the iron concentration.

throughout the growth process to maintain this diameter. Typical crystals were from 6 — 9 cm in height, requiring ~4 — 7 hours of growth time.

To halt crystal growth, the crystal was manually raised from the melt and the furnace temperature was lowered to room temperature. The rate of the temperature reduction varied and is given in Table 2.1 for each crystal.

C. Dopant Concentrations

The initial dopant concentration in the melt is given in Table 2.1 for each of the crystals grown in this investigation. This concentration was calculated from the potassium bromide and dopant masses. The dopant concentrations in the crystals were consistently much lower than the calculated melt concentrations, indicating that the solid-liquid distribution coefficient is less than one for Ca^{2+}, Cd^{2+}, and Pb^{2+} in KBr.

When a distribution coefficient, D, is less than one, the dopant concentration will increase in the crystal as it grows. The concentration of dopant in the crystal is given by

$$C_c(X) = DC_m(X) \quad , \tag{2.1}$$

where $C_c(X)$ is the concentration of dopant in the crystal at a position X cm from the top, and $C_m(X)$ is the

concentration of dopant in the melt after X cm of crystal has grown. If D is much less than one, then $C_m(X)$ is given by

$$C_m(X) = C_m(0) \left[\frac{M_m(0)}{M_m(0) - M_c(X)} \right] , \qquad (2.2)$$

where $M_m(0)$ is the mass of the melt when X is zero, and $M_c(X)$ is the mass of the crystal after X cm of crystal has grown. If the cross-sectional area of the crystal, A, is nearly constant, then $M_c(X) = A\rho X$, where ρ is the density of the crystal. Thus, from equation (2.2), equation (2.1) may be rewritten as

$$\frac{C_m(0)}{C_c(X)} = \frac{1}{D} - \frac{A\rho X}{DM_m(0)} . \qquad (2.3)$$

Dopant concentration profiles are shown in Figures 2.2 through 2.4 for calcium, cadmium, and lead doped crystals. The numerical data are listed in Appendix I. Lead and cadmium concentrations were determined by atomic absorption on a Perkin Elmer model 403 spectrophotometer with a 4-inch air-acetylene burner. The calcium concentrations were determined by atomic emission using the same instrument.

The analysis was performed by comparison of ~10% KBr sample solutions with two sets of reference

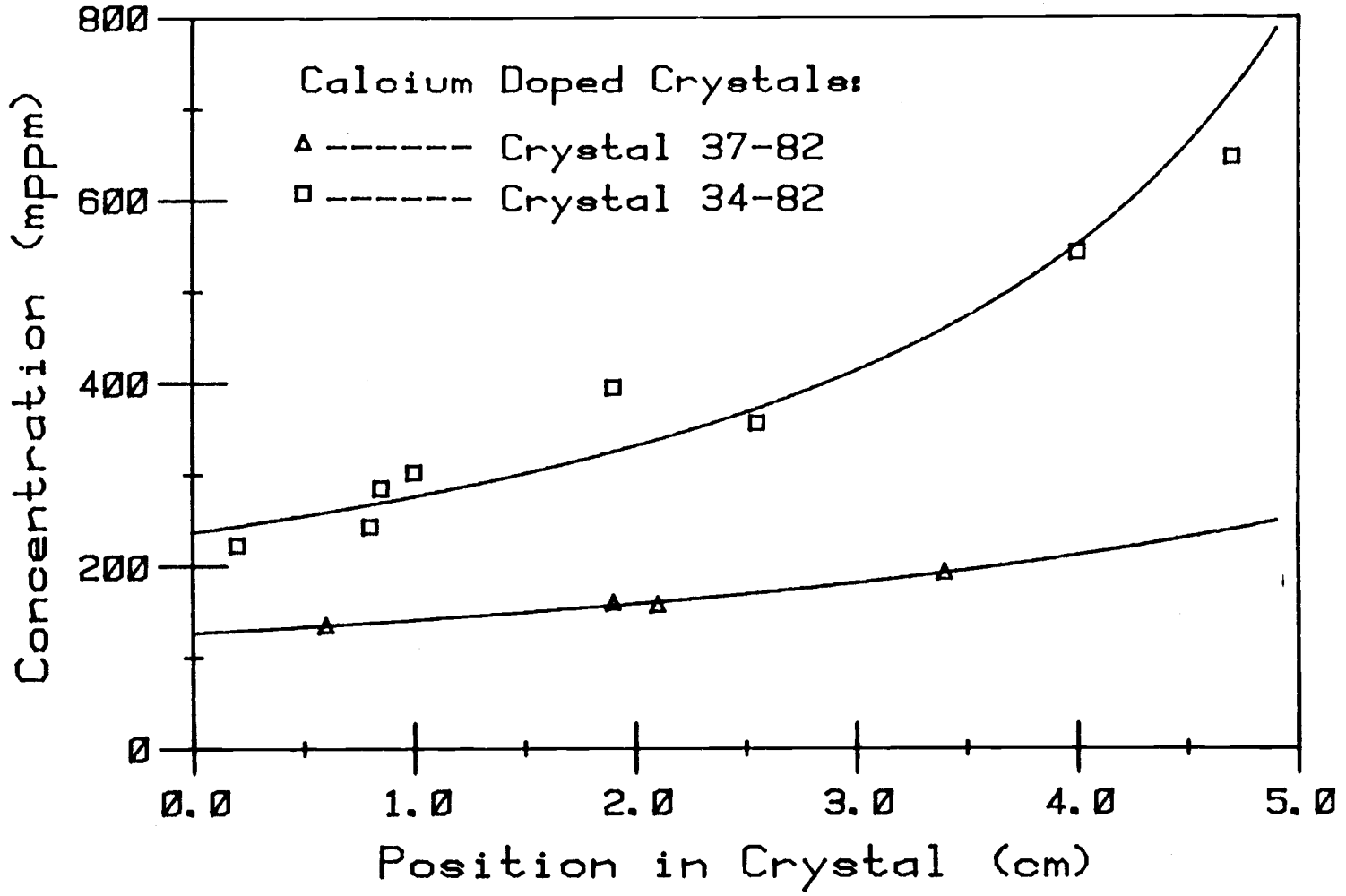

Figure 2.2 Calcium concentration as a function of distance from top of crystal.

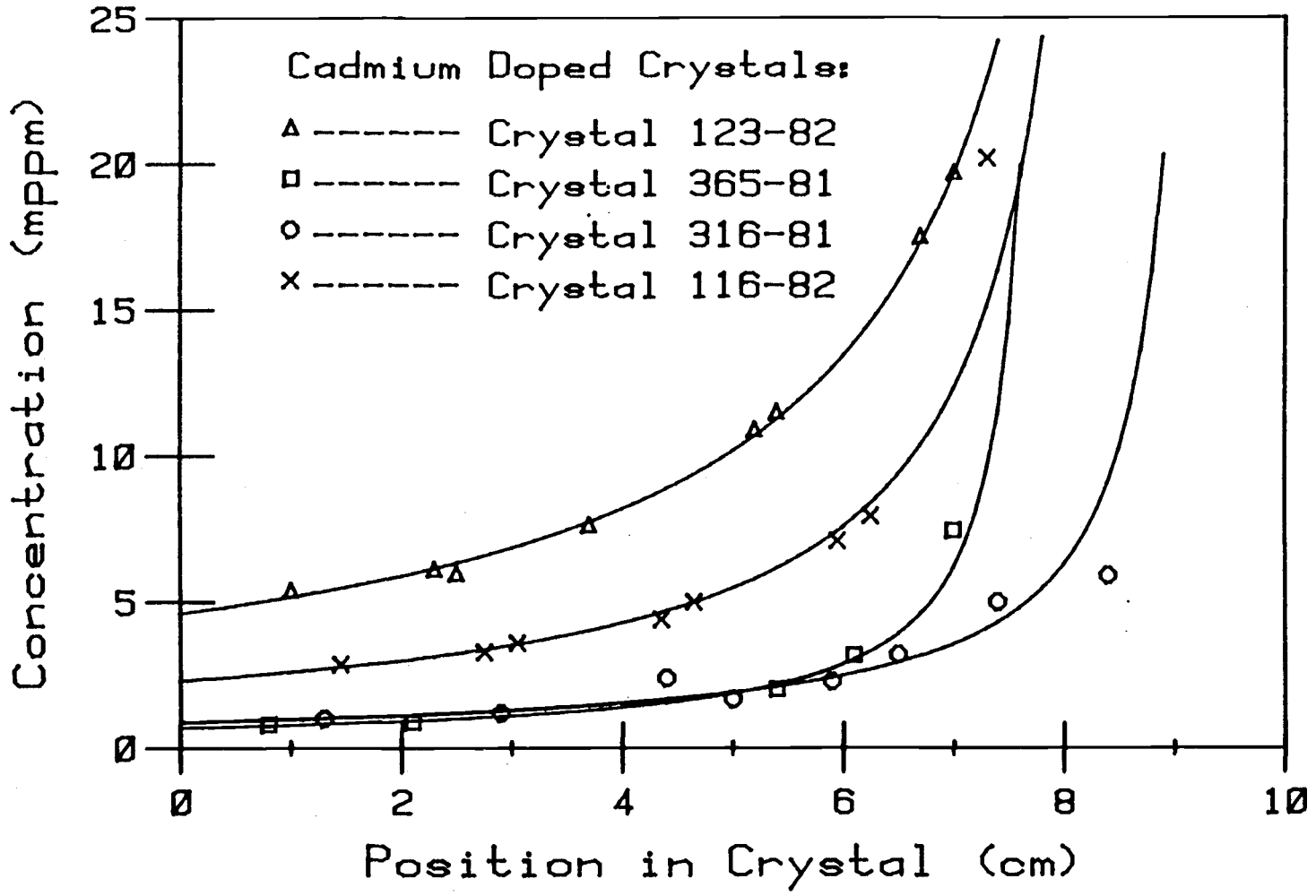

Figure 2.3 Cadmium concentration as a function of distance from top of crystal.

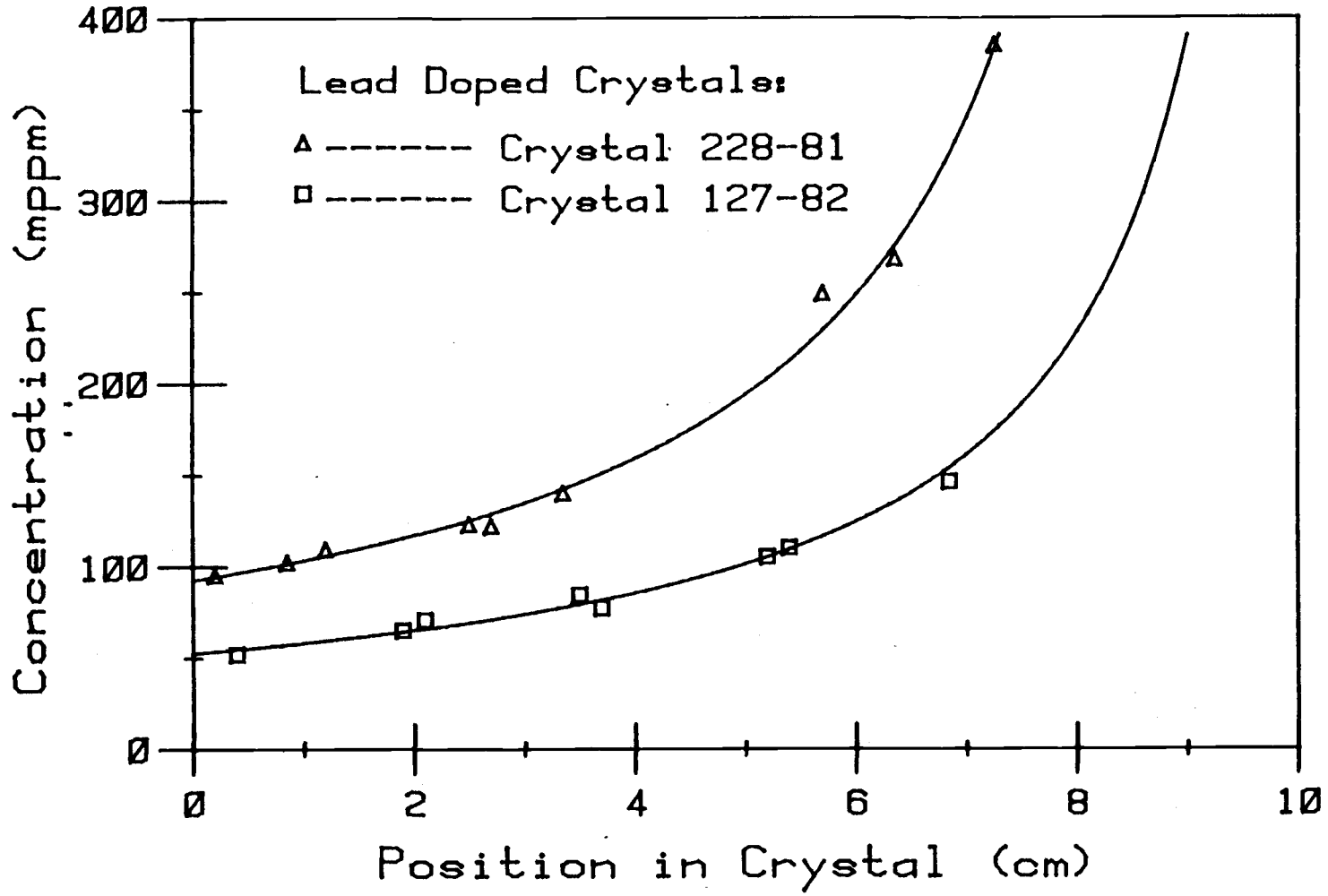

Figure 2.4 Lead concentration as a function of distance from top of crystal.

standards prepared with KBr from the pure crystals. The two sets of reference standards were prepared with KBr concentrations of ~11% and ~6%. By interpolation between the analyte concentrations determined from these two sets of standards, an accurate analyte concentration could be determined in the sample solutions.

It is very important in this type of analysis that the reference solution used to prepare the standards be free of any analyte species. For the lead analysis, the absence of a characteristic ultraviolet absorption band in the crystalline KBr ensured a lead concentration well below the detection limit of atomic absorption. For the calcium analysis, the absence of a calcium emission line from the pure reference solutions ensured a negligible calcium concentration. At the wavelength of the cadmium absorption line the background absorption from KBr is negligible. Thus, the absence of cadmium absorption in the pure reference solution could be determined directly.

The data in Figures 2.2 through 2.4 have been fit to equation 2.3 using a least-squares procedure. From these plots, using values for $C_m(0)$ from Table 2.1, the distribution coefficients may be calculated. These are listed in Table 2.2.

Distribution coefficients determined in this manner are only approximate. While heating the KBr, sublimation and evaporation occur. Unless the KBr and dopant

Table 2.2 Approximate Distribution Coefficients.

Calcium in KBr		Cadmium in KBr		Lead in KBr	
Xtal I.D.	D	Xtal I.D.	D	Xtal I.D.	D
37-82	> 0.14	123-82	> .0029	228-81	> .0177
34-82	> 0.12	365-81	> .0020	127-82	> .0193
		316-81	> .0028		
		116-82	> .0022		
Average	> 0.13	Average	> .0025	Average	> .0185

sublime and evaporate congruently, $C_m(0)$ will be altered. $CdBr_2$ and $PbBr_2$ melt at 567°C and 373°C, respectively (Handbook of Chemistry and Physics, 1976). Thus $C_m(0)$ will be lower than calculated prior to heating, and the distribution coefficients in Table 2.2 for Pb^{2+} and Cd^{2+} are, consequently, minimum values. The melting point of $CaBr_2$ is 740°C (Handbook of Chemistry and Physics, 1976), which is nearly the same as the KBr melting point.

D. Sample Preparation

The crystals were cleaved into approximately one-centimeter cubes for study. Dopant concentrations in the samples were determined as described in part C of this chapter. With the aid of the position versus dopant-concentration plots, concentration gradients in the samples were also determined.

To determine the effect of thermal history on the optical properties of the doped samples, they were given various thermal treatments. The samples were placed in quartz tubes which were evacuated and filled with $\sim\frac{1}{3}$ atm of dry argon. The tubes were then sealed and placed into a furnace for treatment.

A set of quenched samples and a set of annealed samples were prepared from the calcium and cadmium doped crystals. In the quenching process, the samples were heated to ~550°C for ~1 hour. The sample tubes were

then quickly removed from the furnace and immediately placed into an ice-water bath. They became cool to the touch within ~15 seconds. In the annealing process, the samples were also heated to ~550°C, but the temperature was then slowly lowered to room temperature. A time versus temperature plot for these annealed samples is shown in Figure 2.5.

The lead doped samples were also either quenched or annealed. However, three sets of quenched samples were prepared: one set quenched from ~550°C, one set quenched from ~350°C, and one set quenched from ~200°C. The set of annealed lead doped samples was prepared similarly to the calcium and cadmium doped annealed samples, but the annealing time was somewhat longer. A time versus temperature plot for the lead doped annealing process is also shown in Figure 2.5.

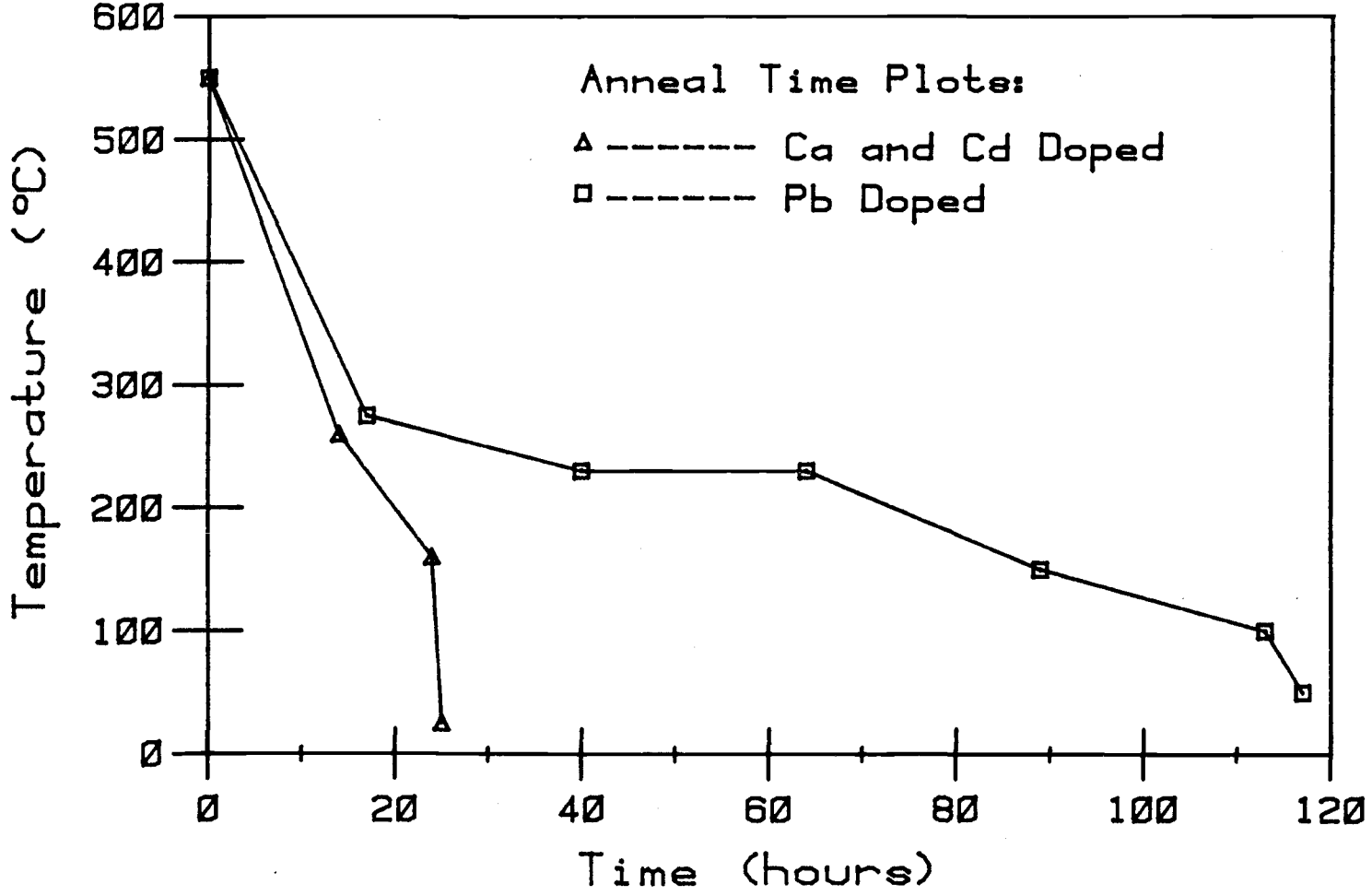

Figure 2.5 Annealing time-temperature profiles.

III. LIGHT SCATTERING THEORY

A. Mandel'shtam-Brillouin-Gross Scattering

Many investigators during the early part of the twentieth century contributed to the development of our present understanding of light scattering, and the reader is referred to a historical review by Young (1982). The elementary theory is briefly outlined here.

In a perfect, pure cyrstal, light is elastically scattered by dielectric inhomogeneities produced by thermally induced entropy fluctuations. The scattering of light by this process is termed Gross scattering (Gross, 1930).[1] Light is inelastically scattered by thermally induced phonon oscillations.

There are 3S normal mode dispersion curves for an ionic crystal, where S is the number of atoms per unit cell (S = 2 for KBr). These dispersion curves can, in principle, be obtained from harmonic solutions to the equations of motion for the atoms in the crystal. The branches (modes) of the dispersion curves for which the

[1] In the previous literature, Gross scattering has often been termed Rayleigh scattering. Here the term Rayleigh scattering will be reserved for scattering from small particles. This follows the terminology proposed by A. T. Young (1982).

angular frequency, ω, remains finite while the wave vector, $\vec{q}$, goes to zero are considered the optical phonon branches. These oscillations correspond to the atoms within a unit cell moving in opposite directions to one another and are responsible for Raman scattering in a crystal (observed by C. V. Raman in 1928). There are 3(S - 1) of these branches. In the three remaining branches, ω goes to zero as $\vec{q}$ goes to zero. These are the acoustic phonon branches responsible for MB scattering. In the acoustic branches, the atoms within a unit cell move in unison and are equivalent to macroscopic sound waves. The dispersion relation for acoustic phonons depends on both the magnitude and direction of $\vec{q}$ (as does the sound velocity).

The interaction of light with acoustic phonons must necessarily involve only phonons with $\vec{q}$ of comparable magnitude to the wave vector of the incident photon, $\vec{k}$. The resulting scattered wave, $\vec{E}_s(\vec{r},t)$, is given by (Cummins, 1969)

$$\vec{E}_s(\vec{r},t) \propto \exp(i(\vec{k}_s \cdot \vec{r} - (\omega_o \pm \omega_q)t)) \int_V \exp(i(\vec{k}_o \pm \vec{q} - \vec{k}_s) \cdot \vec{r}')dV' \quad , \qquad (3.1)$$

where $\vec{E}_s$ is the electric field vector of the scattered wave, $\vec{r}$ is the position vector to the point of observation, V is the scattering volume, t is time, and the

subscripts o, s, and q designate the incident photon, the scattered photon, and the scattering phonon, respectively. This photon-phonon interaction expression thus imposes the requirements that

$$\vec{k}_s = \vec{k}_o \pm \vec{q} \tag{3.2}$$

and

$$\omega_s = \omega_o \pm \omega_q \quad . \tag{3.3}$$

Since phonon frequencies are much smaller than light frequencies, ω_q must be much smaller than ω_o. Thus the magnitude of $\vec{k}_s$ must be equal to the magnitude of $\vec{k}_o$, and $\vec{q}$ is then completely determined by the scattering geometry:

$$|q| = 2n|k_o|\sin(\theta/2) \quad . \tag{3.4}$$

Here θ is the angle between $\vec{k}_o$ and $\vec{k}_s$, and n is the index of refraction of the medium. The direction of $\vec{q}$ is along the bisector of θ. For acoustic modes of a crystal, ω_q and $\vec{q}$ are related by

$$v = \frac{\omega_q}{|\vec{q}|} \quad , \tag{3.5}$$

where v is the speed of sound in the direction of $\vec{q}$ (i.e., the slope of the dispersion curve at $\vec{q}$). Combining equations (3.3), (3.4), and (3.5) yields

$$\omega_s - \omega_o = \pm 2vn \, |\vec{k}_o| \sin(\theta/2) \quad . \tag{3.6}$$

This relation can also be derived by considering that the light is scattered from a moving wave train of phonons. The scattered light is then doppler-shifted as given by equation (3.6).

The sound velocity in a crystal, and hence the MB frequency shift, can be related to the elastic tensor of the crystal by plane-wave solutions to the equations of motion for atom displacements within the crystal. The components of the elastic tensor are the proportionality constants between the strain and stress tensors of a crystal. In a one-dimensional crystal, this would simply be the Hooke's law force-constant between the atoms. In a three-dimensional crystal, the strain and stress are described by second-rank tensors. Therefore, the elastic tensor is of fourth rank, with elements C_{iklm}. The equations of motion are of the form

$$\rho \ddot{u}_i = C_{iklm} \frac{\partial^2 u_m}{\partial r_k \partial r_l} \quad . \tag{3.7}$$

Here ρ is the density of the crystal, u_i is the atom displacement in the i^{th} direction ($i = 1, 2, 3$), and r_k and r_l are components of the position vector $\vec{r}$. In this notation, the Einstein summation convention is

implied (Nye, p. 7, 1957), and the double dots refer to the second time derivative. As discussed above, the equations of motion will depend on the direction of $\vec{q}$, and so they must be solved for the particular direction of $\vec{q}$ which will be observed experimentally.

Since the stress and strain tensors of a crystal are symmetric, the 81-element elastic tensor only contains 36 distinct elements. These are generally given as the components of a sixth-order square matrix. For KBr, which is a cubic crystal, the 36 elements are reduced to 12 non-zero components, of which only three are distinct (Nye, 1957, p. 120). These are

$$C_{11} = C_{22} = C_{33} \tag{3.8}$$

$$C_{12} = C_{21} = C_{13} = C_{31} = C_{23} = C_{32} \tag{3.9}$$

$$C_{44} = C_{55} = C_{66} \quad . \tag{3.10}$$

In the experimental scattering geometry of this investigation, θ is 90°, $\vec{k}_o$ propagates along [1,0,0] with [0,0,1] polarization, and $\vec{k}_s$ propagates along [0,1,0] (no analyzer). For this scattering geometry, $\vec{q}$ will be along [1,1,0], and the solutions to the equations of motion are (Cummins and Schoen, 1972)

$$\rho v^2 = \frac{C_{11} + C_{12} + 2C_{44}}{2} \qquad \vec{u} = (1,1,0)/\sqrt{2} \tag{3.11}$$

$$\rho v^2 = \frac{C_{11} - C_{12}}{2} \qquad \vec{u} = (1,-1,0)/\sqrt{2} \quad (3.12)$$

$$\rho v^2 = C_{44} \qquad \vec{u} = (0,0,1) \quad . \quad (3.13)$$

An incident photon is optically coupled to thermal phonons by the elasto-optic effect. The thermal phonons induce a strain which generates a proportional change in the reciprocal dielectric tensor. The proportionality constants form the elasto-optic tensor. The amplitude of the phonon oscillations (i.e., the magnitude of the strain) will depend on the temperature of the material. From these considerations, the scattering coefficient for MB scattering, R_{MB}, is given by (Cummins and Schoen, 1972)

$$R_{MB} = \frac{kT\omega_s^4}{32\pi^2 c^4 \rho v^2} [e_s \cdot M \cdot e_0]^2 \quad . \quad (3.14)$$

Here k is Boltzmann's constant, T is the temperature, c is the velocity of light, e_s and e_0 are unit vectors along the polarization directions of the scattered and incident photons, and M is a matrix which will be discussed below. The scattering coefficient relates the incident and scattered light intensities by

$$I_s = R_{MB} \frac{VI_0}{r^2} \quad , \quad (3.15)$$

where V is the scattering volume, r is the distance to the point of observation, and I_0 and I_s are the incident and scattered light intensities, respectively. A scattering coefficient is thus a measure of the efficiency of scattering independent of the experimental arrangement. The matrix, M, in equation (3.16) is unique for each phonon mode. It is derived by considering the tensorial relations between stress and the reciprocal dielectric constant (see Cummins and Schoen, 1972, for a detailed description of this process).

For the experimental scattering geometry given above, the matrix elements in equation (3.14) are (Cummins and Schoen, 1972)

$$[e_s \cdot M_L \cdot e_0]^2 = \varepsilon^4 P_{12}^2 \qquad \vec{u} = (1,1,0)/\sqrt{2} \qquad (3.16)$$

$$[e_s \cdot M_{T_1} \cdot e_s]^2 = 0 \qquad \vec{u} = (1,-1,0)/\sqrt{2} \qquad (3.17)$$

$$[e_s \cdot M_{T_2} \cdot e_0]^2 = \frac{\varepsilon^4 P_{44}^2}{2} \qquad \vec{u} = (0,0,1) \quad . \qquad (3.18)$$

Here ε is the dielectric constant, and the P_{ij}'s are elements of the elasto-optic tensor (these elements are commonly called Pockel's constants). L designates the longitudinal mode matrix, and T_1 and T_2 designate the transverse modes.

The elastically scattered peak (Gross peak) in the MBG spectrum arises from thermal entropy fluctuations. For non-viscous liquids, the intensity of these non-propagating fluctuations can be related to the intensity of phonon oscillations by the simple relation (Fabelinski, 1968)

$$\frac{R_G}{2R_{MB}} = \frac{9\alpha_\ell^2 T}{\rho C_p \beta_s} = \eta_{LP} \quad . \tag{3.19}$$

Here R_G is the scattering coefficient for the Gross scattering, R_{MB} is the scattering coefficient for the MB scattering (one peak of the doublet), C_p is the constant pressure heat capacity, β_s is the adiabatic compressibility, α_ℓ is the linear thermal expansion coefficient, and η_{LP} is the Landau-Placzek ratio (Landau and Placzek, 1934). The adiabatic compressibility is a function of the sound velocity: $\beta_s = 1/\rho v^2$ (Fabelinski, 1968). In the present investigation, ρv^2 is given by equation (3.11) (the transverse velocity contributes negligibly to η_{LP}). Equation (3.19) thus becomes

$$\eta_{LP} = (C_{11} + C_{12} + 2C_{44}) \frac{9\alpha_\ell^2 T}{2\rho C_p} \quad . \tag{3.20}$$

For solids, the thermodynamic arguments used to arrive at equation (3.20) must be modified. In

particular, Fabelinski (1956) pointed out that the direct dependence of the dielectric constant on temperature had been ignored. Also, the large shear stresses possible in solids enable the direct coupling of light to entropy fluctuations. Wehner and Klein (1972) have included these effects in a microscopic theory of fluctuations in phonon occupation numbers. They arrive at the result

$$\eta'_{LP} = \eta_{LP}(1 - r)^2 \quad , \tag{3.21}$$

where r is given by

$$r = \frac{C_{11}}{C_{11} + 2C_{12}} \left[\frac{(\frac{\partial \varepsilon}{\partial T})_p}{\alpha_\ell \varepsilon^2 P_{12}} + \frac{P_{11}}{P_{12}} + 2 \right] . \tag{3.22}$$

The constants in equations (3.20) and (3.22) are only mildly dependent on impurity concentration. Thus it should be possible to obtain η'_{LP} for a perfect pure crystal from measurements performed on only moderately pure materials. Values of the constants in equations (3.20) and (3.22) are listed in Table 3.1 for KBr. Many of the values for these constants differ between investigators. Fredericks et al. (1984) have calculated η'_{LP} for various combinations of the disparate values, yielding

Table 3.1 Various Material Constants of KBr.

Quantity	Value	Reference
α_ℓ	38.4×10^{-6} K^{-1}	Landolt-Bornstein (1973)
n	1.572	A.I.P. Handbook (1963)
$\{\frac{\partial E}{\partial T}\}_p$	-12.2×10^{-5} K^{-1}	Havinga and Bosman (1965)
$\{\frac{\partial E}{\partial T}\}_p$	-12.8×10^{-5} K^{-1}	A.I.P. Handbook (1963)
ρ	2.753 $g\text{-}cm^{-3}$	Landolt-Bornstein (1969)
C_p	0.4398J-g^{-1}-K^{-1}	Janaf Therm. Tables (1971)

C_{11}(GP)	C_{12}(GP)	C_{44}(GP)	Reference
34.6	5.61	5.15	Landolt-Bornstein (1966)
34.5	5.5	5.10	Landolt-Bornstein (1979)
35.1	6.1	5.1	Braul and Plint (1981)
33.7	6.1	5.1	Matsura and Miyazawa (1973)

P_{11}	P_{12}	P_{44}	Reference
0.198	0.154	-0.023	Landolt-Bornstein (1966)
0.212	0.165	-0.022	Landolt-Bornstein (1979)
0.220	0.171	-0.019	Braul and Plint (1981)

$$0.056 < \eta'_{LP} < 0.11 \quad . \tag{3.23}$$

B. Particle Scattering

When impurities and defects are present, the elastically scattered light will be increased but the MB scattering will remain nearly constant (Fredericks, et al., 1984). The experimental scattering ratio, η_T, will then be

$$\eta_T = \frac{R_G + R_E}{2R_{MB}} \quad , \tag{3.24}$$

where R_E is the scattering coefficient for impurity and defect scattering. The difference between η_T and η_{LP} will thus give a measure of the purity and perfection of the crystal. The measurement of η_T also provides a convenient means of measuring the scattering coefficient of the elastically scattered light; the MB peaks provide an internal standard for the measurement.

Scattering from an impurity is caused by an inhomogeneity in the dielectric constant at the site of the impurity due to the difference in polarizability of the impurity relative to the host. The theoretical description of scattering from small particles was originally given by Rayleigh (1871). The degree of "smallness" required for the Rayleigh theory to be valid is approximately $a < .05\lambda$ (Pangonis et al., 1960), where a is the

radius of the scatterer and λ is the wavelength of the light. For spherical scatterers, the scattering coefficient for 90° scattering is

$$R_R = \frac{16N\pi^4\alpha^6}{\lambda^4}\left[\frac{n^2 - 1}{n^2 + 2}\right]^2 , \qquad (3.25)$$

where N is the number of particles per unit volume. This expression is for light polarized perpendicular to the scattering plane, and the scattered light will also be perpendicularly polarized. No light of parallel polarization is scattered by small spheres. Equation (3.25) can be expressed in terms of the polarizability of the particle, α, as

$$R_R = \frac{16N\pi^4\alpha^2}{\lambda^4} . \qquad (3.26)$$

For nonspherical particles, α is no longer isotropic. When the particle is a spheroid, α may be characterized by a polarizability along the singular axis, α', and a polarizability along the two equal axes, α''. The Rayleigh ratios for random orientation of the particles and 90° scattering are

$$R_{VV} = \frac{16N\pi^4}{15\lambda^4}\left(3(\alpha')^2 + 4\alpha'\alpha'' + 8(\alpha'')^2\right) , \qquad (3.27)$$

$$R_{VH} = R_{HH} = R_{HV} =$$

$$\frac{16N\pi^4}{15\lambda^4}\left((\alpha')^2 - 2\alpha'\alpha'' + (\alpha'')^2\right) \quad , \qquad (3.28)$$

where the first subscript on R indicates the polarization of the incident light (vertical or horizontal relative to the scattering plane), and the second subscript indicates the polarization of the scattered light. For the limiting cases of rods and discs, the polarizabilities are given by

$$\text{(rods)} \quad \alpha' = \frac{V(n^2 - 1)}{4\pi} \quad ; \quad \alpha'' = \frac{V(n^2 - 1)}{2\pi(n^2 + 1)} \qquad (3.29)$$

$$\text{(discs)} \quad \alpha' = \frac{V(n^2 - 1)}{4\pi n^2} \quad ; \quad \alpha'' = \frac{V(n^2 - 1)}{4\pi} \quad , \qquad (3.30)$$

where V is the volume of the particle.

The theoretical description of scattering from large particles was developed by Mie (1908). For spherical particles, the scattering coefficients are given by

$$R_{VV} = \frac{\lambda^2}{4\pi^2}\,|S_1|^2 \qquad (3.31)$$

$$R_{HH} = \frac{\lambda^2}{4\pi^2} |S_2|^2 \tag{3.32}$$

$$R_{VH} = R_{HV} = 0 \tag{3.33}$$

where S_1 and S_2 are amplitude functions given by

$$S_1 = \sum_{j=1}^{\infty} \frac{2j+1}{j(j+1)} \left[A_j \Pi_j(\cos\theta) + B_j \tau_j(\cos\theta) \right] \tag{3.34}$$

$$S_2 = \sum_{j=1}^{\infty} \frac{2j+1}{j(j+1)} \left[A_j \tau_j(\cos\theta) + B_j \Pi_j(\cos\theta) \right], \tag{3.35}$$

with $\Pi_j(\cos\theta) = \dfrac{P_j^{(1)}(\cos\theta)}{\sin\theta}$

and $\tau_j(\cos\ ) = \dfrac{dP_j^{(1)}(\cos\theta)}{d\theta}$. (3.36)

Here $P_j^{(1)}$ is the j^{th} associated Legendre polynomial of degree one, and A_j and B_j are functions given by

$$A_j = \frac{\Psi_j(x)\Psi_j'(y) - n\Psi_j(y)\Psi_j'(x)}{\zeta_j(x)\Psi_j'(y) - n\Psi_j(y)\zeta_j'(x)} \tag{3.37}$$

$$B_j = \frac{n\Psi_j(x)\Psi_j'(y) - \Psi_j(y)\Psi_j'(x)}{n\zeta_j(x)\Psi_j'(y) - \Psi_j(y)\zeta_j'(x)} \tag{3.38}$$

with $x = \dfrac{2\pi a}{\lambda}$ and $y = nx$. (3.39)

The functions Ψ_j and ζ_j are given by

$$\Psi_j(x) = \left[\frac{\pi x}{2}\right]^{\frac{1}{2}} J_{j+\frac{1}{2}}(x) \quad ; \quad \Psi_j'(x) = \frac{d\Psi_j(x)}{dx} \qquad (3.40)$$

$$\zeta_j(x) = \Psi_j(x) + i\Phi_j(x) \quad ; \quad \zeta_j'(x) = \frac{d\zeta_j(x)}{dx} \qquad (3.41)$$

$$\text{with } \Phi_j(x) = -\left[\frac{\pi x}{2}\right]^{\frac{1}{2}} N_{j+\frac{1}{2}}(x) \quad , \qquad (3.42)$$

where i is $\sqrt{-1}$, and $J_{j+\frac{1}{2}}$ and $N_{j+\frac{1}{2}}$ are the half integral order Bessel and Neumann functions, respectively.

Thus, through an iterative process on standard mathematical functions (albeit complex), the exact light scattering intensities from a spherical particle can be determined. Unfortunately, the scattering from non-spherical large particles tremendously increases the complexity of the Mie equations. Asano and Sato (1980) have derived exact solutions for spheroids, and have demonstrated the solutions graphically so as to give an idea of the variations relative to spheres.

The general effects of particle size and shape on the polarization properties of scattering can be elucidated by a few simple symmetry laws. It is useful to use a scattering matrix in discussing these laws. The

full scattering matrix consists of a fourth order square matrix which relates the four Stokes parameters of the incident light to the Stokes parameters of the scattered light. Perrin (1942) has shown that for scattering particles which are not birefringent, the matrix elements S_{13}, S_{14}, S_{23}, S_{24}, S_{31}, S_{32}, S_{41}, and S_{42} are zero. Krishnan (1938) has shown that $S_{12} = S_{21}$ and $S_{34} = -S_{43}$. The lower right (2 x 2) portion of the full scattering matrix deals only with the phase relations of the scattering (degree of circular polarization). No circular polarization effects were measured in the present investigation, so these components will not be examined. What is left is a second order square matrix with elements S_{11}, S_{22}, S_{12}, and S_{21} (= S_{12}).

Neglecting phase relations, the Stokes parameters, I and Q, are given by

$$I = I_V + I_H \text{ and } Q = I_V - I_H \tag{3.43}$$

where the subscripts V and H indicate light polarized perpendicular and parallel to the scattering plane. The scattering equation is then

$$\begin{pmatrix} S_{11} & S_{12} \\ S_{12} & S_{22} \end{pmatrix} \begin{pmatrix} I_o \\ Q_o \end{pmatrix} = \begin{pmatrix} I_s \\ Q_s \end{pmatrix} . \tag{3.44}$$

In terms of these matrix elements, the four scattering

coefficients are

$$R_{VV} = S_{12} + S_{22} - 2S_{12} \tag{3.45}$$

$$R_{VH} = S_{11} - S_{22} \tag{3.46}$$

$$R_{HV} = S_{11} - S_{22} \tag{3.47}$$

$$R_{HH} = S_{11} + S_{22} - 2S_{12} \quad . \tag{3.48}$$

When the scattering is from spherical scatterers, $S_{11} = S_{22}$ (equations (3.32) through (3.34)), and

$$R_{VV} = 2(S_{11} - S_{12}) \tag{3.49}$$

$$R_{VH} = R_{HV} = 0 \tag{3.50}$$

$$R_{HH} = 2(S_{11} + S_{12}) \quad . \tag{3.51}$$

When the scattering particles are small (but not necessarily spherical), $S_{22} = -S_{12}$ (equations (3.28) and (3.29)), and

$$R_{VV} = S_{11} + 3S_{22} \tag{3.52}$$

$$R_{VH} = R_{HV} = R_{HH} = S_{11} - S_{22} \quad . \tag{3.53}$$

For pure Rayleigh scattering from spherical particles, $S_{11} = S_{22} = -S_{12}$, and

$$R_{VV} = 4S_{11} \tag{3.54}$$

$$R_{VH} = R_{HV} = R_{HH} = 0 \quad . \tag{3.55}$$

IV. SCATTERING INSTRUMENTATION

A. Mandel'shtam-Brillouin Spectrometer

The apparatus used in these MB scattering measurements was assembled by D. F. Edwards of Los Alamos National Laboratory (LANL). The measurements reported here were made by the author at LANL. A diagram of the apparatus is shown in Figure 4.1 and is described below.

The light source was a Spectra Physics Model 165-8 argon laser. An intracavity etalon in the laser cavity was required to produce a stable single mode line at 488.0 nm, with a line width of about 2×10^{-5} nm and an output power of about 100 mW. A polarization rotator (Spectra Physics Model 310-21) was affixed to the front of the laser. The laser beam was passed through lens L1 to provide a narrow concentrated beam in the scattering sample cell. The scattered light was viewed at 90° through a pinhole into the light-tight box. To eliminate room light, interference filter F passed only the 488 nm light. Lens L2 was focused on the scattering volume (f.l. = 60 cm), and thus a parallel beam entered the Fabry-Perot interferometer.

The interferometer was a Burleigh Instruments triple-pass type (corner mirror reflectors providing the triple-pass operation). The interference cavity

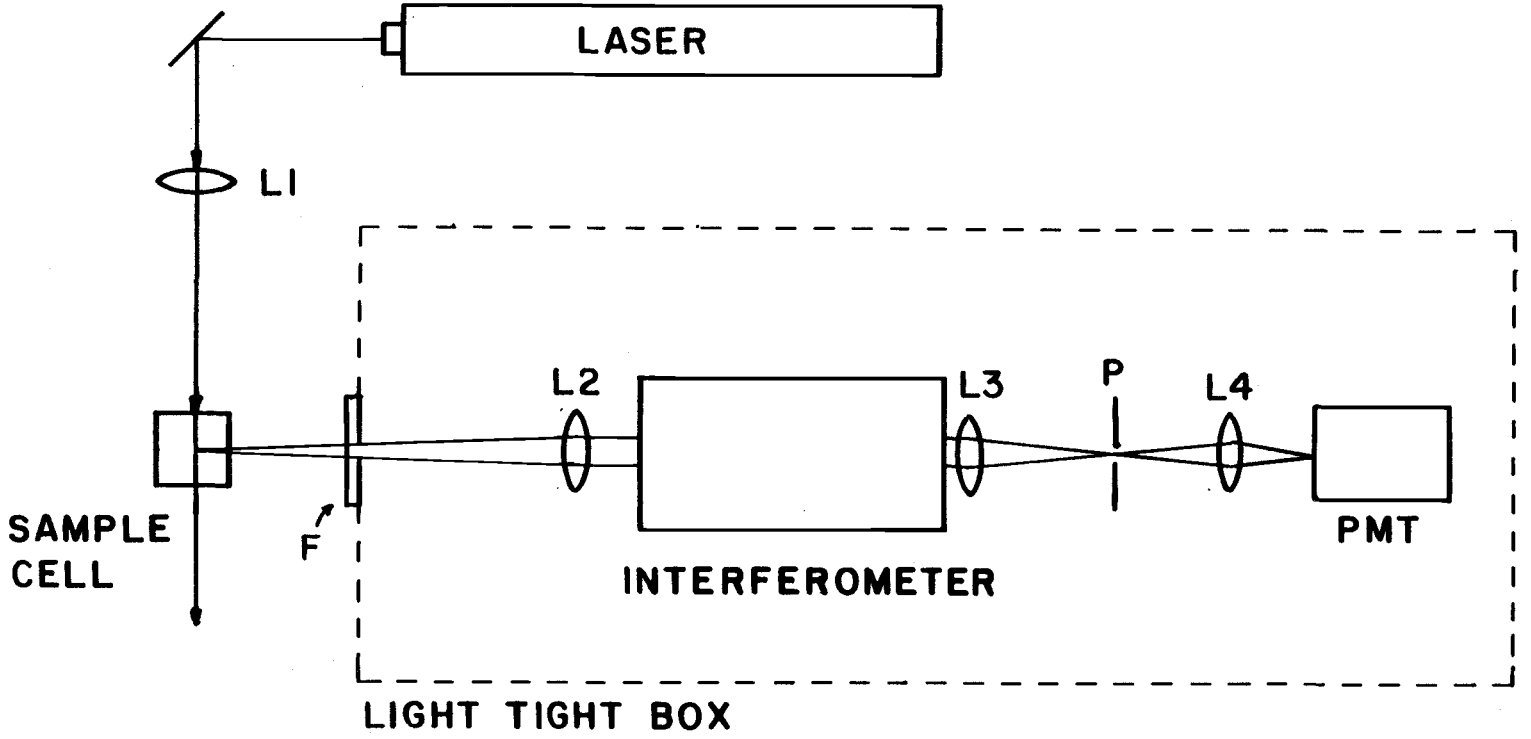

Figure 4.1 Mandel'shtam-Brillouin spectrometer.

consisted of two mirrors with 98.5% reflectance, and a flatness of $\lambda/200$. One mirror was moved relative to the other by the action of three piezoelectric crystals. The piezoelectric scanning action was controlled by a Burleigh Instruments D.A.S. 1 controller which applied a voltage ramp to the piezoelectric elements. In addition, the D.A.S. 1 maintained a high degree of parallelism between the mirrors by varying the bias voltages on the elements in small increments so as to obtain maximum peak intensities.

The light from the interferometer was collected by lens L3 (f.l. = 25 cm) which was focused on pinhole P (diameter = 1.0 mm). Lens L4 (f.l. = 5.5 cm) formed an image of the pinhole on the photomultiplier. The photomultiplier was an I.T.T. Model FW130 which was cooled with a thermo-electric refrigerator to -30°C. The output from the photomultiplier passed through a peak height analyzer and photon counter.

The D.A.S. 1 made repetitive scans of two (sometimes three) spectral orders of the scattered light, and accumulated the photon counts in a 1024 channel multichannel analyzer. The instrumental noise could be reduced to a minimal level by allowing ~30 min of accumulation time per spectrum. For intense scatterers, ~30,000 scans at 0.05 ms/channel were required. For less intense scatterers, the scan rate was slowed to a

minimum of 10 ms/channel. At this rate, ~150 scans were required for a clean spectrum. The accumulation time (~30 min) is the same in these two extreme cases. The MB peaks are of nearly the same intensity in all samples and thus require comparable times for their resolution. The scan rate was varied to accomodate the large differences in the Rayleigh component of the different samples; less intense scatterers required slower scans to facilitate lock-in of the D.A.S. 1 to the scattering peak.

To reduce surface scattering, it was necessary to immerse the sample in an index matching fluid. This required the addition of a new sample cell (Figure 4.2) to the MB Spectrometer. The laser beam entered the cell through a quartz window, passed through the cell, and exited through another quartz window. The scattered light was viewed through a quartz window at 90°, with the fourth window providing a "black" background for the observation. Bromobenzene was employed as the index matching fluid for most spectra (n = 1.56 as compared to n = 1.57 for KBr). In some early measurements, benzene was used (n = 1.50). Both fluids eliminated most of the surface scattering; the switch to bromobenzene was made mainly for health reasons.

In order to accurately measure phonon velocities, it was necessary to calibrate the free spectral range (FSR) of the instrument. The FSR is the wavelength

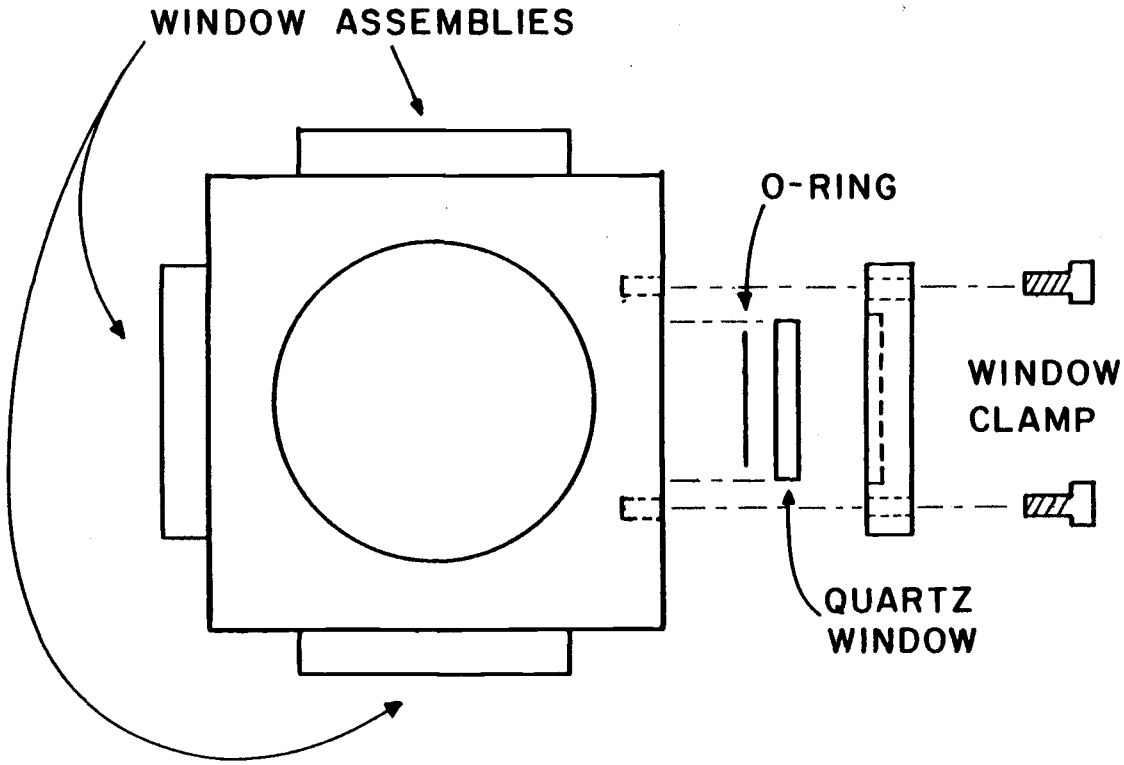

Figure 4.2 Sample cell.

shift between spectral orders of the interferometer. The FSR was determined by using the high-resolution atomic line structure of a mercury lamp. The details of this determination are given in Appendix II; the result is:

$$FSR = 0.0390 \pm 0.0004 \text{ nm} \quad . \tag{4.1}$$

B. Scattering Polarization Spectrometer

The wavelength dependence of the polarization components of the scattered light was measured with the apparatus shown in Figure 4.3. This apparatus was originally constructed for fluorescence measurements by the biophysics group headed by I. Isenberg at Oregon State University (described in detail by Ayres et al. (1973)).

Light from a Cary Instruments Model 450-W xenon lamp, S, passed through two Jarrell-Ash 0.25-m Ebert monochromators in series, M1 and M2. The monochromatic beam passed through a rotatable Glan-Thompson prism polarizer, P1, and was focused onto the sample by lens L1. The scattered light was viewed on both sides of the sample at 90°. Each scattered beam passed through a Glan-Thompson prism analyzer; analyzer A1 transmitted light polarized perpendicular to the scattering plane, and analyzer A2 transmitted light polarized parallel to the scattering plane. These two polarized beams then

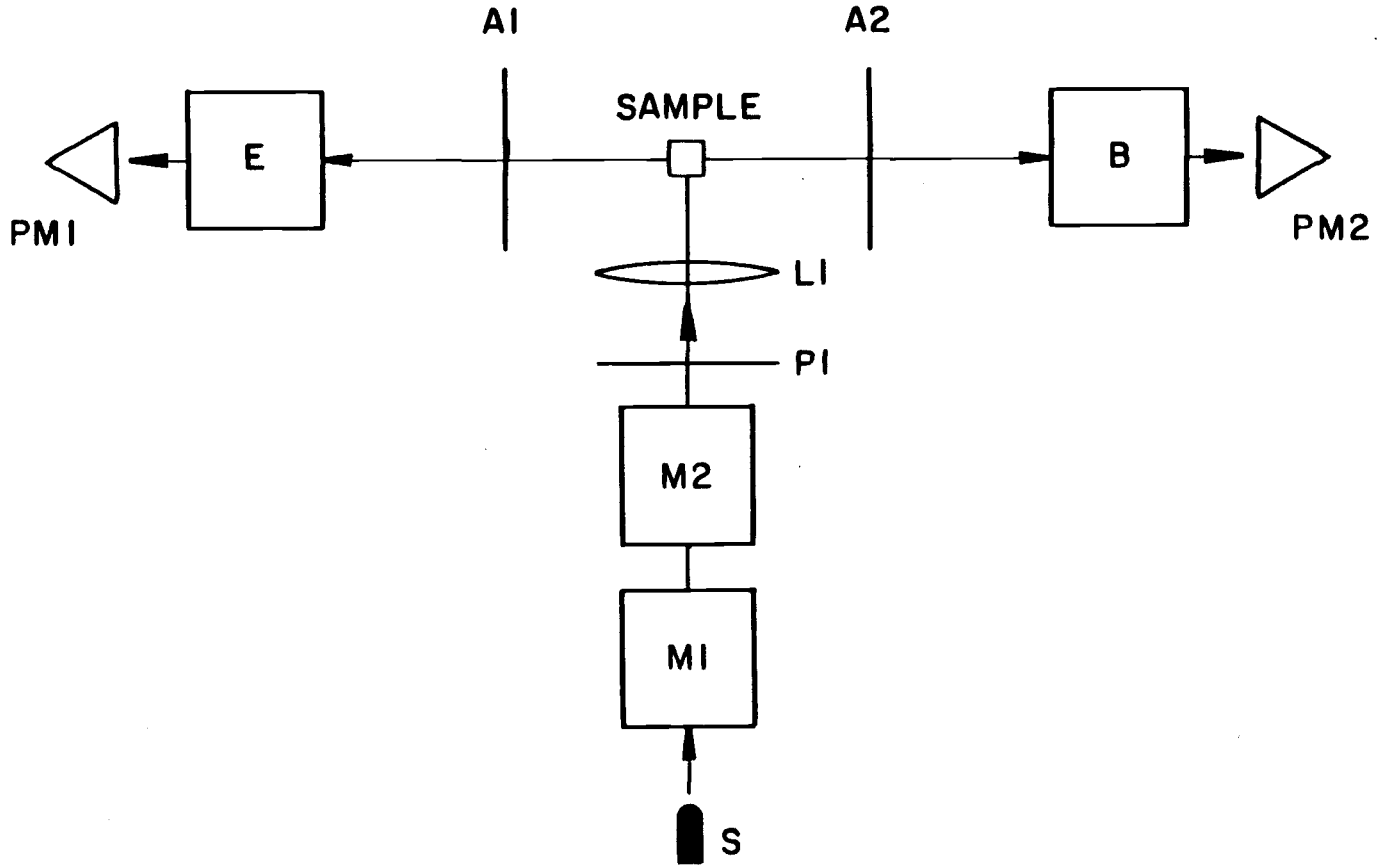

Figure 4.3 Scattering polarization spectrometer.

passed through Jarrell-Ash 0.25-m monochromators, E and B, respectively. The light intensities were detected by EMI 9524B photomultipliers, PM1 and PM2.

Scanning of the monochromators was performed by stepping motors controlled by a Digital Equipment PDP8/E mini-computer. The computer also provided a digital readout of the four intensities I_{VV}, I_{VH}, I_{HV}, and I_{HH}. Since the transmission characteristics of the E and B light paths were slightly different, a method for comparison of the two was necessary. From equations (3.45) through (3.48) it can be seen that, even for non-spherical scatterers, I_{HV} is equal to I_{VH}. Consequently, the ratio of the experimental quantities, $I_{VH}(exp)/I_{HV}(exp)$, yields the ratio of the transmission factors of the two light paths. The experimental values for I_{HH} and I_{HV} were then multiplied by this ratio to yield numbers compatible with the experimental I_{VV} and I_{VH} intensities. Since the difference in transmission characteristics of the two paths included differences in the surface quality of the two faces of the crystal, the ratios were computed individually for each spectrum.

Because of the small size of the sample space in this instrument, the samples could not be immersed in index matching fluids to reduce surface scattering. Careful baffling of the sample area blocked much of the

surface scattering; however, accurate measurements were still limited to the more intense scatterers.

V. SCATTERING MEASUREMENTS ON PURE SAMPLES

A. Results

A trace of a typical pure KBr spectrum is shown in Figure 5.1. The ratio of the FSR to the width of the peaks at half-maximum (FWHM) is about 50. This quantity, called the finesse, gives a measure of the resolution of the instrument; values of 40-60 are typical for apparatus of this type (Fabelinski and Chistyi, 1976). Two spectral orders of the spectrum are shown. The unshifted elastically scattered peaks are at 254 and 762 channels. The large shifted peaks at 117, 388, 632, and 891 channels are attributable to the longitudinal phonon mode given by equation (3.11). The smaller peaks at 192, 313, 704, and 820 channels are from the T_2 transverse mode given by equation (3.13). The T_1 transverse mode given by equation (3.12) is not observed at this scattering geometry. This is predicted by the zero value of the optical coupling matrix element for this mode given in equation (3.17).

The frequency shifts for the undoped samples are listed individually in Appendix III. The average values are

$$\Delta\nu_L = 14.0 \pm 0.2 \text{ GHz} \qquad (5.1)$$

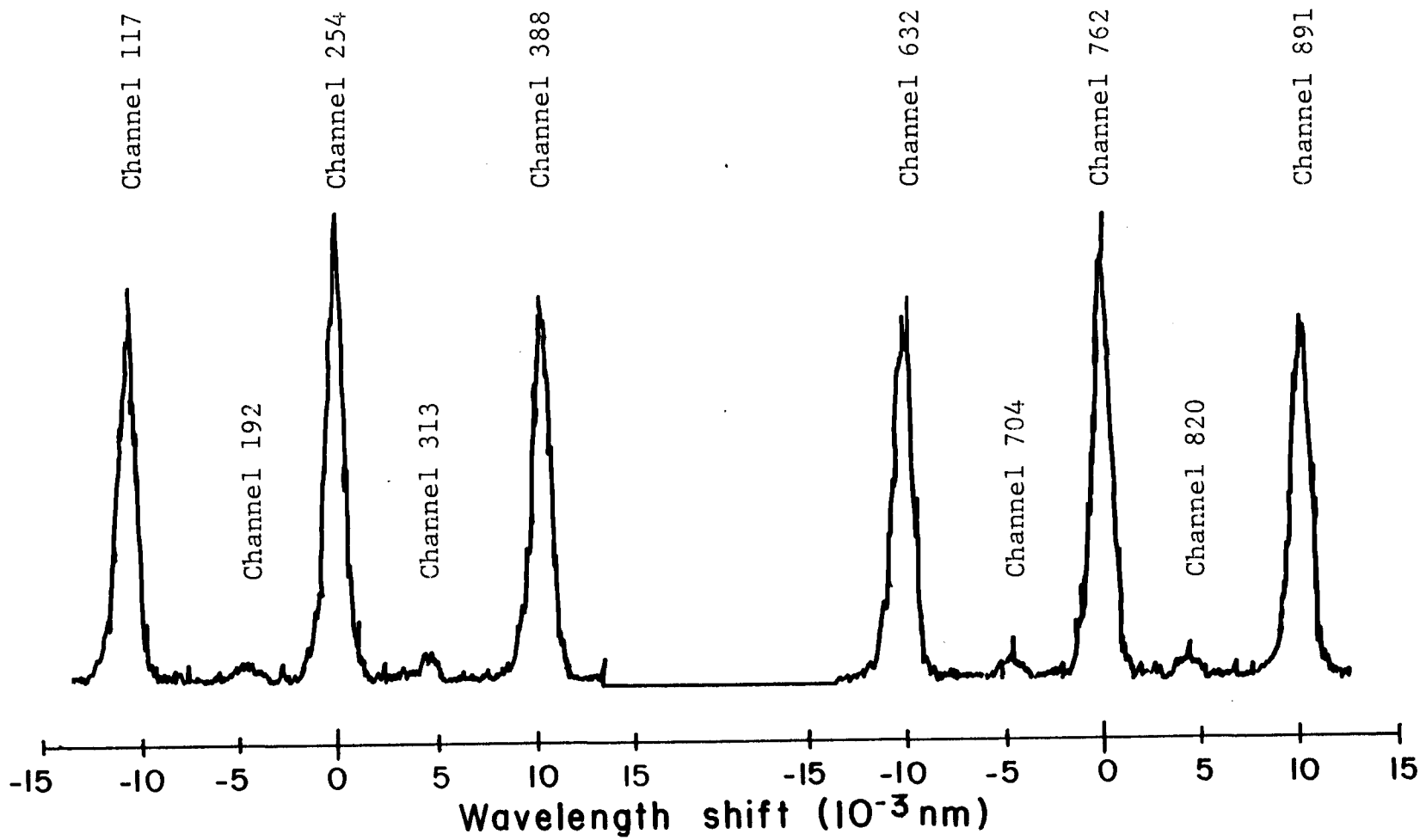

Figure 5.1 MB spectrum of pure KBr crystal (224-80).

$$\Delta\nu_{T_2} = 6.2 \pm 0.10 \text{ GHz} \quad . \tag{5.2}$$

From equation (3.6), the sound velocity associated with each mode, v, is given by

$$v = \frac{\lambda \, \Delta\nu}{n\sqrt{2}} \quad . \tag{5.3}$$

Using values for the index of refraction and density of KBr from Table 3.1, equations (5.1) through (5.3), and equations (3.11) and (3.13), yield

$$\rho v_L^2 = \tfrac{1}{2}(C_{11} + C_{12} + 2C_{44}) = 26.0 \pm 0.7 \text{ GPa} \tag{5.4}$$

$$\rho v_{T_2}^2 = C_{44} = 5.1 \pm 0.3 \text{ GPa} \quad . \tag{5.5}$$

The errors in these measurements arise mainly from the error in the FSR calibration. About one-half of the FSR calibration error comes from discrepancies in the published values of the Hg atomic lines (see Appendix II). Published values of ρv_L^2 and $\rho v_{T_2}^2$ are listed in Table 5.1. The present values agree within experimental error with all published values except the ρv_L^2 value of Kaplan et al.

Only Cummins and Schoen (1972) have observed the transverse mode at $\theta = 90°$. The other values for $\rho v_{T_2}^2$ were calculated from values of the elastic constants obtained at other angles (for which the T_2 mode is

Table 5.1 Published Values of Hypersonic Elastic Constants.

ρv_L^2 (GPa)	$\rho v_{T_2}^2$ (GPa)	Reference
25.3 ± 0.2	5.1 ± 0.1	Braul and Plint, 1980
23.2 ± 0.6	4.7 ± 0.4	Kaplan et al., 1970
25.0 ± 0.3	5.1 ± 0.2	Matsura and Miyazawa, 1973
25.4	5.08	Cummins and Schoen, 1972

actually a mixed mode). The ability to observe the pure transverse mode requires pure, perfect crystals and an instrument with a large finesse.

As discussed in chapter III, the scattering ratio, η_T, is the ratio of the elastic scattering intensity to the MB scattering intensity. The values of η_T for the pure crystals measured in this investigation are listed in Table 5.2. These values are averages of a number of measurements at different points in each crystal; the errors are the standard deviations of these averages. The number of measurements is also given in Table 5.2. From equation (3.23), these scattering ratios range from ~6 to ~200 times the theoretical scattering ratio for a perfect pure crystal, η'_{LP}.

Table 5.2 Scattering from Pure Crystals.

Crystal I.D.	Number of Measurements	η_T	$R_E(10^{-7}\ cm^{-1})$
408	4	2.1 ± 0.4	6.1 ± 1.1
413	3	4.0 ± 1.8	11 ± 3
451	5	5.8 ± 1.6	17 ± 5
751	10	1.0 ± 0.2	2.9 ± 0.6
834	5	1.4 ± 0.2	4.1 ± 0.6
841	6	11 ± 2	32 ± 6
232-79	5	13 ± 4	38 ± 12
235-79	5	11 ± 5	32 ± 14
224-80	3	0.6 ± 0.2	1.5 ± 0.6

The MB scattering coefficient, R_{MB}, may be calculated from equation (3.14) using the constants from Table 3.1; the result is

$$R_{MB} = 1.45 \times 10^{-7}\ cm^{-1} \quad . \tag{5.6}$$

From equation (3.24), the scattering coefficient for extrinsic scattering, R_E, is given by

$$R_E = 2R_{MB}\ (\eta_T - \eta'_{LP}) \quad . \tag{5.7}$$

R_E has been calculated for these pure crystals using equation (5.7) with values for R_{MB} and η'_{LP} from

equations (5.6) and (3.23), respectively. These values are also listed in Table 5.2. The uncertainty in the value of η'_{LP} has little effect on the calculated values for R_E since η_T is considerably larger than η'_{LP} in all these samples.

B. Discussion

Arora et al. (1982) has expanded on work by Mills (1980) and has calculated theoretical scattering cross sections for vacancies and various impurity-vacancy complexes in alkali halides. In general, a scattering cross section, σ, is related to a scattering coefficient at 90°, R, by (Kerker, 1968)

$$R = \left(\frac{3}{16\pi}\right) N\sigma \quad , \tag{5.8}$$

where N is the number of scattering centers per cubic centimeter. Using equation (5.8), R has been calculated for various possible scattering centers in KBr from values of σ given by Arora (1982). These are listed in Table 5.3.

The impurity concentrations in KBr crystals grown in this laboratory by methods similar to the present study were analyzed by induced neutron activation analysis. All impurity levels were in the parts-per-billion range except for Fe^{2+} and Rb^{+} which were measured at

Table 5.3 Scattering Coefficients for Various Scattering Centers in KBr.*

Center	R/N (10^{-28} cm^2)
Cation Vacancy	1.0
Anion Vacancy	158
Pb^{2+} - Cation Vacancy	105
Ca^{2+} - Cation Vacancy	39.2
Fe^{2+} - Cation Vacancy	88.6
BA^{2+} - Cation Vacancy	1.4
Sr^{2+} - Cation Vacancy	15.9
Cd^{2+} - Cation Vacancy	10.0
Rb^{+}	8.0

*With the exception of the Cd^{2+} center, values were calculated from σ values given by Arora et al. (1981) with corrections for λ at 488.0 nm. The value for the Cd^{2+} center was calculated using the method of Arora et al. (1981) with a Cd^{2+} polarizability of 1.8Å (Tessman et al., 1953), and a Cd^{2+} ionic radius of 0.97Å (Handbook of Chemistry and Physics, 1976).

0.04 ± 0.01 ppm and 4.9 ± 0.8 ppm, respectively (Fredericks et al., 1984). From the values for R/N given in Table 5.3, the scattering coefficients for Fe^{2+} and Rb^{+} at these concentration levels are 1.1×10^{-11} cm^{-1} and 7.6×10^{-11} cm^{-1}, respectively. Clearly, the scattering from these types of impurity centers is insignificant in comparison to the extrinsic scattering measured in this study.

The number of Schottky defects in a pure KBr crystal follows a thermodynamic equilibrium expression (Lidiard, 1956)

$$N_c N_a = \exp\left(-g/kT\right) \quad , \tag{5.9}$$

where N_c and N_a are the concentration of cation and anion vacancies, respectively, and g is the free energy of formation of a Schottky defect. If no aliovalent ions are present, then N_c is equal to N_a.

As a crystal grows, vacancy pairs are grown into it at concentration levels associated with a temperature near the melting point. As the crystal is then cooled to room temperature, equation (5.9) dictates that the number of vacancy pairs must decrease. This occurs by either migration of the defects to the crystal surface or by the precipitation of defect clusters within the crystal. The latter process is generally believed to predominate in ionic crystals (Lidiard, 1956). Models

have been proposed for the precipitation process in terms of dislocation jog formation (Eshelby et al., 1958) and simple dislocation core binding (Lifshitz and Geguzin, 1965). The process is reviewed by Whitworth (1973). Of greatest importance here, the vacancies do not exit the crystal, and hence will still contribute to light scattering.

From conductivity measurements on KBr (Chandra and Rolfe, 1971), the number of Schottky vacancies at 730°C is about 1×10^{18} cm^{-3}. At this vacancy concentration, the values of R/N given in Table 5.3 yield scattering coefficients for cation and anion vacancies of $\sim 1.0 \times 10^{-10}$ cm^{-1} and $\sim 0.16 \times 10^{-7}$ cm^{-1}, respectively.

The anion vacancies are thus the major contributor to the scattering by these calculations. However, the calculated anion vacancy scattering is still only about 0.1 times the extrinsic scattering of the lowest scattering sample measured (224-80).

A likely explanation for this discrepancy is the precipitation of the grown-in defects into larger aggregates in order that the number of free defects follow equation (5.9). From equation (3.25), Rayleigh scattering is proportional to the square of the particle volume. Hence, for a given total volume of scattering material the scattering will be directly proportional to the average volume of the individual scattering units.

With so few crystals, it is difficult to draw positive conclusions regarding the effects of the crystal growth conditions on the scattering power. However, a few tentative remarks are in order. Referring to Tables 2.1 and 5.2, the crystals treated with oxidizing gasses (Cl_2 and/or O_2) seem to have either very large or very small scattering powers. Crystals 232-79 and 235-79 were grown from an iron-doped melt; and, although no iron was detected in the crystal, the detection limit for AA analysis of iron is quite high (~0.7 mppm). This could well be the reason for the anomalously large scattering power in these crystals. Additionally, crystal 232-79 was reseeded, which can increase grown-in dislocations. Crystal 841 was cooled to room temperature over a 23-hour period, and this allowed more time for defect aggregation. The three crystals with the smallest scattering power were all cooled quickly (751, 834, and 224-80). Crystals 413, 451, and 408 were also cooled quickly, but these crystals were not treated with an oxidizing gas. An oxidizing gas removes organic impurities by forming more volatile compounds.

VI. SCATTERING MEASUREMENTS ON DOPED SAMPLES

A. Theory of Scattering by Precipitate Phases

Scattering from a given number of scattering particles is enhanced if those particles precipitate into larger aggregates. When precipitation occurs, the number of scattering particles is decreased; but since the particle radius term in equation (3.25) is raised to the sixth power, the scattering power of the new collection is larger.

Equation (3.25) may be written in terms of the average volume and number density of precipitate particles, V_P and N_P, respectively, yielding

$$R_R = \frac{9\pi^2 N_P V_P^2}{\lambda_i^4} \left[\frac{n^2 - 1}{n^2 + 2} \right]^2 \quad . \tag{6.1}$$

Here λ_i is the wavelength of the light inside the sample (i.e., $\lambda/1.572$ in KBr), and n is the refractive index of the particle relative to the refractive index of KBr. If the average number of individual divalent cations making up a precipitate particle is N_x, the V_P is given by

$$V_P = V_I N_x \quad , \tag{6.2}$$

where V_I is the volume associated with each divalent

cation in the precipitate. From conservation of mass,

$$N_x = \frac{N - N_o}{N_P} \quad , \tag{6.3}$$

where N is the total number density of divalent cations (i.e., the analytical concentration), and N_o is the solubility of the divalent cation. Combining equations (6.2) and (6.3) yields

$$V_P = \frac{(N - N_o)V_I}{N_P} \quad . \tag{6.4}$$

Combining equations (6.4) and (6.1) yields

$$R_R = \frac{9\pi^2(N - N_o)V_I V_P}{\lambda_i^4} \left[\frac{n^2 - 1}{n^2 + 2} \right]^2 \quad . \tag{6.5}$$

Thus, for $N > N_o$, the scattering coefficient will be a linear function of concentration if V_I and V_P are independent of N.

In fact, the volume of the precipitate particles probably increases somewhat with concentration. A precipitation process consists of two stages: the nucleation of precipitate particles, followed by Ostwald ripening of those particles. If the nucleation process is homogeneous, the number of nucleated particles is

proportional to the concentration of the impurity (Hughes, 1982). Thus, the number of precipitating particles is proportional to N, whereas from equation (6.4) N_P must be proportional to $(N - N_o)$ for V_P to be independent of N. When N_o is small (i.e., for very insoluble precipitates), the scattering coefficient is expected to be more nearly linear with respect to concentration.

Despite this inherent inaccuracy, the assumption of constant V_P allows an estimation of the average particle size within a precipitation region. The actual particle size will be somewhat larger at high concentrations and somewhat smaller at low concentrations.

η_T may be referenced to R_{MB} in a similar manner to that described in chapter V, yielding

$$\eta_T = \frac{9\pi^2(N - N_o)V_I V_P}{2R_{MB}\,\lambda_i^4}\left[\frac{n^2 - 1}{n^2 + 2}\right]^2 . \qquad (6.6)$$

The constants in equation (6.6) yield

$$\eta_T = 4.594(C - C_o)V_I V_P\left[\frac{n^2 - 1}{n^2 + 2}\right]^2 . \qquad (6.7)$$

Here V_I and V_P must have units of nm^3, and C and C_o are

impurity concentrations in μ-moles of impurity per mole of KBr ($N = C \times 1.393 \times 10^{16}$ when N is in cm^{-3}).

B. Results

Three regions of each sample were viewed with the MB spectrometer. These regions were the top, center, and bottom relative to the growth axis of the original crystal. As discussed in chapter II, the dopant concentration increases from top to bottom in each crystal. The dopant concentration at each sample point has been calculated as described in chapter II. Details of the heat treatments given the samples is also in chapter II.

Graphs of η_T versus concentration are shown in Figures 6.1 through 6.3 for quenched and annealed samples containing Ca^{2+}, Cd^{2+}, and Pb^{2+} dopants. The numerical data are listed in Appendix IV. The instrumental uncertainty in η_T at each sample point was insignificant on the scale of these graphs. The error bars have been calculated from variations in η_T occurring between the three sample points described above. In most cases, this variation is much larger than can be accounted for by the small concentration gradient within the samples, and thus yields a liberal value for the uncertainty in η_T. All three sample points have been included individually for completeness.

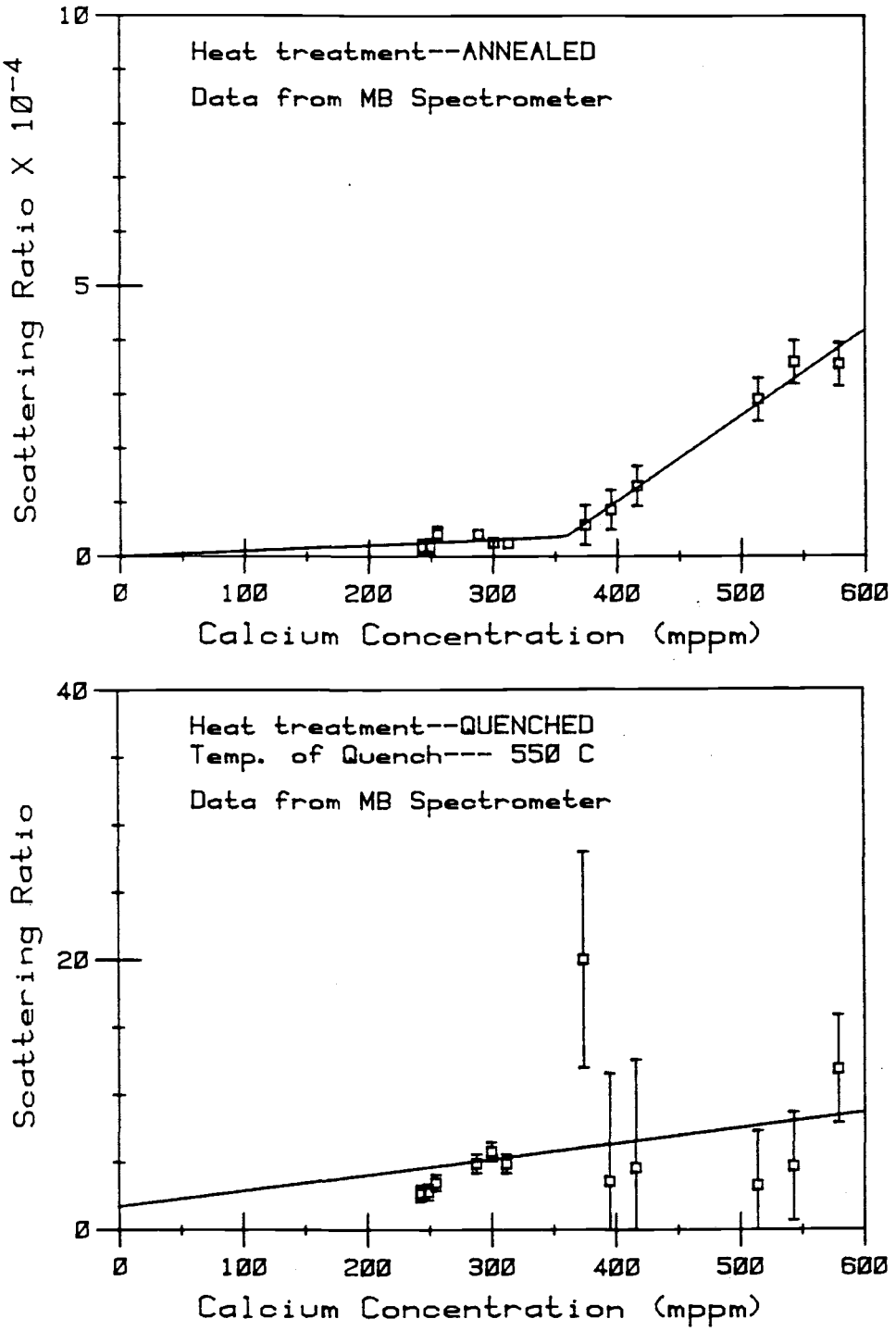

Figure 6.1 Plot of the scattering ratio, η_T, versus calcium concentration in KBr crystals.

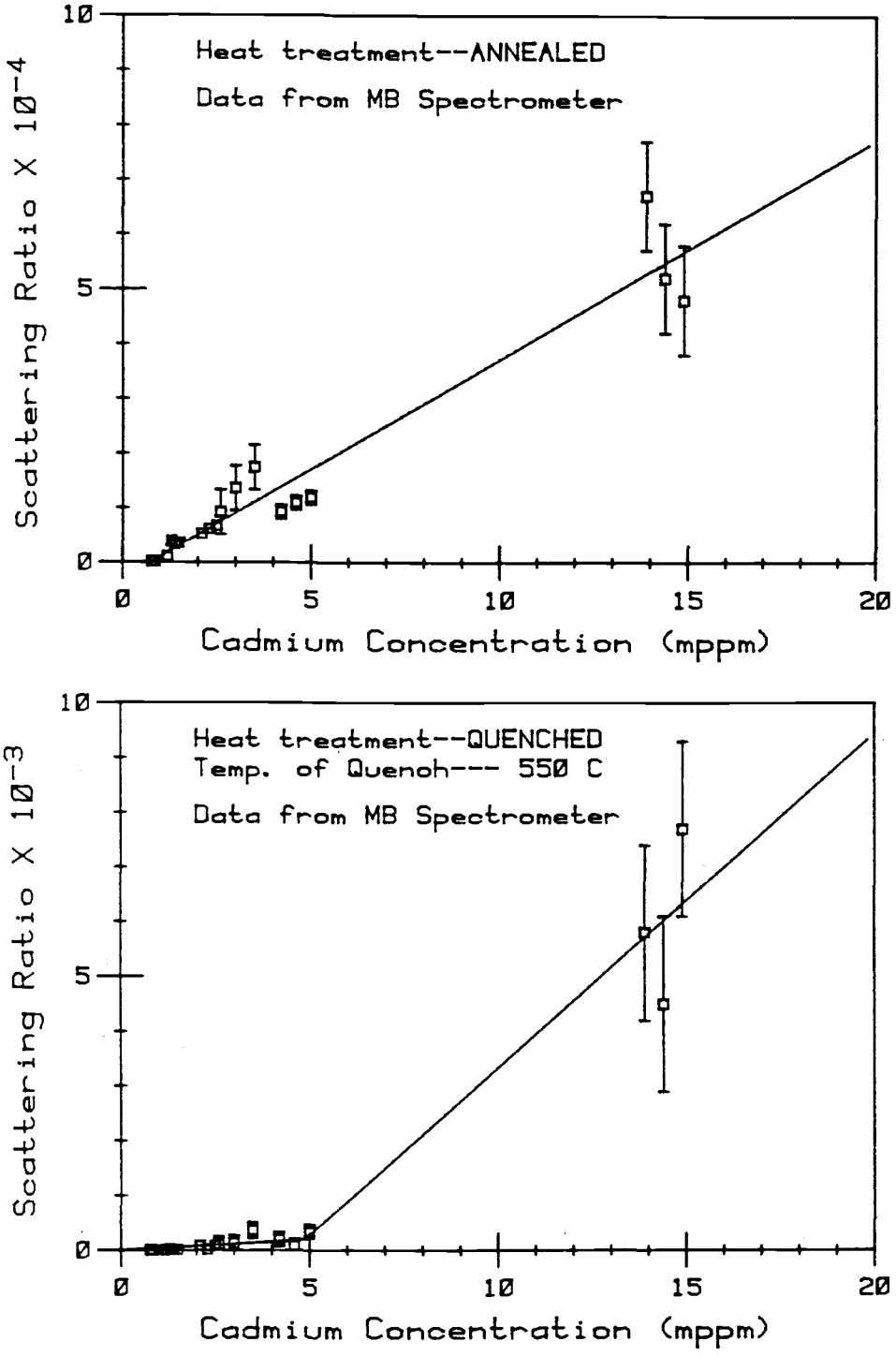

Figure 6.2 Plot of the scattering ratio, η_T, versus cadmium concentration in KBr crystals.

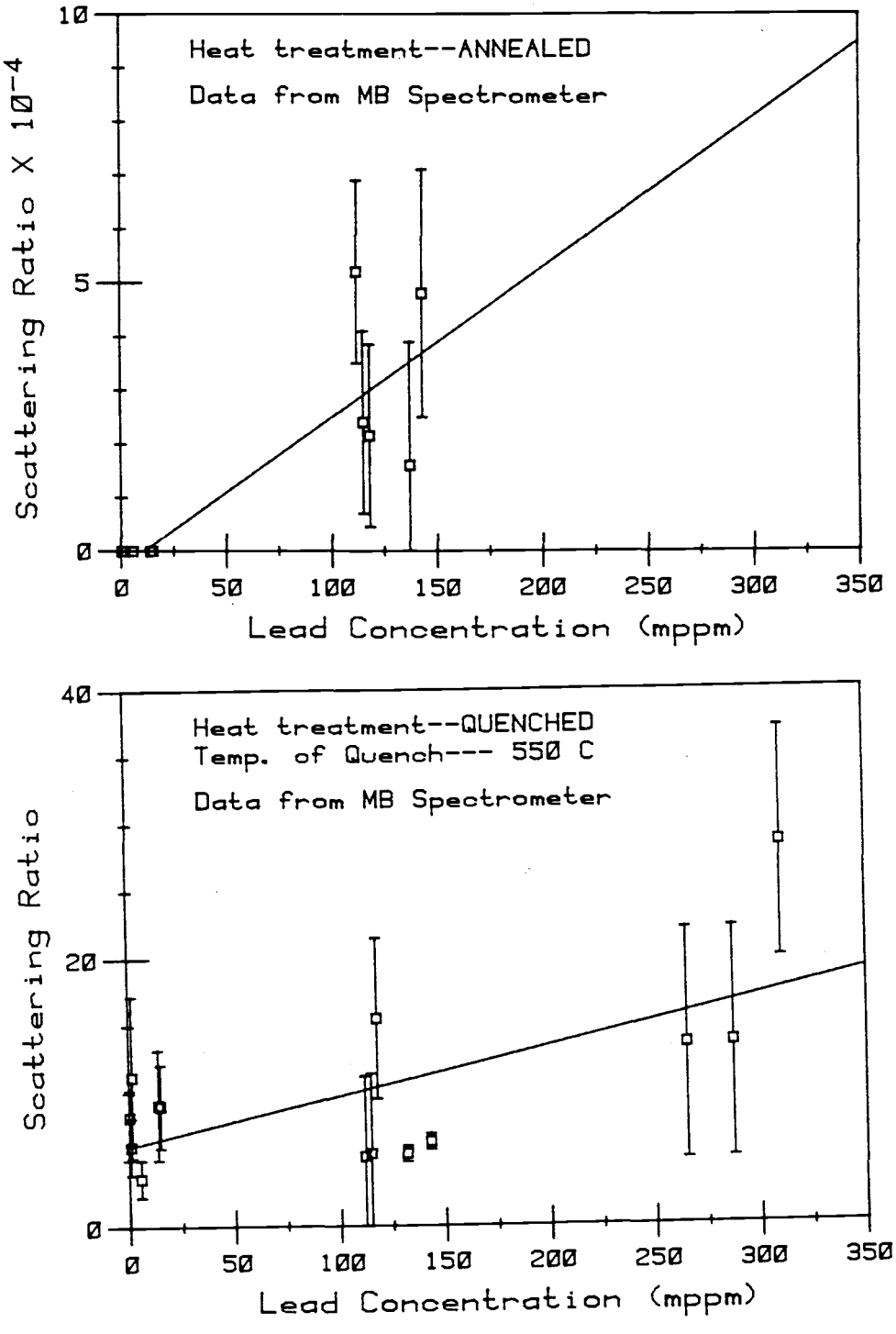

Figure 6.3 Plot of the scattering ratio, η_T, versus lead concentration in KBr crystals.

The variation in η_T within each sample is very pronounced (particularly in the annealed samples). This variation is not instrumental; the two spectral orders observed in each spectrum yield nearly identical scattering ratios. This variation must be due to an inhomogeneous distribution of scattering centers.

Also demonstrated by these graphs is the markedly decreased scattering in the quenched samples relative to the annealed samples. This indicates the formation of large impurity aggregates upon annealing. The formation of these aggregates was observed to occur only above a limiting solubility, C_o, which is characteristic for the specific impurity. For the lead data, the uncertainties in the scattering ratio are so large that it is impossible to determine a concentration functional dependence from these data alone. From other scattering measurements to be discussed below, lead also exhibits a solubility limit for aggregate formation.

The three impurities show some distinct differences. C_o for the annealed cadmium doped samples is significantly lower than for the lead or calcium doped samples. Also, the concentration dependence of the scattering in the cadmium doped samples is very much larger. In the quenched cadmium doped samples, η_T is reduced, but not to the level observed in the lead and calcium doped samples.

As mentioned previously, the annealed lead doped samples have large variations in η_T within each sample. The greater variation in the lead samples is probably due to the longer annealing time given them (see Figure 2.5). The Ostwald ripening of a precipitate consists of the growth of larger particles at the expense of smaller ones. This process increases the inhomogeneity of the impurity distribution (Jain and Hughes, 1978).

Additional scattering information was obtained with the scattering polarization (SP) spectrometer. Since the SP instrument measures the total scattering from the samples, no MB peak is available for internal standardization of the intensity. However, by plotting the scattering ratio from the MB spectrometer versus the intensity from the SP spectrometer, a calibration curve for the SP measurements can be obtained. This plot is shown in Figure 6.4. The straight line is a linear least squares fit to the data with statistical weighting of the points relative to the uncertainty in the η_T values. The slope and intercept are listed on the graph; the errors in these quantities are calculated from statistical variations in the least squares fit.

The SP intensity data and the scattering ratios calculated from them are listed in Appendix IV. Graphs of η_T versus concentration for Cd^{2+} and Pb^{2+} doped

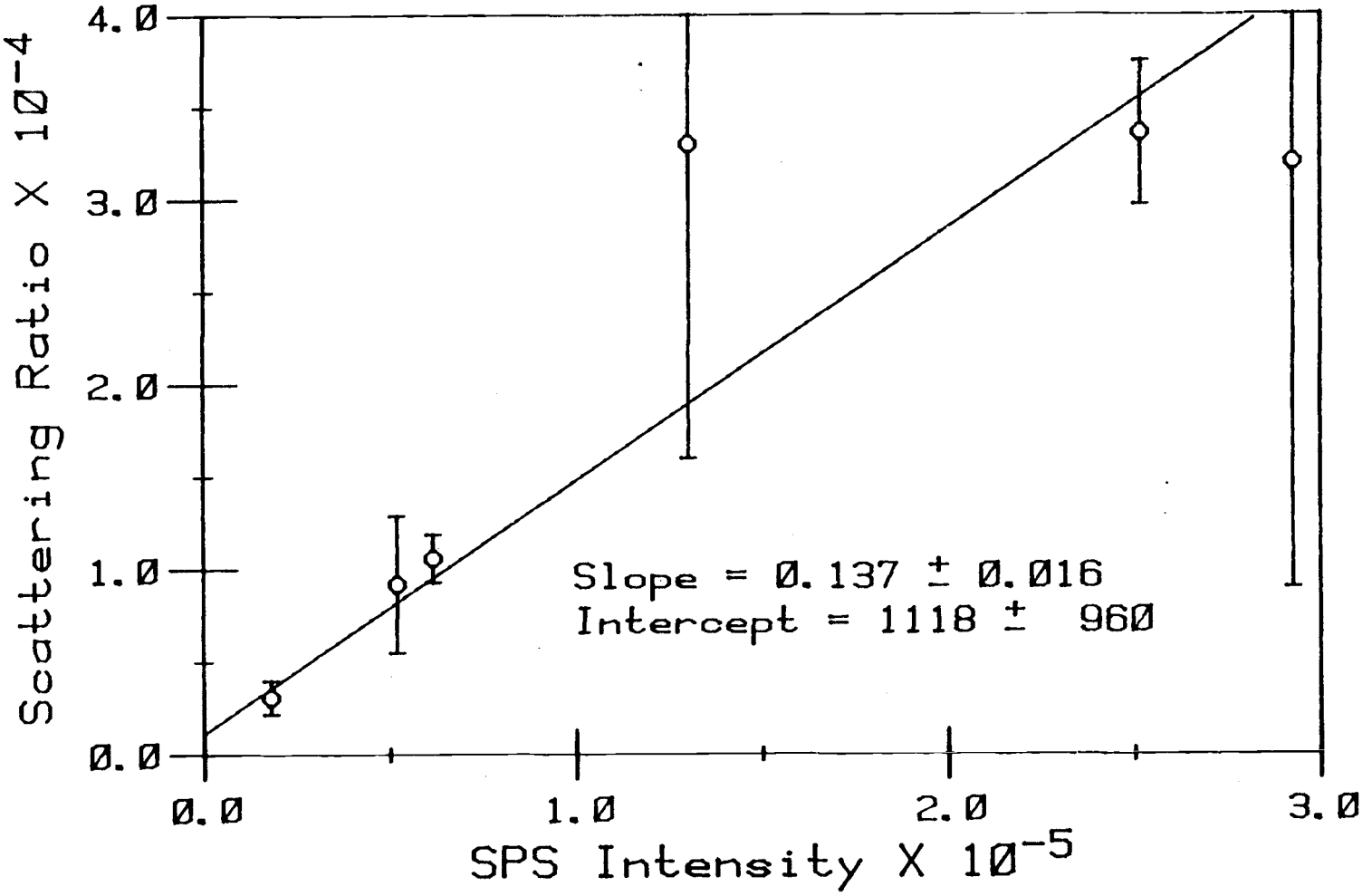

Figure 6.4 Plot of the scattering ratio from the MB spectrometer versus the scattering intensity from the SP spectrometer for various samples. The two points with the large errors are lead doped samples.

samples are shown in Figures 6.5 and 6.6. For samples not measured with the SP spectrometer, η_T has been calculated from the MB data. These two sources are designated as such on the graphs. The data for calcium doped samples are not shown since there is little difference between the SP data and that from the MB spectrometer.

These new plots clearly demonstrate the validity of the qualitative descriptions of the MB scattering plots. In particular, the annealed lead doped samples clearly yield a C_o value above which aggregation of the impurities greatly enhances the scattering.

The plots of the annealed samples and of the quenched cadmium doped samples have been fitted with two intersecting straight lines. The intersection point, C_o, was chosen to yield the best fit (minimum squared deviations). The equations are

$$\eta_T = b_1 C \quad ; \text{ for } C < C_o \qquad (6.8)$$

and $$\eta_T = b_1 C + b_2 (C - C_o) \quad ; \text{ for } C > C_o \quad , \qquad (6.9)$$

where b_1 and b_2 are the slopes in the two regions.

When C is less than C_o, there appears to be little aggregation of impurities. From conductivity studies (Rolfe, 1964) it is expected that the impurities are associated with a cation vacancy; but aggregation of these impurity-vacancy pairs into precipitates does not

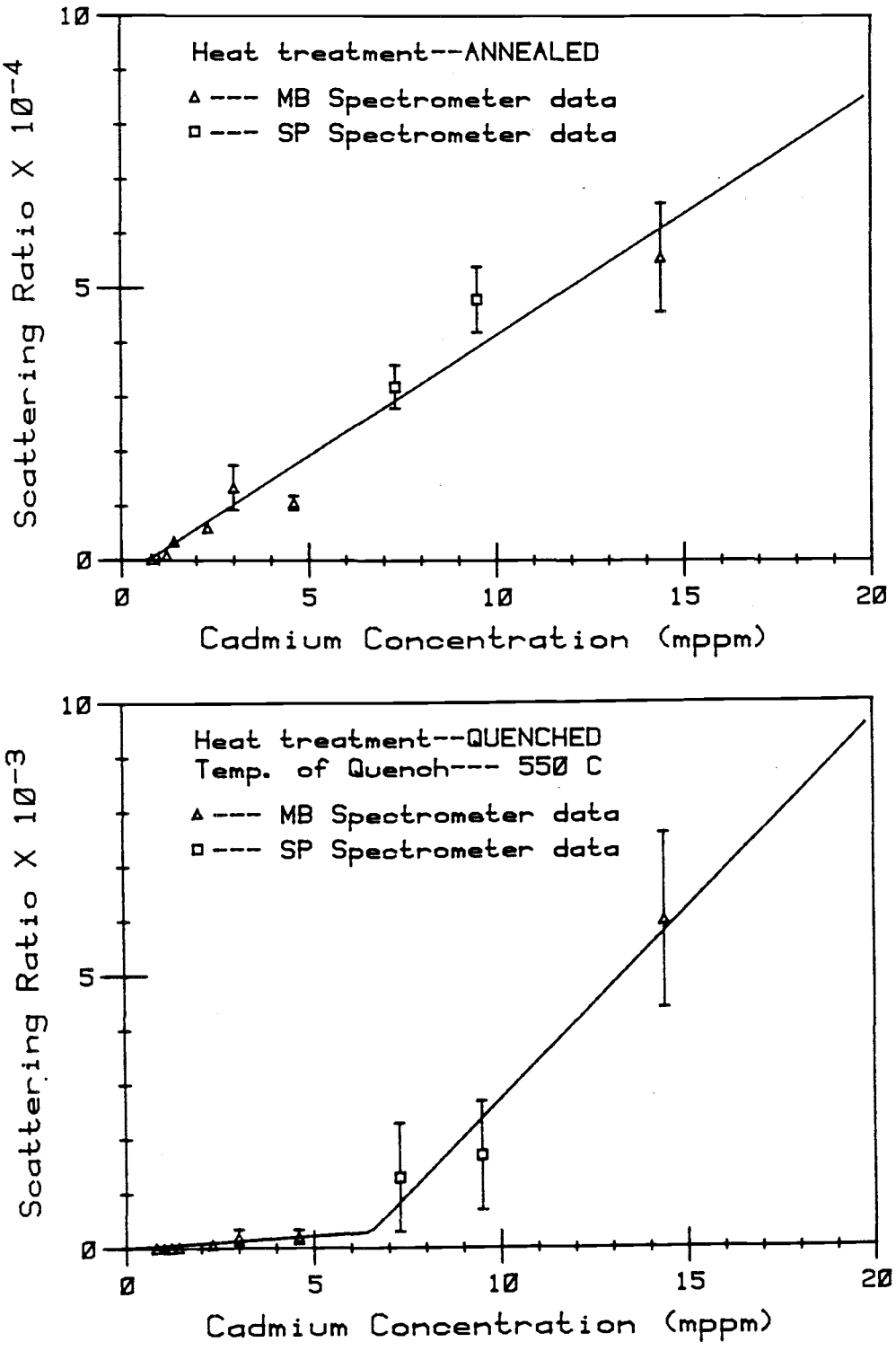

Figure 6.5 Plot of the scattering ratio versus cadmium concentration in KBr crystals. Data are from two different instruments.

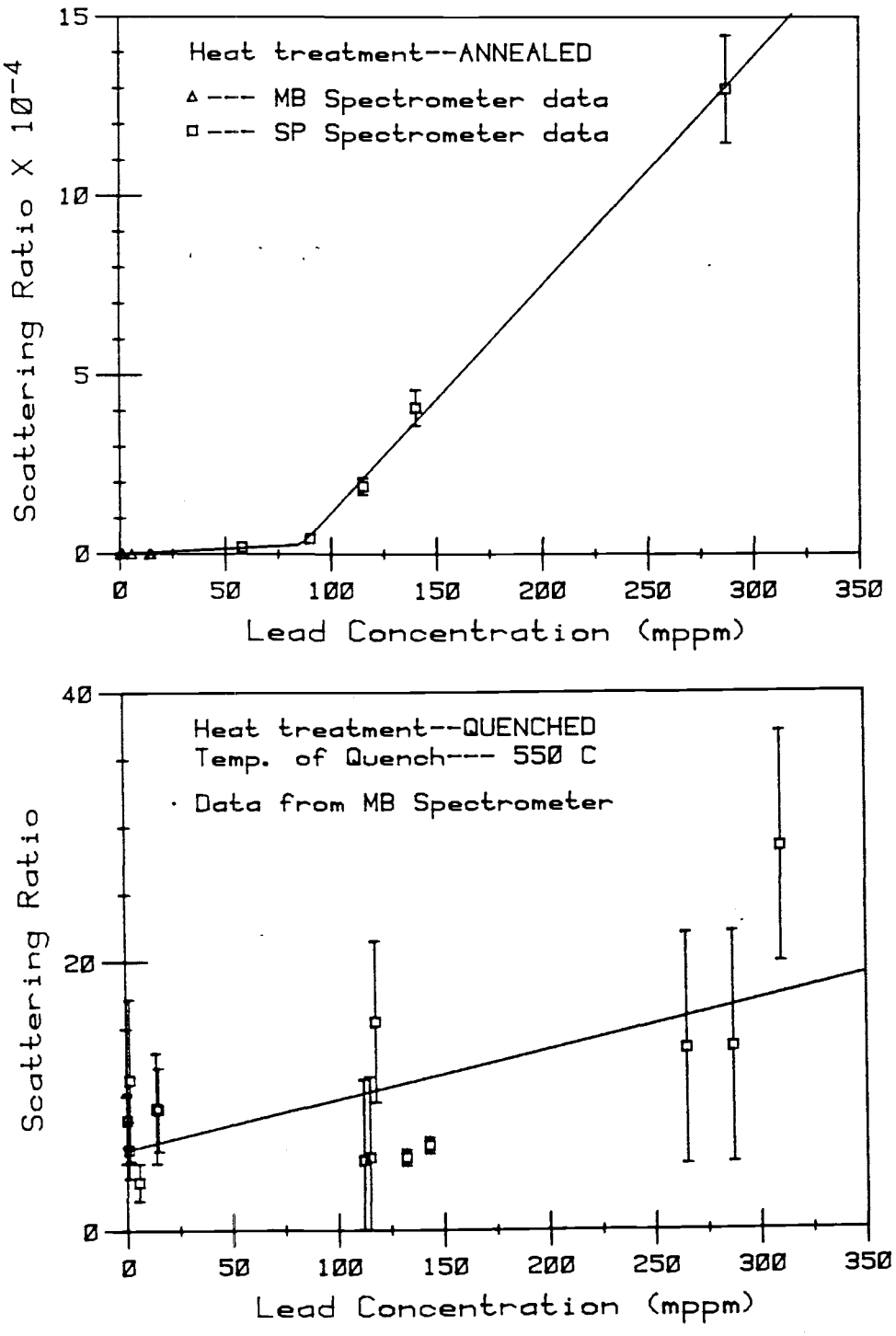

Figure 6.6 Plot of the scattering ratio versus lead concentration in KBr crystals. Data is from two different instruments.

seem to occur below C_o. Thus from equation (3.25) the scattering is expected to be linear with respect to concentration.

When C is greater than C_o, precipitation must occur to account for the large increase in the concentration dependence of the scattering. As discussed in section A of this chapter, the scattering in the cluster region is not expected to be exactly linear with respect to concentration; but the slope, b_2, will be useful for order-of-magnitude estimates of precipitate particle size and character.

The values of b_1, b_2, and C_o from the preceding graphs are listed in Table 6.1. A more detailed description of the precipitate particles will be given in the discussion section.

Plots of the scattering ratio versus concentration for lead doped samples which have been quenched from different temperatures are shown in Figure 6.7. The samples quenched from 200°C more closely resemble the annealed samples, while those quenched from 350°C more closely resemble the samples quenched from 550°C. This indicates that the solubility of lead increases with temperature, as would be expected.

The wavelength dependence of the SP spectrometer data is useful for observing the wavelength dependence of ratios of the four polarization configurations

Table 6.1 Experimental Quantities from Scattering Ratio Versus Concentration Plots.

Dopant	Heat Treatment	$b_1(mppm)^{-1}$	$b_2(mppm)^{-1}$	$C_o(mppm)$	Instrument
calcium	Annealed	10±10	160±15	360±30	MB
cadmium	Annealed	0	4000±500	0.7±0.7	MB
cadmium	Annealed	0	4500±400	0.7±0.5	SP & MB
lead	Annealed	0.7 ±0.7	280±100	>11	MB
lead	Annealed	30±6	640±20	86±5	SP & MB
calcium	Quenched (550°C)	0.01±0.01	--	--	MB
cadmium	Quenched (550°C)	40±15	600±200	>4.9	MB
cadmium	Quenched (550°C)	45±20	700±200	6.5±2	SP & MB
lead	Quenched (550°C)	0.04±0.01	--	--	MB
lead	Quenched (350°C)	0.03±0.02	2.	265±50	MB
lead	Quenched (200°C)	0.21±0.08	50±10	50±30	MB

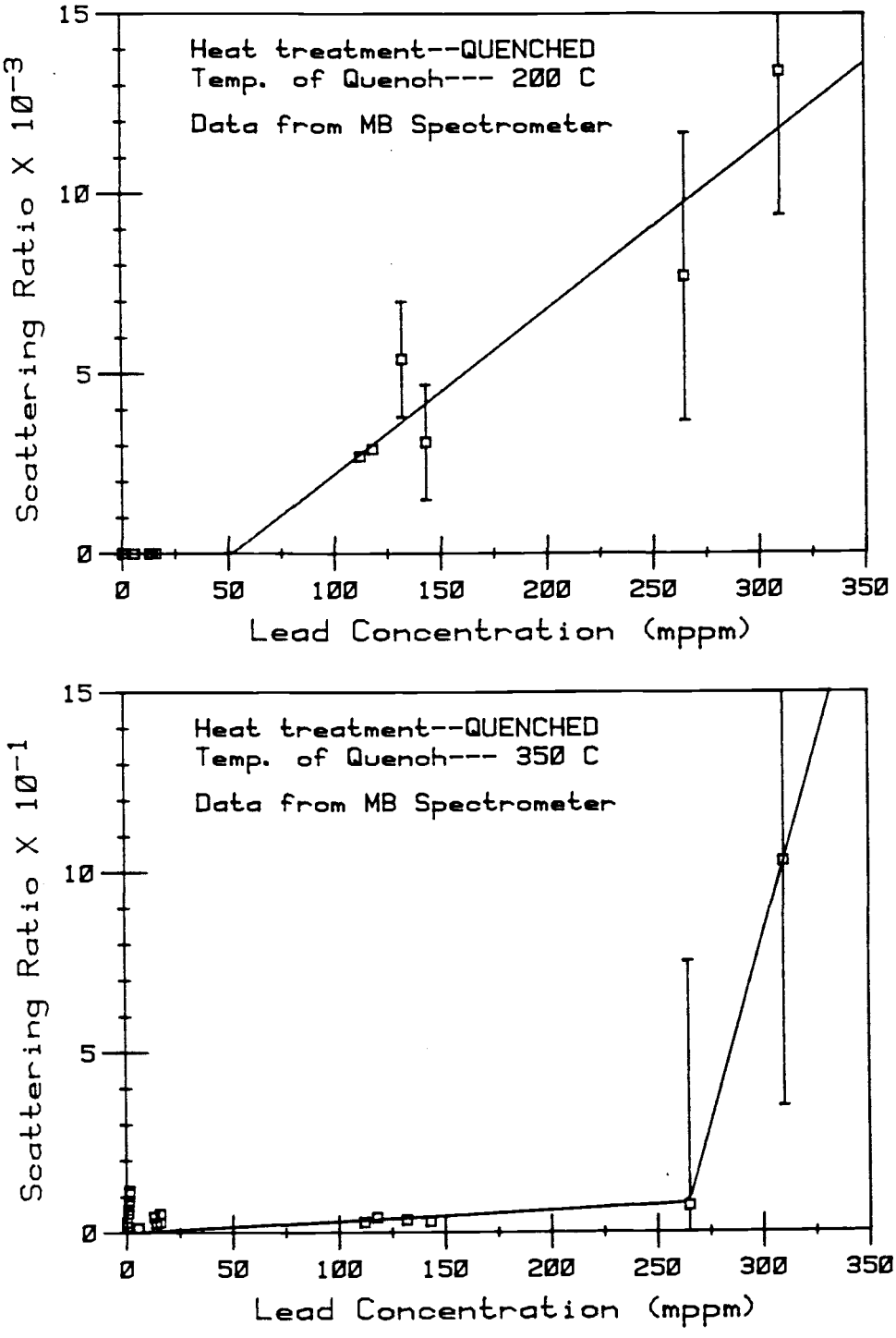

Figure 6.7 Plots of the scattering ratio of lead doped samples which have been quenched from two different temperatures.

(equations (3.45) through (3.48)). The wavelength dependence of the absolute intensity could not be measured accurately. In particular, equations (3.45) through (3.48) yield

$$\frac{R_{VV} + R_{HH} - 2R_{HV}}{R_{VV} + R_{HH} + 2R_{HV}} = \frac{S_{22}}{S_{11}} \quad . \tag{6.10}$$

This ratio is of interest since S_{22} is equal to S_{11} when the scattering is from spherical particles (equations (3.32) through (3.34)). Another ratio of interest is

$$\frac{R_{HH} - R_{HV}}{R_{VV} - R_{HV}} = \frac{S_{22} + S_{12}}{S_{22} - S_{12}} \quad . \tag{6.11}$$

When the scattering is from small particles, S_{22} is equal to $-S_{12}$ (equations (3.28) and (3.29)), and this ratio will be equal to zero.

These two ratios are shown in Figures 6.8 through 6.10 for two concentrations of each dopant (calcium, cadmium, and lead). The discussion of these plots will be left to the next section.

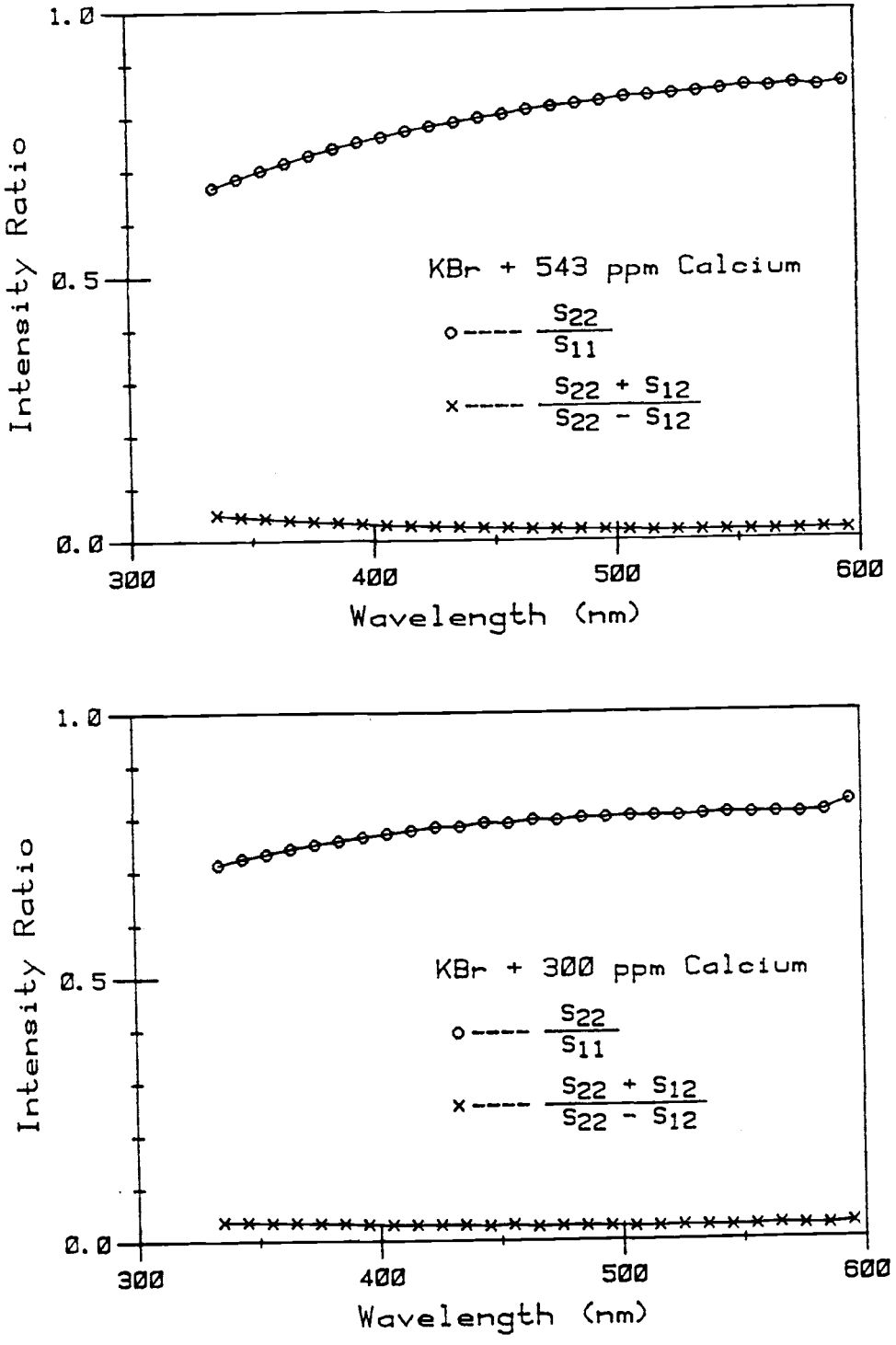

Figure 6.8 Plots of the wavelength dependence of scattering for two polarization intensity ratios. Two extreme concentrations of calcium in KBr crystals are shown.

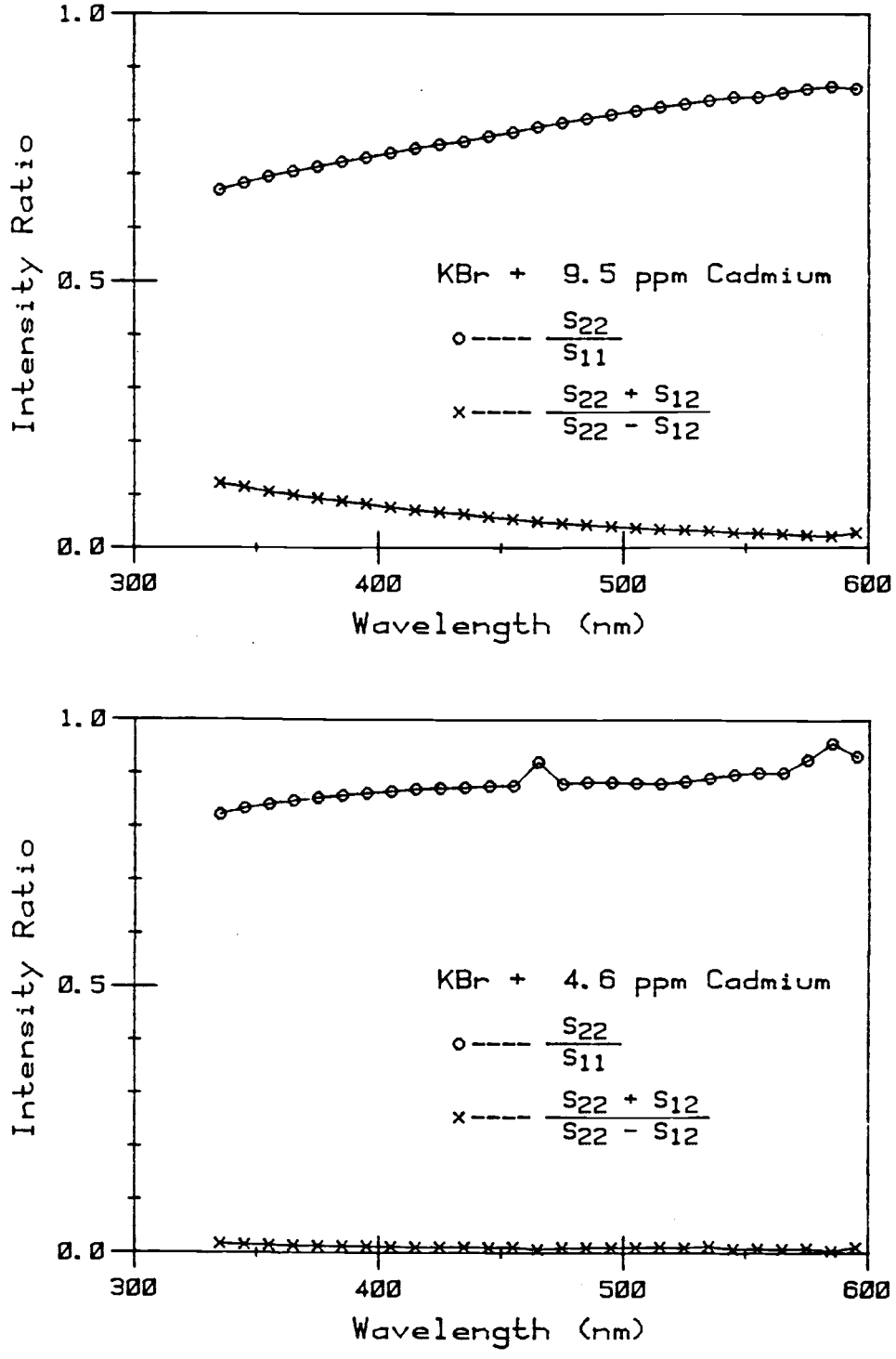

Figure 6.9 Plots of the wavelength dependence of scattering for two polarization intensity ratios. Two extreme concentrations of cadmium in KBr crystals are shown.

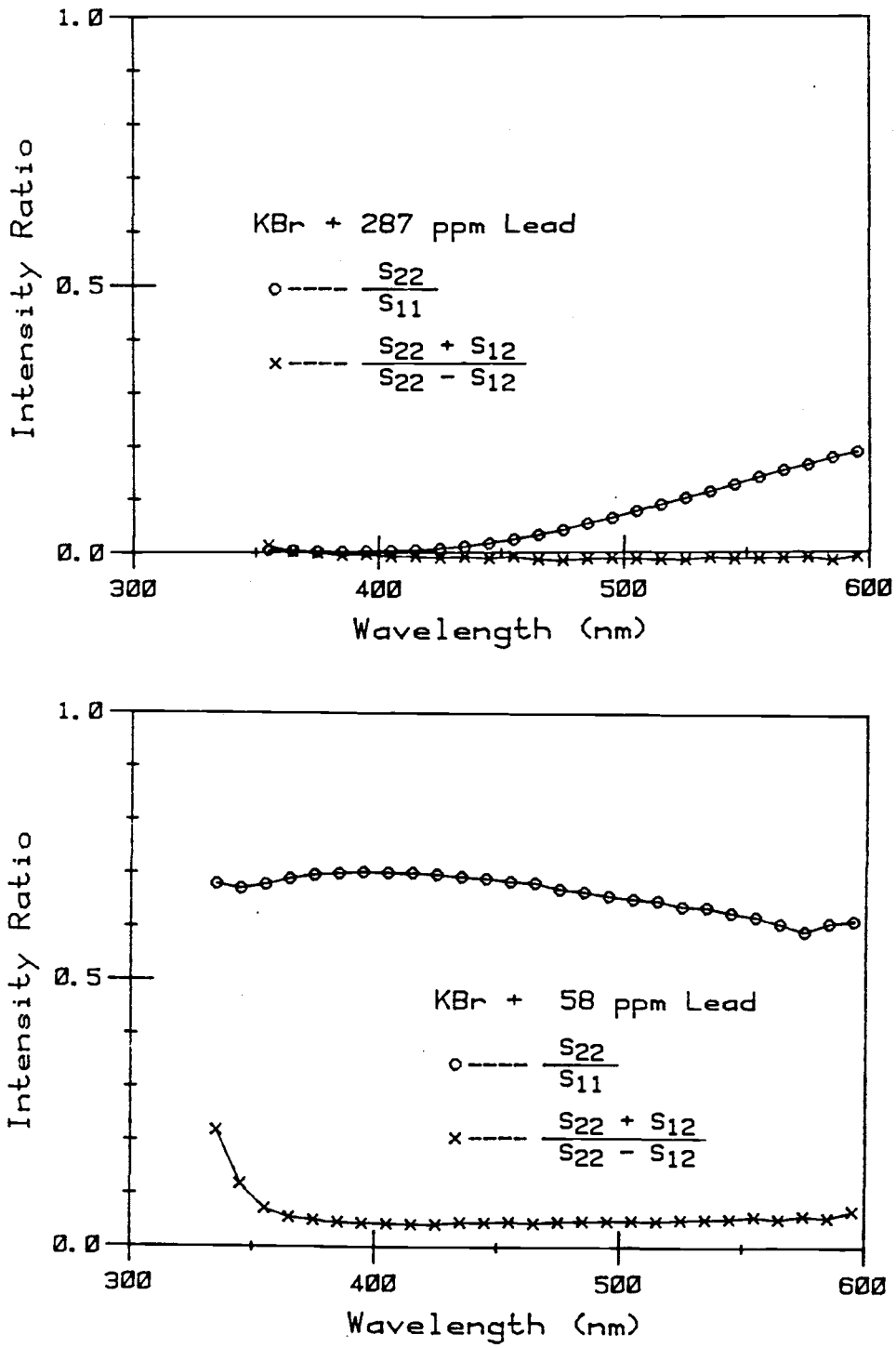

Figure 6.10 Plots of the wavelength dependence of scattering for two polarization intensity ratios. Two extreme concentrations of lead in KBr crystals are shown.

C. Discussion

1. Solubilities

The solubilities obtained from the light scattering measurements (Table 6.1) follow the same general trend among the dopants as the distribution coefficients given in Table 2.2. The ionic (crystal) radii of the three dopants are 0.99Å for Ca^{2+}, 0.97Å for Cd^{2+}, and 1.20Å for Pb^{2+}; the ionic radius of K^{+} is 1.33Å (Pauling, 1960). Thus, the relative stability of the solvated ions is not a function of the ionic radius.

Ikeya (1974) has measured the distribution coefficient for a number of transition metal ions in KCl and NaCl. A general trend of decreasing distribution coefficient with increasing number of d electrons was observed. The present results are in agreement with these results for calcium and cadmium in KBr.

2. Particle Size

Using equation (6.7), the volume of a scattering particle can be calculated only if the volume of an individual particle component, V_I, and the relative

refractive index of the particle, n, are known. Two possible models for the composition of a scattering particle are discussed below.

Model 1: The precipitate consists of the normal divalent metal bromide. In this case, the index of refraction and unit cell volume of the divalent metal bromide can be used in equation (6.7) for n and V_I. The values of these parameters are listed in Table 6.2 for several compounds.

Table 6.2 Index of Refraction and Unit Cell Volume for Several Materials.

Compound	Unit Cell Volume (nm^3) (1)	n_I/n_{KBr} (2)
KB_r	0.0712	1.0
$CaBr_2$	0.084	1.1 (4)
$CdBr_2$	0.097	1.13
$PbBr_2$	0.091	1.61
$CaCl_2$	---	1.05 (3)

(1) from Wyckoff (1963).
(2) KBr and $PbBr_2$ values are from A.I.P. Handbook (1963), and $CdBr_2$ is from Matsumoto et al. (1977).
(3) estimated from measured values of molten $CaCl_2$ (Marcoux, 1971).
(4) estimated from the value for $CaCl_2$.

Model 2: The precipitate consists of clusters of impurity-vacancy complexes. In this case, the unknown quantities on the right-hand side of equation (6.7) can be obtained from the value of the scattering coefficient, R, for an individual complex. Values for R/N are listed in Table 5.3. In the derivation of these values (Arora et al., 1982), the volume of the complex was assumed to be twice the unit cell volume of KBr. According to the present model, this is also the volume of an individual complex in a cluster. A rearrangement of the Rayleigh scattering equation yields

$$V_I \left(\frac{n^2 - 1}{n^2 + 2} \right) = \frac{(R/N)\ \lambda_i^4}{9\pi^2 V_I} \qquad (6.12)$$

The left-hand side of equation (6.13) is the required unknown quantity in equation (6.7). The value of the unit cell volume of KBr is listed in Table 6.2.

The values of V_P calculated from the two models for the structure of a cluster are listed in Table 6.3. Also listed in Table 6.3 are values for the radius of the particles, assuming V_P is spherical. Spherical particles have been tacitly assumed throughout this discussion.

Table 6.3 Volumes and Radii of Scattering Particles for Two Precipitate Models.

Dopant	Model 1		Model 2	
	$V_p(10^4 nm^3)$	a_p(nm)	$V_p(10^5 nm^3)$	a_p(nm)
Ca^{2+}	9.6	28	4.2	46
Cd^{2+}	130	67	120	140
Pb^{2+}	1.3	14	6.2	53

The particle sizes calculated from Model 2 are larger since the structure is less densely packed. For particles as large as these, a Model 2 structure would certainly collapse to the Model 1 case. However, the Model 2 structure allows for the possible inclusion of K^+ ions in the structure, with a volume increase proportional to the K^+ mole fraction. Separate phases of this type with a 6:1 ratio of Cd^{2+} to Na^+ in NaCl were first identified as a separate phase by Suzuki (1960). Since that time, Suzuki phases have been identified for Mn^{2+} in NaCl (Kirk et al., 1975) and Pb^{2+} in KCl (Bertoldi et al., 1980). Although no Suzuki phases have been reported for the present constituents, their formation is a definite possibility.

The particle sizes calculated by either model are large enough to be approaching the upper limit of validity for dipolar (Rayleigh) scattering. The Rayleigh scattering theory is valid for particles with radii less than approximately 0.05λ. In Figures 6.8 through 6.10, the intensity ratio $(S_{22} + S_{12}) / (S_{22} - S_{12})$ gives a measure of the deviation from the Rayleigh limit.

The spectra of the calcium doped samples show only a marginal deviation from zero, indicating that the calcium particle size is within or near the Rayleigh limit.

The spectrum of KBr containing 9.5 mppm cadmium shows a deviation from zero at shorter wavelengths. This is to be expected, considering the large particle size estimated by both clustering models. The spectrum of KBr containing 4.6 mppm cadmium does not show any deviation from zero, indicating that the presumption of constant particle size at concentrations greater than C_o is not strictly valid.

Since the criterion for the Rayleigh limit is based on particle size relative to the wavelength of the incident light, the intensity ratio is expected to increase at shorter wavelengths. This was observed in the calcium- and cadmium-containing samples. In the KBr +58 mppm lead spectrum, the lack of any significant

wavelength dependence in the intensity ratio is an indication of a particle-shape effect. The slightly negative intensity ratio for the more concentrated lead sample is further evidence of an anisotropic particle shape.

3. Particle Shape

The intensity ratio S_{22}/S_{11} in Figures 6.8 through 6.10 gives a measure of the shape anisotropy of the scattering particles. S_{22}/S_{11} is equal to one (1) for spherical particles.

The calcium and cadmium doped samples show some deviation from sphericity; but because of the sensitivity of this ratio to even moderate shape changes, the particles are probably roughly spherical. Asano and Sato (1980) calculated theoretical deviations of roughly this magnitude for spheroids with axis ratios as small as 2.

The lead doped samples demonstrate extreme deviations from a spherical shape. It is possible that lead tends to preferentially precipitate along dislocation lines. This explanation was proposed by Plint and Sibley (1965) to explain a similar anisotropy for lead in sodium chloride.

VII. ABSORPTION SPECTRA

A. Historical Perspective

The electronic absorption spectra of impurity ions in alkali halide crystals have been extensively studied for many years. A complete literature review will not be attempted here, and the reader is referred to reviews by Jain (1971), Radhakrishna and Chowdari (1977), and numerous other reviews and books on the subject. The major issues will be discussed below, followed by a discussion of some specific investigations relevant to the current study.

The absorption bands of well-dispersed impurities have generally been well characterized for most of the common impurities in KBr and other alkali halides. The effects of thermal treatment and high-energy irradiation on impurity centers has also been extensively studied; however, the definitive reconciliation of absorption bands with specific structural centers has often proved an elusive goal.

Thermal treatment, particularly annealing at moderate temperatures generally leads to aggregate impurity centers. This is associated with a broadening of the impurity bands. The aggregate bands are generally broad and weak, making their discrimination from unknown

sources difficult; many inconsistencies exist among investigators.

Irradiation of alkali halides with X-rays leads to the formation of trapped electron and trapped hole-type centers. The trapped electron centers include the F-center and its associated decay products. The trapped-hole centers include the V centers in pure cyrstals and the D centers in crystals doped with divalent cations.

The absorption spectrum of s^2 configuration ions (Tl^+, Sn^{2+}, Pb^{2+}, etc.) in alkali halides generally consists of four bands designated by A, B, C, and D (Fowler, 1968). The A-band is attributed to the spin-orbit allowed $^1S_o \rightarrow {}^3P_1$ transition. The B-band is attributed to a vibration-assisted $^1S_o \rightarrow {}^3P_2$ transition. The C-band is attributed to the dipole-allowed $^1S_o \rightarrow {}^1P_1$ transition; and the D-band is a perturbed exciton band. Fukuda (1964) has observed an additional D'-band in Pb^{2+} doped KCl and NaCl. By observing the temperature dependence of the peak areas and widths in lead doped KBr, Chaney et al. (1974) have definitively matched these transitions to the observed absorption bands. The A-band is expected to be split into a doublet by the Jahn-Teller effect. Tsuboi et al. (1975) have shown that the splitting constant for lead in KBr is very small, hence this expected splitting is not observed.

Jain and Radhakrishna (1968) have observed the absorption spectrum of KBr containing Cd^{2+}. They found room-temperature absorptions at 280 nm, 215 nm, and 202 nm. However, no background subtraction has been indicated in this study; and it seems likely that their 202 nm peak is actually the Uhrbach tail of the exciton absorption in KBr.

The V-centers in alkali halides have traditionally been produced in three ways: by additive coloration using Br_2 vapor, by X- or γ-irradiation, or by electrolytic injection. All three methods produce a complex set of bands from 300 nm to 200 nm with differing thermal stabilities. Ishii and Rolfe (1965) studied the bands produced by all three methods in pure KBr and in KBr doped with Ca^{2+}, Ba^{2+}, and Sr^{2+}. From an analysis of the dichroism associated with the various absorptions, they determined that the centers produced by these three methods of coloration were different in the pure crystals, but were similar in the alkaline-earth doped crystals. Ishii and Rolfe (1965) identified the trapped-hole centers in the alkaline-earth doped KBr as D centers, with room-temperature absorption bands between 260 nm and 290 nm. The center proposed by Ishii and Rolfe (1965) for the D-center was a Br_3^- ion surrounded by three divalent cations and three cation vacancies.

Jain et al. (1969) investigated the effects of X-irradiation on Pb^{2+} doped KBr. They found that the irradiation decreased and broadened the characteristic Pb^{2+} absorptions and that the presence of the lead inhibited the formation of F-centers. Jain et al. (1969) attributed these results to the capture of electrons by Pb^{2+} cations.

It is clear from these studies (and others) that V-centers are trapped-hole centers consisting of some type of bromine aggregate. Further, the presence of divalent cations can modify the observed V-bands, most likely by association of the divalent cation with the bromine aggregate. Finally, the trapped-hole centers are very sensitive to thermal treatment and can be bleached by annealing at temperatures above 400°C.

B. Experimental

The instrument used to measure the absorption was a Perkin Elmer model 450 spectrophotometer. A sample cell constructed by W. J. Fredericks allowed spectra to be observed at temperatures from -196°C to 150°C. The cell consisted of a liquid dewar with a copper thermal contact to an evacuated sample compartment. The sample was held in contact with the copper by another copper plate and four brass screws. A copper-constantan thermocouple was soldered to the copper near the sample.

Temperatures below room temperature were attained by using various cooling mixtures in the dewar (e.g., liquid N_2, ice-water, etc.). Temperatures above room temperature were attained with oil in the dewar, warmed by an immersion heater.

A Hanovia quartz mercury lamp was used to perform optical treatments on the samples. Additional optical treatments were performed with a xenon arc lamp.

The spectral data were entered into a PDP 11/23 microcomputer to allow background subtraction and peak deconvolution. The background consists of reflection and scattering losses from the crystal surfaces.

For perpendicular incidence, the reflection of light is given by

$$\rho_r = \left(\frac{n - 1}{n + 1} \right)^2 , \qquad (7.1)$$

where ρ_r is the fraction of the light reflected. The transmittance through a sample, T_r is then

$$T_r = \left[1 - \left(\frac{n - 1}{n + 1} \right)^2 \right]^2 , \qquad (7.2)$$

where reflection from both surfaces has been included. The wavelength dependence of the refractive index is given by the Sellmeier formula (Lowndes and Martin, 1969)

$$n^2 - 1 = \frac{\epsilon_o - \epsilon_\infty}{1 - \left(\frac{\lambda_o}{\lambda}\right)^2} + \frac{\epsilon_\infty - 1}{1 - \left(\frac{\lambda_e}{\lambda}\right)^2} \quad , \quad (7.3)$$

where ϵ_o and ϵ_∞ are the static and high-frequency dielectric constants of the material, and λ_o and λ_e are the characteristic absorption wavelengths associated with lattice vibration and electronic excitation, respectively. The second term in equation (7.3) is more accurately a sum of the many electronic excitations in a solid; however, Lowndes and Martin (1969) have fit experimental refractive indices in the alkali halides to better than 0.02% using the single term given in equation (7.3). The values obtained by Lowndes and Martin (1969) for λ_o, λ_e, ϵ_o, and ϵ_∞ in KBr were 87700 nm, 134.6 nm, 4.90, and 2.358, respectively.

The background corrections were performed on the spectra in this investigation in the following manner. The reflection loss was calculated at a wavelength removed from any dopant absorptions, using equations (7.2) and (7.3). The excess experimental transmission loss at this wavelength was then used as a scattering correction factor. The background correction was then extended through the dopant absorption region using this constant scattering factor and the wavelength-

dependent reflection loss calculated from equation (7.2) and (7.3). The scattering loss was generally only about 20% of the total background, so the assumption of wavelength independence for this term did not lead to a large error. In any case, most of the scattering is from macroscopic surface imperfections and is not expected to be very dependent on wavelength.

It should be mentioned that the term "transmission loss" has been used in the above discussion so as not to imply an energy absorption by the sample. However, it is only the absorbance, $^{-}\log T$, which can be treated as an additive quantity.

C. Oscillator Strength

In a classical theory of impurity absorption in solids, an oscillator strength, f, may be defined for an electronic absorption (Dexter, 1958)

$$Nf = 8.7 \times 10^{16} \frac{n}{(n^2 + 2)^2} \alpha_m \Delta\epsilon \quad , \qquad (7.4)$$

where N is the number density of the absorbing species, α_m is the absorption coefficient at the band maximum in cm^{-1}, and $\Delta\epsilon$ is the band width in eV at one-half the maximum absorbance. Equation (7.4) assumes a Gaussian band shape rather than the Lorentzian shape assumed in the original derivation of Smakula (1930).

Classically, an oscillator strength is simply the number of electrons which are responsible for a given absorption band. Quantum mechanically, the single absorption predicted by a classical oscillator is split into a number of bands corresponding to transitions to discrete electronic states (Smith and Dexter, 1972). For a single electron in a given state, the sum of the oscillator strengths for all transitions from that state is called the f-sum. Ignoring electronic interactions, the f-sum would be equal to one. But, the Pauli exclusion principle eliminates some classically allowed transitions; and the f-sum will, in general, deviate from its classical limit (Smith and Dexter, 1972).

. The oscillator strength is still a useful number for the comparison of band strengths. If the valence electronic state in an impurity atom is well separated from any filled electronic state, the f-sum will still be close to one (Smith and Dexter, 1972).

D. Results

Room temperature spectra of as-grown samples of pure KBr, KBr doped with Pb^{2+}, and KBr doped with Cd^{2+} are shown in Figures 7.1 through 7.3. The pure KBr spectrum is shown with and without background correction to demonstrate the accuracy of the correction procedure. The band edge for electronic absorption by the KBr host

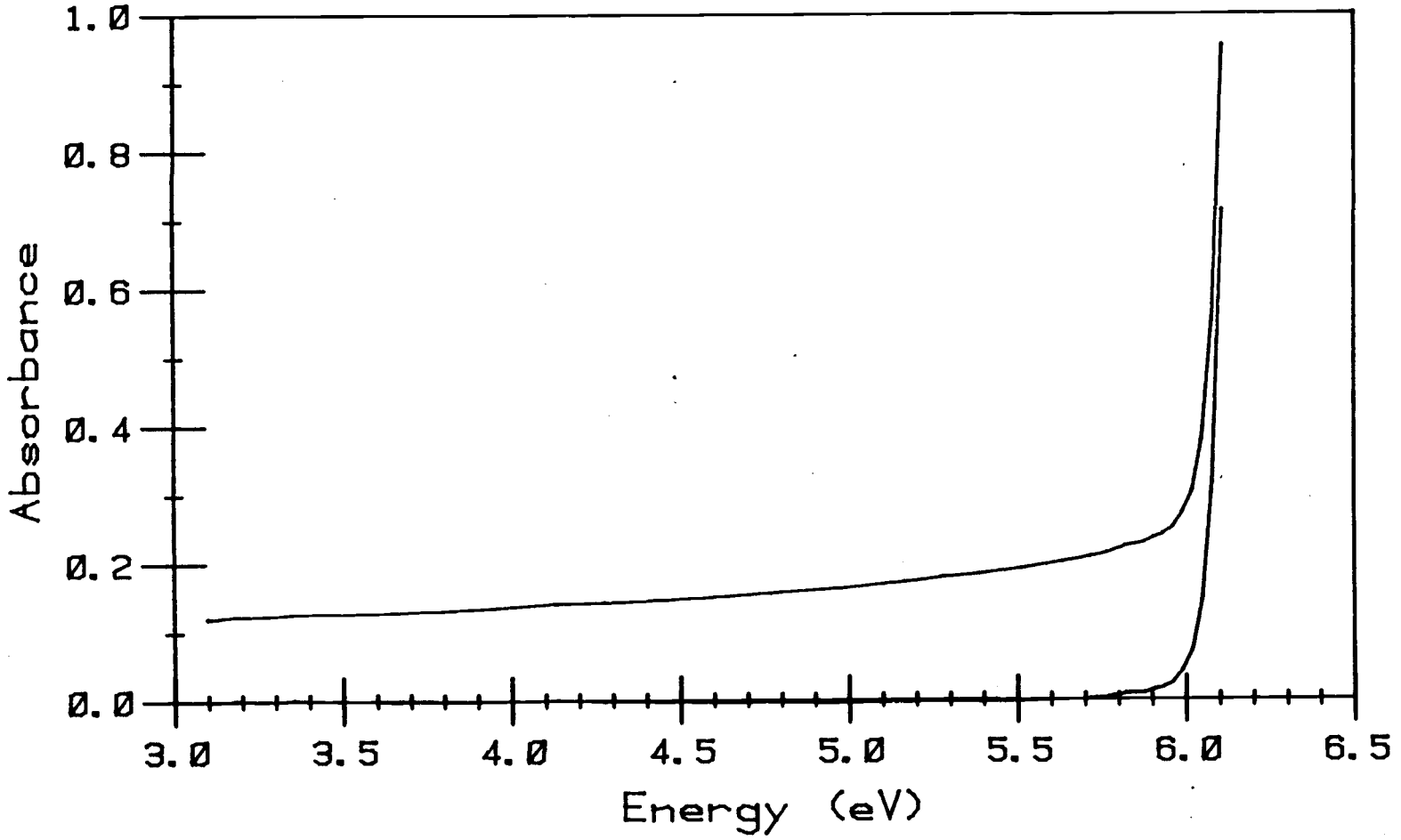

Figure 7.1 Absorption spectrum of pure KBr with and without background correction.

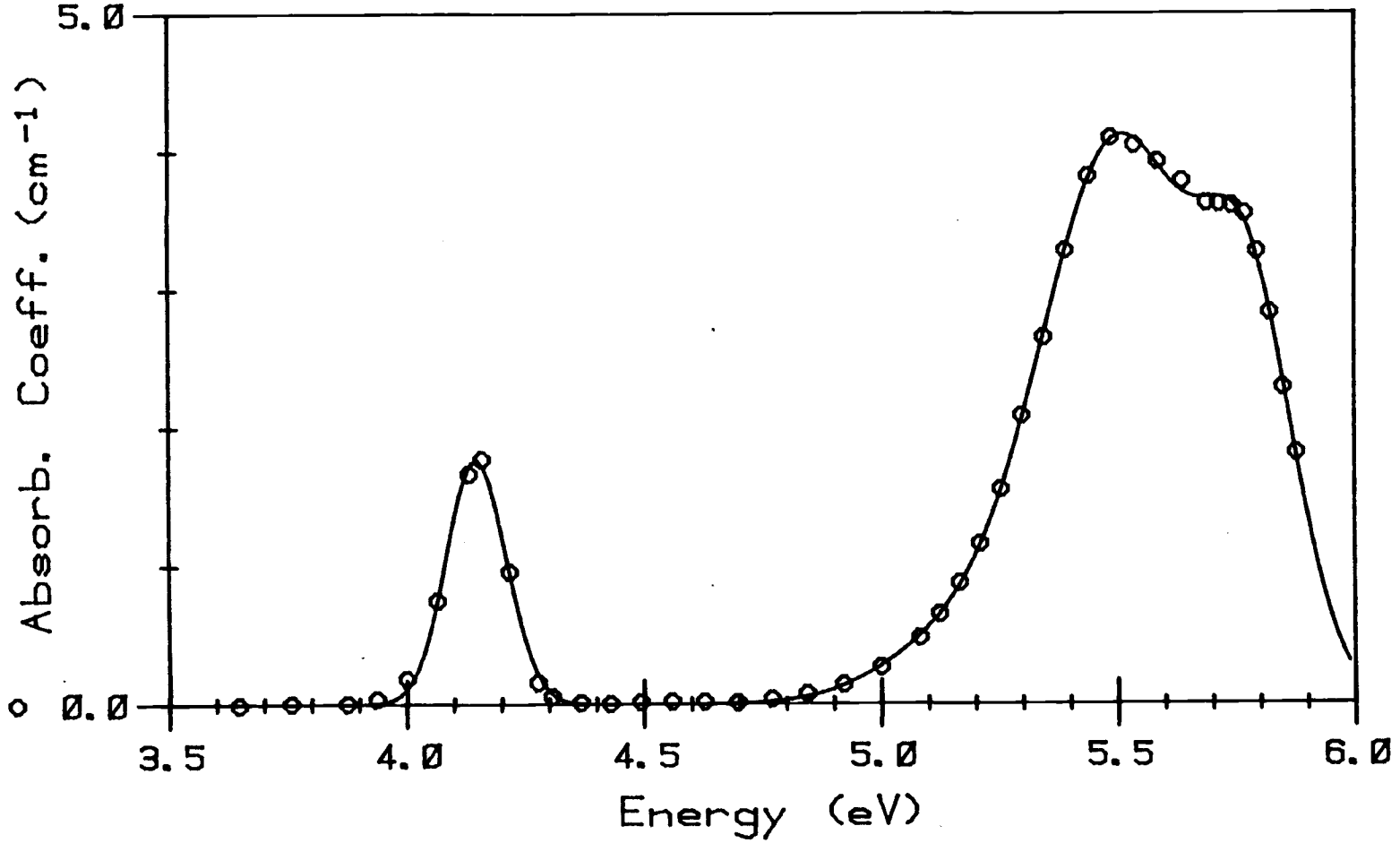

Figure 7.2 Absorption spectrum of Pb^{2+} doped KBr.

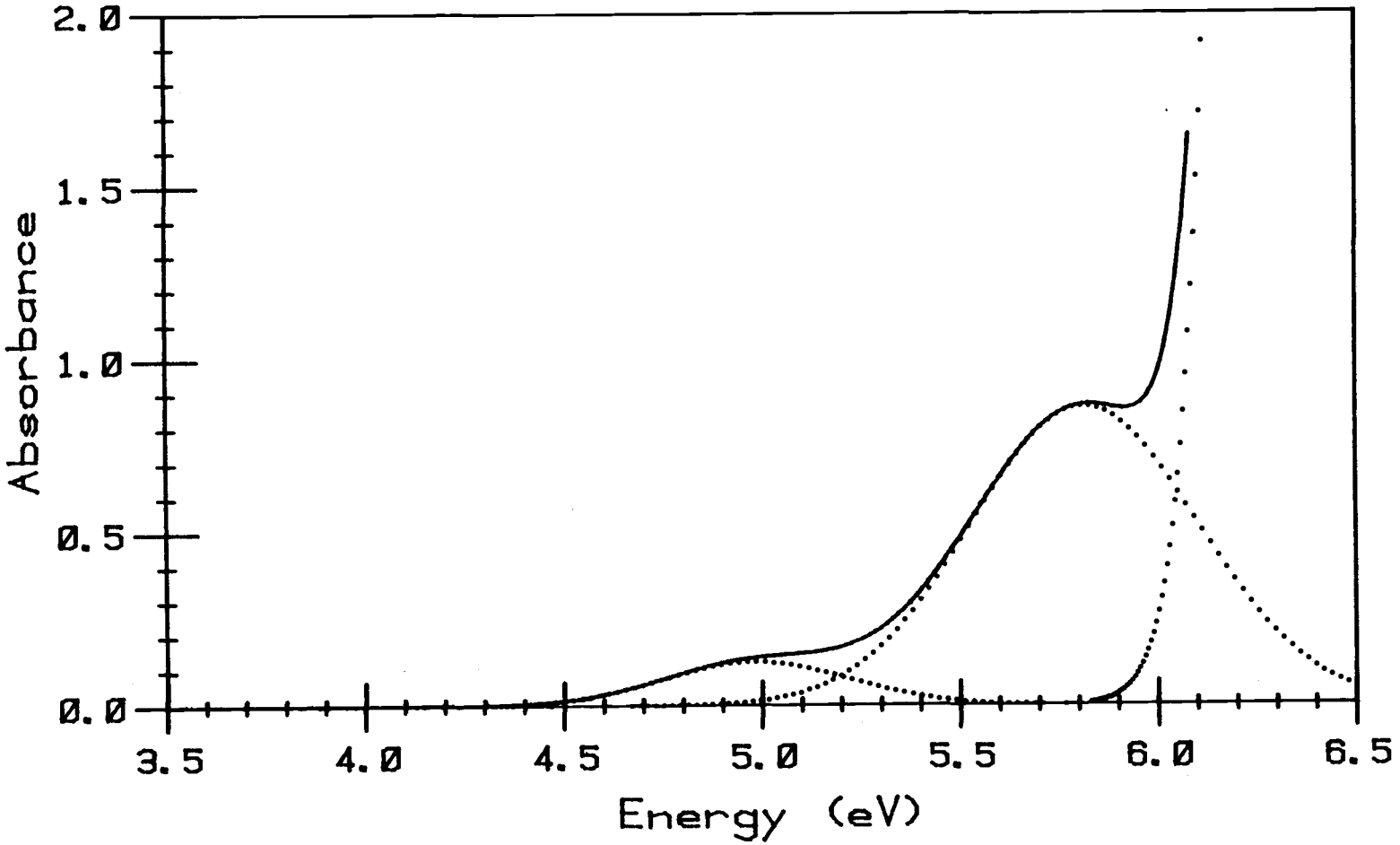

Figure 7.3 Absorption spectrum of Cd^{2+} doped KBr.

occurs at about 200 nm (6.2 eV) in these and following spectra.

The band assignments for the spectrum of Pb^{2+} doped KBr are given in Table 7.1. These assignments are based on the work by Chaney et al. (1973). Here the peak positions have been determined by deconvolution of the spectrum into Gaussian absorptions. The C-band was fitted with a single Gaussian, rather than the triplet used by Chaney et al. (1973); the marginally better fit attained using a triplet was not warranted by the data. The deconvoluted spectrum is shown in Figure 7.4.

The cadmium absorptions observed by Jain and Radhakrishna (1968) were also observed in this study, with the exception of their 202 nm peak. These peak positions are also given in Table 7.1.

Table 7.1 Absorption Peaks Observed in Pb^{2+} and Cd^{2+} Doped Samples at Room Temperature.

Pb^{2+} Doped KBr		Cd^{2+} Doped KBr
Band Max (eV)	Designation*	Band Max (eV)
4.15 ± .05	A-Band	5.0 ± 0.1
5.1 ± 0.1	B-Band	5.8 ± 0.1
5.52 ± .07	C-Band	
5.79 ± .05	D'-Band	

*Designations are from Chaney et al. (1973).

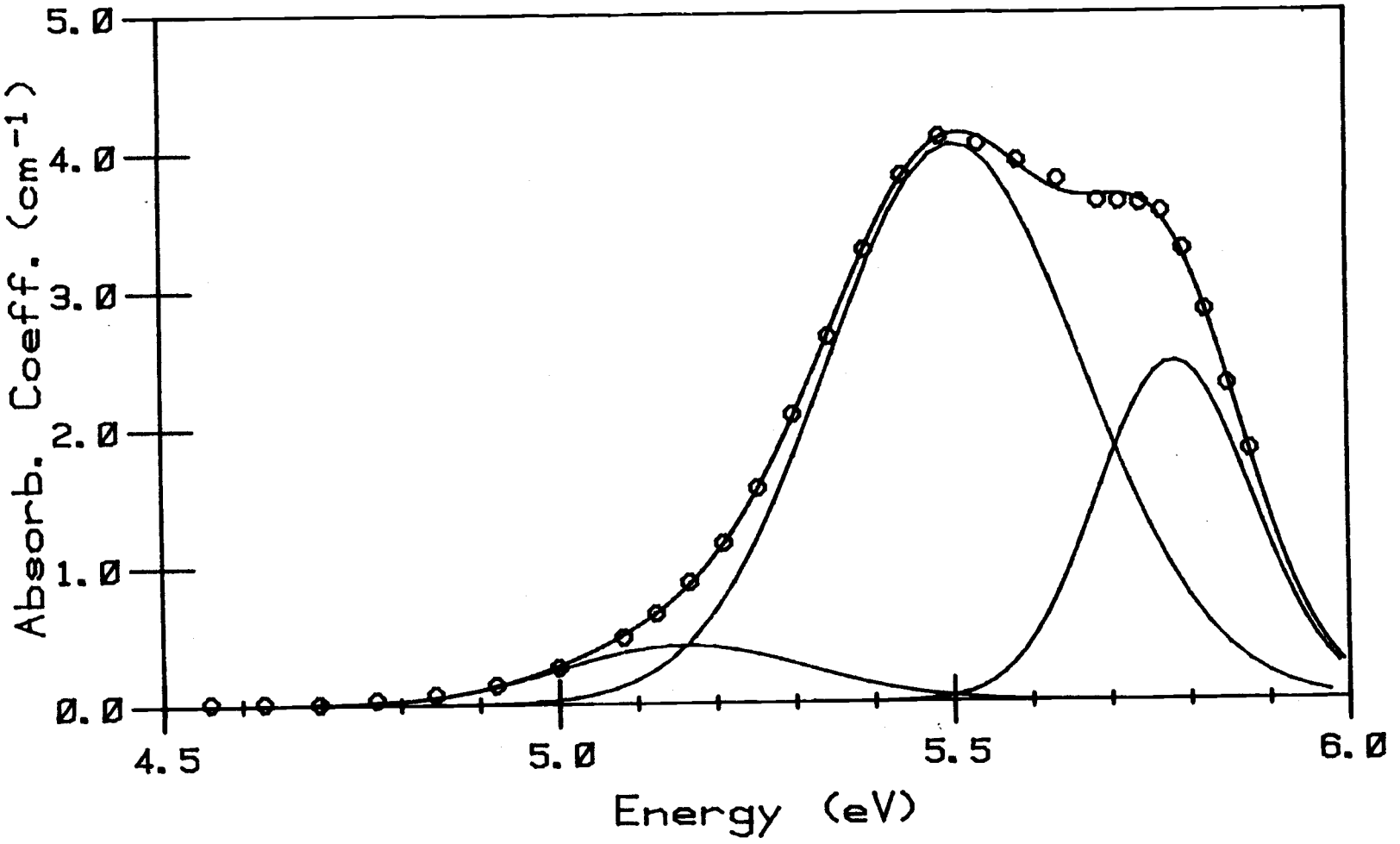

Figure 7.4 Deconvolution of B, C, and D^1 absorption bands in Pb^{2+} doped KBr.

Table 7.2 A-, B-, and C-band Parameters at Various Pb^{2+} Concentrations.

Conc. (10^{16} cm^{-3})	A-Band		B-Band		C-Band	
	$\alpha_m(cm^{-1})$	$\Delta\in$(eV)	$\alpha_m(cm^{-1})$	$\Delta\in$(eV)	$\alpha_m(cm^{-1})$	$\Delta\in$(eV)
22.1	26.6	0.151	----	----	----	----
21.2	25.6	0.150	----	----	----	----
16.3	19.1	0.152	2.5	0.36	44.6	0.43
11.9	14.6	0.148	0.77	0.64	33.5	0.49
6.9	8.7	0.146	1.4	0.49	19.6	0.42
6.4	8.0	0.148	1.1	0.31	18.4	0.42
2.6	1.8	0.147	0.42	0.37	4.0	0.38

The Ca^{2+} doped samples showed no observable absorptions in the visible or untraviolet regions of the spectrum.

Oscillator strengths for the A-, B-, and C-bands in the lead doped samples were determined using a number of as-grown samples with varying Pb^{2+} concentrations. Values of α_m, $\Delta\epsilon$, and N for these samples are listed in Table 7.2. Plots of (α_m x $\Delta\epsilon$) versus N are shown in Figure 7.5 for the three bands. Using the slope of these plots and equation (7.4), values for the oscillator strengths were determined. The value of the refractive index in equation (7.4) was determined using equation (7.3) and the wavelength of the band maximum. The oscillator strengths and refractive indices for each band are listed in Table 7.3.

Table 7.3 Oscillator Strengths for the A-, B-, and C-bands in Pb^{2+} Doped KBr.

Band	n (at band max.)	f
A	1.644	0.12 ± .01
B	1.720	0.04 ± .01
C	1.766	0.77 ± .02
f-sum		0.93 ± .05

No oscillator strength values for these absorptions were found in the literature. Sibley et al. (1964)

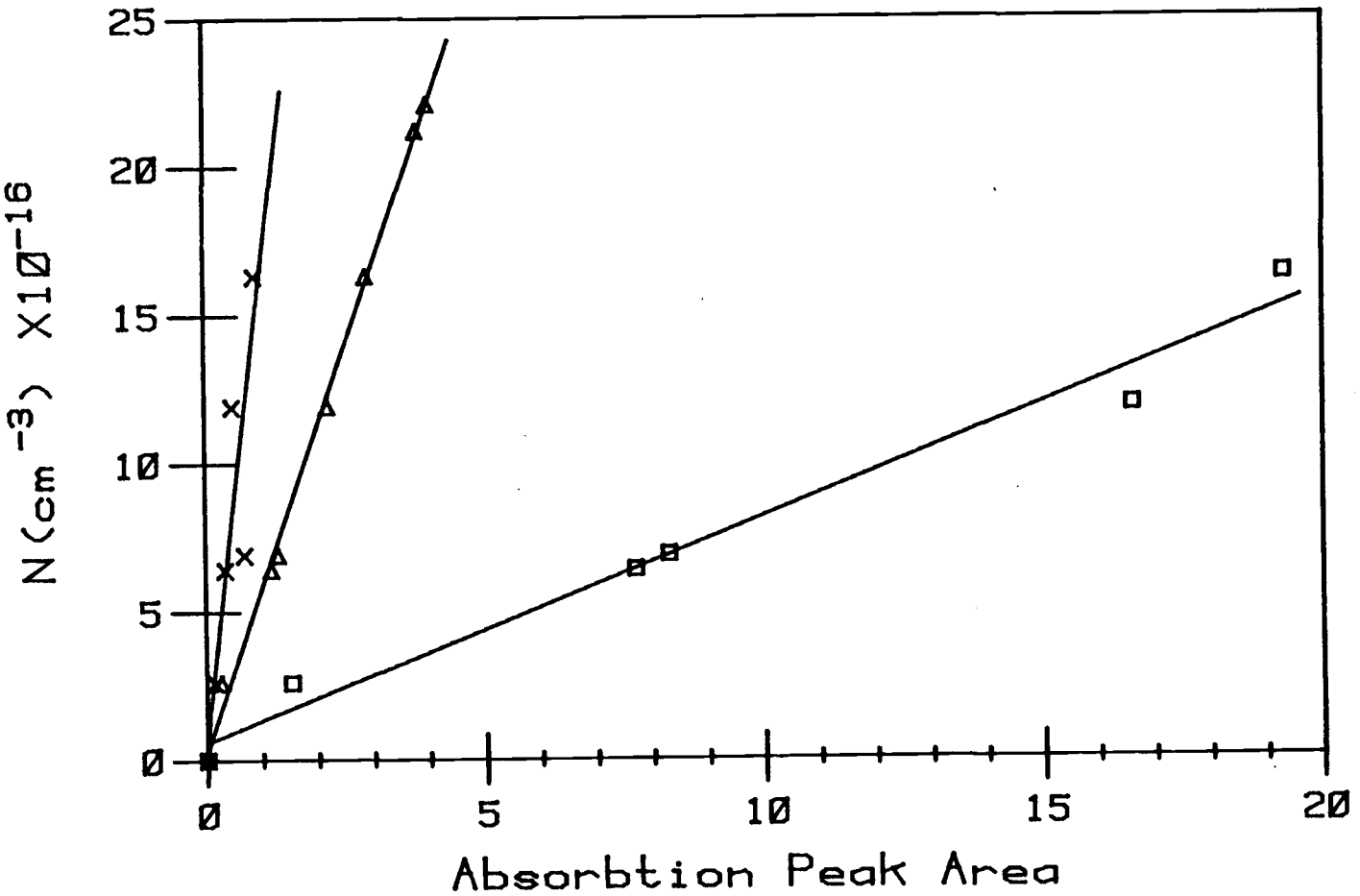

Figure 7.5 Plots of α_m x $\Delta\epsilon$ versus lead concentration for the A, B, and C absorption bands (Δ, x, and □ respectively).

calculated a value of 0.11 for the oscillator strength of the A-band absorption in KCl.

Irradiation of the Pb^{2+} doped samples with ultraviolet light from the quartz mercury lamp created a new band at about 4.5 eV, and the characteristic Pb^{2+} absorption bands were reduced in intensity. These effects are demonstrated by the spectra shown in Figure 7.6. This new band will be designated the D_x-band. The D_x-band could be bleached by warming the sample to about 400°C for 15 minutes. A number of experiments were performed to determine the thermal and optical requirements for producing the D_x-band, and to estimate the activation energy for the thermal bleaching process. The results of these experiments are given in Table 7.4.

Irradiation of the Ca^{2+} doped samples produced two very weak and very broad absorptions at about 2 eV and about 4.8 eV.

Irradiation of the Cd^{2+} doped samples produced a very weak and broad absorption at about 4.8 eV, and the characteristic Cd^{2+} absorptions were slightly reduced.

E. Discussion

The oscillator strengths of the A-, B-, and C-bands in the Pb^{2+} doped samples yield an f-sum of 0.93.

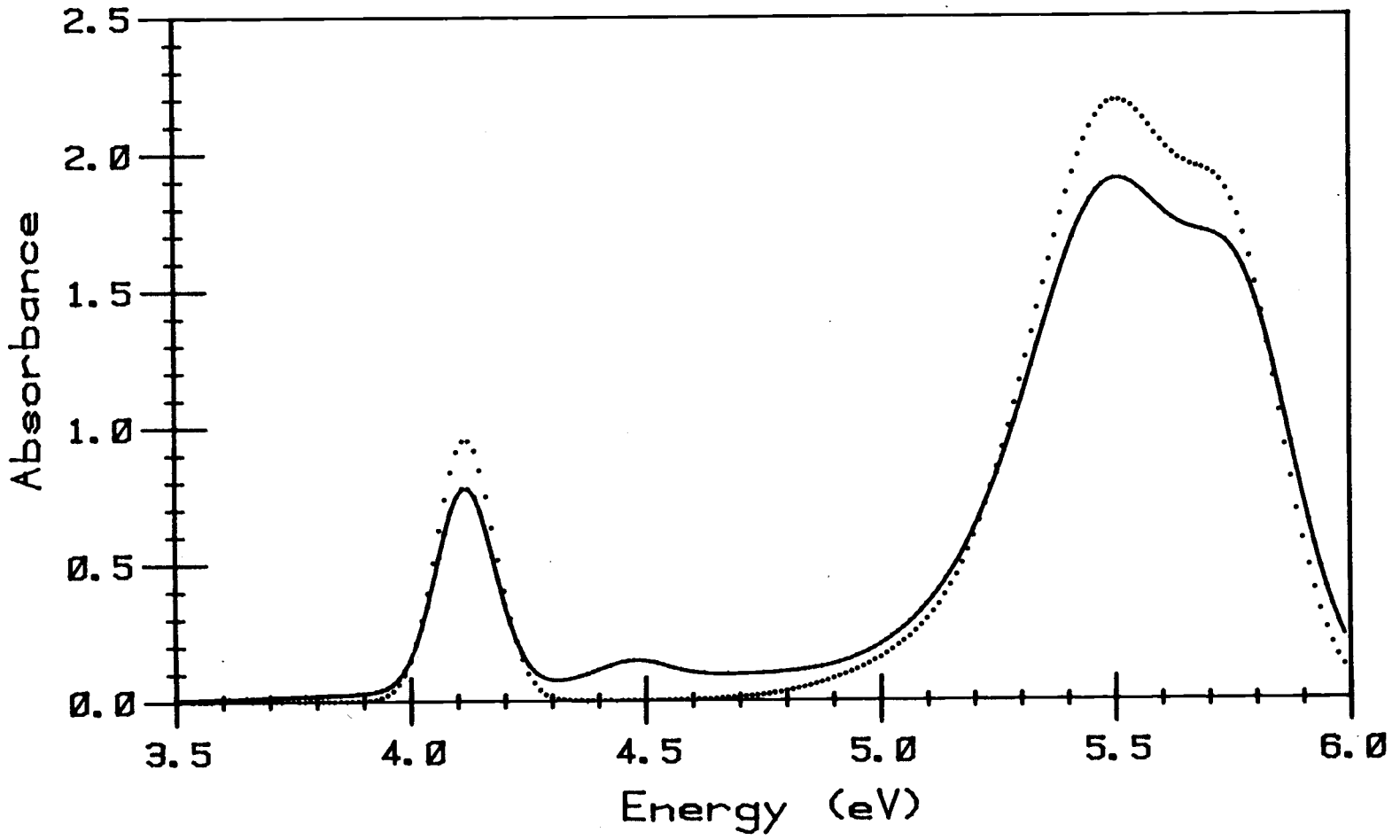

Figure 7.6 Absorption spectrum of Pb^{2+} doped KBr before (dotted curve) and after (solid curve) irradiation.

Table 7.4 Summary of Experiment on the Production and Thermal Bleaching of the D_x-band in Pb^{2+} Doped KBr.

A. Temperature Dependence of D_x-band Production

Irradiation Temp.	Result
23°C	D_x-band easily produced with 10-15 min. of irradiation
-77°C	D_x-band produced but at a marginally reduced rate
-296°C	No D_x-band produced even at long irradiation times.

B. Irradiation Wavelength Dependence of D_x-band Production

Transmitted wavelengths through optical filter	Result
>350 nm	No D_x-band produced
>210 nm	No D_x-band produced

C. Thermal Bleaching of D_x-band*

Temperature	Result
23°C	Slow bleaching measurable over days
100°C	Moderately fast bleaching measurable over hours
150°C	Fairly rapid bleaching measurable over minutes

*The activation energy for the bleaching process was estimated to be ~0.6 ± 0.3 eV from these results.

Despite the theoretical limitations of an f-sum, the fact that the f-sum for these absorptions is near one lends evidence for the correctness of the band designations given by Chaney et al. (1973). All three absorptions are presumed to occur due to transitions from the same ^1S_o ground electronic state. Since the f-sum for these transitions is nearly one, they form a nearly complete set of possible transitions as predicted.

The converse of the above argument lends evidence that there is not a great deal of electron-electron interaction between the ^1S_o Pb^{2+} electrons and the KBr host electrons. Since the oscillator-strength sum is nearly one, the electronic excited states must be well separated from the filled host electronic levels. Of course, electron-electron interaction effects can produce "canceling" positive and negative corrections to the f-sum, so this conclusion is not definitive.

The effects of ultraviolet irradiation on the KBr samples in this study are consistent with a low-efficiency coloration process yielding trapped-hole and trapped-electron centers. Smakula (1930) observed the formation of F-centers in KBr upon similar irradiation with a mercury lamp. The ultraviolet coloration process has been studied more recently by Etzel (1955), Parker (1961), and Rolfe (1959).

From Table 7.4 (B), the D_x band is produced by

irradiation at wavelengths less than 210 nm; this is consistent with Smakula's (1930) findings for F-center production. Rolfe (1959) showed that F-centers could not be produced in very pure cyrstals by ultraviolet irradiation; this was also found to be true in the present investigation.

The D_x band produced in the Pb^{2+} doped samples is then presumably a trapped-hole center similar to the D centers observed by Ishii and Rolfe (1965) in alkaline-earth doped KBr; the weak bands at 2 eV and 4.8 eV observed in irradiated Ca^{2+} doped samples are typical F and D_2 absorptions; and the 4.8 eV band observed in irradiated Cd^{2+} doped samples is a trapped-hole center similar to the D_x band.

These presumptions are consistent with generally accepted properties of the coloration process: alkaline-earth dopants enhance F-center production, while cadmium and lead dopants retard F-center production but enhance the production of trapped holes.

Since no F band is produced in Pb^{2+} and Cd^{2+} doped samples, the question arises as to where the electron goes in forming the trapped-hole centers. The D_x band is formed in the Pb^{2+} doped samples, even at moderately reduced temperatures (-77°C). This precludes any ionic motion to form complex centers. Further, since the characteristic Pb^{2+} (and Cd^{2+}) absorptions are reduced

upon irradiation, the missing electron quite possibly reduces the divalent cations to a +1 state. The higher 2nd ionization potential for lead and cadmium, compared to calcium, then also explains the differing effects of these dopants on the coloration process.

Lidiard (1956) has calculated the energy required for reduction of Cd^{2+} and Ca^{2+} in KCl from lattice and ionization energies, yielding 5.9 eV for Cd^{2+} and 10.8 eV for Ca^{2+}. Assuming similar values for these values in KBr, the energy of the irradiation would be sufficient to reduce the Cd^{2+} but not to reduce the Ca^{2+}. A similar energy would be expected for the reduction of Pb^{2+} since lead and cadmium have similar 2nd ionization potentials.

VIII. CONCLUSION

The investigation of the properties of alkali halide crystals is such a mature field that a single study cannot hope to answer every question. However, some salient points have been brought out in this thesis.

The distribution coefficients estimated here for Ca^{2+}, Cd^{2+}, and Pb^{2+} in KBr have not been previously reported. The surprising lack of this information in the literature warrants more precise future determinations. As mentioned previously, the values reported in this thesis can only be considered as lower limits.

In the best pure crystals studied here, the extrinsic scattering was only of equal magnitude to the intrinsic thermal MB scattering. Further, a sizable amount of the extrinsic scattering can be attributed to inherent thermal vacancies. Thus, the current best crystals are approaching the limit for scattering losses. In some of the pure crystals, the extrinsic scattering was fairly large; the thermal history of the crystal seems to be an important factor in these cases.

The scattering measurements on doped samples clearly showed the marked precipitation of dopants which occurs from a slow annealing process. Solubilities for

Ca^{2+}, Cd^{2+}, and Pb^{2+} were determined for a temperature near room temperature. As pointed out by Chapman and Lilley (1973), solubilities of divalent cations in alkali halides are a combination of a free ion solubility, a divalent cation-vacancy pair solubility, and other higher-order complex solubilities. Thus, many of the reported enthalpies and entropies of solution are only valid over narrow temperature ranges. An investigation of solubility over a wide temperature range using light-scattering techniques would be a useful addition to the literature.

The very small cadmium solubility determined in this study is difficult to explain; Cd^{2+} is in most respects similar to Ca^{2+}. Ikeya (1974) showed that the distribution coefficient for transition metal ions in KCl is an inverse function of the number of d electrons. Ikeya attributed this to the greater stability of the higher-d metal halides. A similar explanation for the low Cd^{2+} solubility in KBr seems plausible.

The coloration of the crystals using ultraviolet light closely resembled the effects caused by higher-energy X- and γ-ray irradiations performed by numerous investigators. The use of this low-yield technique for defect production is useful in that small defect concentrations can be produced with most of the pre-irradiation

dopant-defect structures intact.

BIBLIOGRAPHY

American Institute of Physics Handbook (1963). 2nd Edition. (D. E. Gray, ed.), McGraw-Hill, New York.

Arora, A. K., Kesavamoorthy, R., and Sahoo, D. (1982). J. Phys. C. - Solid State. Vol. 15:4591.

Asano, S. and Sato, M. (1980). Appl. Opt. Vol. 19: 962.

Ayres, W. A., Small, E. W., and Isenberg, I. (1974). Anal. Biochem. Vol. 58:361.

Bansiger, K. G. and Schneider, E. E. (1962). J. Appl. Phys. Vol. 33, Supp. no. 1:383.

Benedek, G. B. and Fritsch, K. (1966). Phys. Rev. Vol. 149:647.

Bertoldi, P. G., Capelletti, R., Fermi, F., Manfredi, M., and Graveris, V. J. (1980). J. de Phys. (Paris). Vol. 41, Supp. no. 7:C6-367.

Braul, H. and Plint, C. A. (1981). Solid State Comm., Vol. 38:227.

Brillouin, L. (1922). Ann. der Phys. Vol. 17:88 (cited in Fabelinski, I. L. Molecular Scattering of Light, Plenum, New York, 1968).

Cummins, H. Z. (1969). "Laser Light Scattering Spectroscopy," in International School of Physics "Enrico Fermi" XLII Course, Varenna, 1967 (R. Glauber, ed.), Academic Press, New York.

Cummins, H. A. and Schoen, P. E. (1972). In Laser Handbook (F. T. Arecchi and E. O. Schultz-Dubois, eds.), North-Holland, Amsterdam.

Chandra, S. and Rolfe, J. (1971). Can. J. Phys. Vol. 49:2098.

Chaney, R. E., Jacobs, P. W. M., and Tsuboi, T. (1973). Can. J. Phys. Vol. 51:2242.

Chapman, J. A., and Lilley, E. (1973). J. de Phys. (Paris). Vol. 34, Supp. 11-12:C9-455.

Dexter, D. L. (1958). "Theory of the Optical Properties of Imperfections in Non-metals," in Solid State Physics Vol. 6 (F. Seitz and D. Turnbull, Eds.), Academic Press, New York, 1958.

Eshelby, J. D., Newey, C. W. A., Pratt, P. L., and Lidiard, A. B. (1958). Phil. Mag. Vol. 3:75.

Etzel, H. W. (1955). Phys. Rev. Vol. 100:1643.

Fabelinski, I. L. (1968). Molecular Scattering of Light, Plenum, New York.

Fabelinski, I. L. (1956). Sov. Phys. Doklady Vol. 1: 115 (cited in Fabelinski, I. L. Molecular Scattering of Light, Plenum, New York, 1968).

Fabelinski, I. L. and Chistyi. (1976). Sov. Phys. Usp. Vol. 19:597 (A.I.P. Translation).

Fowler, W. B. (1968). "Electronic States and Optical Transitions of Color Centers," in Physics of Color Centers (W. B. Fowler, ed.), Academic Press, New York, 1968.

Fredericks, W. J. (1977). "Purification of Potassium Bromide and Alkaline Earth Fluorides for Laser Components," in Laser Induced Damage in Optical Materials: 1977, (A. J. Glass and A. H. Guenther, eds.), NBS Special Publication 509.

Fredericks, W. J., Collins, P. R., and Edwards, D. F. (1983). J. Phys. Chem. Solids (in press).

Fukuda, A. (1964). Sci. Light. Vol. 13:64.

Gross, E. (1930). Nature. Vol. 126:201 (cited in: A. T. Young, Phys. Today, Vol. 31:42, 1982).

Handbook of Chemistry and Physics. (1976). 57th Edition. (R. C. Weast, ed.), C.R.C. Press, Cleveland.

Havinga, E. E. and Bosman, A. J. (1965). Phys. Rev. Vol. 140:A292.

Hughes, A. E. (1982). "Formation of Clusters in Bulk Materials," Lectures presented at the NATO Advanced Study Institute on "The Impact of Cluster Physics in Materials Science and Technology," Cap d'Agde, 1982 (to be published with NATO ASI Series Books, 1983).

Humphreys-Owen, S.P.F. (1954). Proc. Phys. Soc. Vol. B68:325.

Ikeya, M. (1974). J. Crys. Growth. Vol. 24/25:468.

Ishii, T. and Rolfe, J. (1966). Phys. Rev. Vol. 141: 758.

Jain, S. C. and Radhakrishna, S. (1968). Phys. Rev. Vol. 172:972.

Jain, S. C., Radhakrishna, S., and Sai, K. S. K. (1969). J. Phys. Soc. Japan. Vol. 27:1179.

Jain, S. C. and Hughes, A. E. (1976). J. de Phys. (Paris). Vol. 37, Supp. 12:67-463.

Jain, V. K. (1971). Phys. Stat. Sol. (B). Vol. 44:11.

JANAF Thermochemical Tables (1971). 2nd Edition. (D. R. Stull and H. Prophet, eds.), NSRDS-NBS37.

Kaplan, H., Shaham, J., and Low, W. (1970). Phys. Lett. Vol. 31A:201.

Kerker, M. (1969). The Scattering of Light and Other Electromagnetic Radiation, Academic Press, New York.

Kirk, D. L., Kahn, A. R., and Pratt, P. L. (1975). J. Phys. D. - Appl. Phys. Vol. 8:2013.

Krishnan, R. S. (1938). Proc. Ind. Acad. Sci. Vol. fA:91 (cited in: F. Perrin, J. Chem. Phys. Vol. 10: 415, 1942).

Landau, L. D. and Placzek, G. (1934). Zhurn. Phys. Sowjetunion. Vol. 5:172 (cited in Fabelinski, I. L. Molecular Scattering of Light, Plenum, New York, 1968).

Landolt-Bornstein (1966). Numerical Data and Functional Relationships in Science and Technology, New Series, Group III, Vol. 1 (K. H. Hellwege, ed.), Springer-Verlag, Berlin.

Landolt-Bornstein (1973). Numerical Data and Functional Relationships in Science and Technology, New Series, Group III, Vol. 7a (K. H. Hellwege, ed.), Springer-Verlag, Berlin.

Landolt-Bornstein (1979). Numerical Data and Functional Relationships in Science and Technology, New Series, Group III, Vol. 2 (K. H. Hellwege, ed.), Springer-Verlag, Berlin.

Lidiard, A. B. (1956). "Ionic Conductivity," in Handbuch der Physik, Vol. 20 (S. Flugge, ed.), Springer-Verlag, Berlin.

Lidiard, A. B. (1973). J. de Phys. (Paris). Vol. 34, Supp. 11-12:C9-1.

Lifshitz, I. M. and Geguzin, Y. E. Fiz. Tverd. Tela. Vol. 7:62 (cited in: R. W. Whitworth, J. de Phys. (Paris). Vol. 34, Supp. 11-12:C9-455).

Lowndes, R. P. and Martin, D. H. (1969). Proc. Royal Soc. A, Vol. 308:473.

Mandel'shtam, L. I. (1926). Zh. Russ. Fiz. Khim. Vol. 58:381 (cited in Fabelinski, I. L. Molecular Scattering of Light, Plenum, New York, 1968).

Marcoux, J. (1971). Rev. Sci. Ins. Vol. 42:600.

Matsumoto, H., Nakagawa, H., and Kuwabara, H. (1978). J. Phys. Soc. Japan. Vol. 44:957.

Matsura, H. and Miyazawa, T. (1973). Bull. Chem. Soc. Japan. Vol. 46:3031.

Mie, G. (1908). Ann. Physik. Vol. 25:377.

Mills, D. L. (1980). J. Appl. Phys. Vol. 51:5865.

Nye, J. F. (1964). Physical Properties of Crystals, Oxford University Press, London.

Pangonis, W. J., Heller, W., and Economou, N. A. (1960). J. Chem. Phys. Vol. 34:960.

Parker, J. H. (1961). Phys. Rev. Vol. 124:703.

Pauling, L. (1960). The Nature of the Chemical Bond and the Structure of Molecules and Crystals, Third Edition, Cornell University Press, Ithaca, New York.

Perrin, F. (1942). J. Chem. Phys. Vol. 10:415.

Plint, C. A. and Sibley, W. A. (1965). J. Chem. Phys. Vol. 42:1378.

Radhakrishna, S. and Chowdari, B. V. R. (1977). Fort. der Physik. Vol. 25:511.

Raman, C. V. (1928) (cited in Fabelinski, I. L. Molecular Scattering of Light, Plenum, New York, 1968).

Rank, D. H., Skorinko, G., Eastman, D. P., Saksena, G. D., McCubbin, T. K., and Wiggins, T. A. (1960). J. Opt. Soc. Am. Vol. 50:1045.

Lord Rayleigh. (1871). Phil. Mag. Vol. 41:107, 274, 447.

Rolfe, J. (1959). In International Symposium on Color Centers in Alkali Halides, Oregon State College, Corvallis, Oregon.

Sibley, W. A., Sonder, E., and Butler, C. T. (1964). Phys. Rev. Vol. 136:A537.

Smakula, A. (1930). Z. Physik. Vol. 59:603.

Smakula, A. (1930). Z. Physik. Vol. 63:762.

Smith, D. Y. and Dexter, D. L. (1972). "Optical Absorption Strengths of Defects in Insulators," in Progress in Optics, Vol. X. (E. Wolf, ed.), North-Holland, Amsterdam.

Suzuki, K. (1961). J. Phys. Soc. Japan. Vol. 16:67.

Tessman, J., Kahn, A., and Shockley, W. (1953). Phys. Rev. Vol. 92:890.

Theimer, O. and Plint, C. A. (1958). Annals Phys. Vol. 3:408.

Theimer, O., Plint, C. A., and Sibley, W. A. (1960). Annals Phys. Vol. 9:475.

Tsuboi, T., Oyama, K., and Jacobs, P. W. M. (1975). Can. J. Phys. Vol. 53:192.

Vacher, R. and Boyer, L. (1972). Phys. Rev. (B). Vol. 6:639.

Van de Hulst, H. C. (1957). Light Scattering by Small Particles, John Wiley and Sons, New York.

Whitworth, R. W. (1973). J. de Phys. (Paris). Vol. 34, Supp. 11-12:C9243.

Wehner, R. K. and Klein, R. (1972). Physica. Vol. 62:161.

Wyckoff, R. W. G. (1963). Crystal Structures Vol. 1. 2nd Edition, John Wiley and Sons, New York.

Young, A. T. (1982). Phys. Today. Vol. 31:42.

APPENDICES

APPENDIX I

CADMIUM DOPED CRYSTALS

CRYSTAL NUMBER 316-81

POSITION (cm)	CONCEN. (mppm)
1.30	1.00
2.90	1.19
4.40	2.39
5.00	1.67
5.90	2.28
6.50	3.18
7.40	5.00
8.40	5.90

CRYSTAL NUMBER 365-81

POSITION (cm)	CONCEN. (mppm)
0.80	0.79
2.10	0.88
5.40	2.01
6.10	3.16
7.00	7.44

CALCIUM DOPED CRYSTALS

CRYSTAL NUMBER 34-82

POSITION (cm)	CONCEN. (mppm)
0.20	223.
0.80	243.
0.85	285.
1.00	302.
1.90	395.
2.55	356.
4.00	543.
4.70	647.

CRYSTAL NUMBER 37-82

POSITION (cm)	CONCEN. (mppm)
0.60	135.
1.90	160.
2.10	157.
3.40	193.

LEAD DOPED CRYSTALS

CRYSTAL NUMBER 228-81

POSITION (cm)	CONCEN. (mppm)
0.20	95.
0.85	102.
1.20	109.
2.50	123.
2.70	122.
3.35	140.
5.70	249.
6.35	268.
7.25	385.

CRYSTAL NUMBER 127-82

POSITION (cm)	CONCEN. (mppm)
0.40	52.
1.90	65.
2.10	71.
3.50	84.
3.70	77.
5.20	105.
5.40	110.
6.85	146.

CADMIUM DOPED CRYSTALS

CRYSTAL NUMBER 116-82

POSITION (cm)	CONCEN. (mppm)
1.05	2.77
2.35	3.38
2.65	3.62
3.95	4.35
4.25	4.72
5.55	6.63
5.85	7.53
7.10	20.10

CRYSTAL NUMBER 123-82

POSITION (cm)	CONCEN. (mppm)
1.00	5.39
2.30	6.12
2.50	5.97
3.70	7.63
5.20	10.90
5.40	11.50
6.70	17.50
7.00	19.70

APPENDIX II

The FSR of the MB instrument was measured from a spectrum of the high resolution atomic line structure of a mercury lamp. The observed peak positions are listed in the Table below in units of channel numbers. The channel shifts are given in column two relative to the peaks at 76, 451, and 821 channels. The wavelength shift, $\Delta\lambda$, corresponding to these channel shifts is given in columns three and four from two literature sources.

Plots of $\Delta\lambda$ versus channel shift for both sets of literature values are shown in Figure AII.1. The slope of these plots yields

$$\text{(A.I.P.):} \qquad 1.31 \times 10^{-3} \pm 0.01 \times 10^{-3} \text{ Å/channel} \tag{AII.1}$$

$$\text{(Rank et al.):} \quad 1.32 \times 10^{-3} \pm 0.01 \times 10^{-3} \text{ Å/channel.} \tag{AII.2}$$

The FSR, in channels, was obtained by averaging the shift for one spectral order of each peak. The average value was

$$\text{FSR} = 371.9 \pm 2.2 \text{ channels} \tag{AII.3}$$

Table AII.1 Spectral Lines of Mercury Lamp.

Peak (channels)	Δ channels	Δλ (Å) (1)	Δλ (Å) (2)
76	0	0	0
145	69	0.09393	0.09497
193	117	0.1521	0.1537
217	141	0.1849	0.1863
323	247	0.3184	0.3209
417	0	0	0
451	34	0.0457	0.0441
519	102	0.1396	0.1391
565	148	0.1978	0.1978
591	174	0.2306	0.2304
692	275	0.3641	0.3605
788	0	0	0
821	33	0.0457	0.0441
889	101	0.1396	0.1391

(1) A.I.P. Handbook (1963).

(2) Rank et al. (1960).

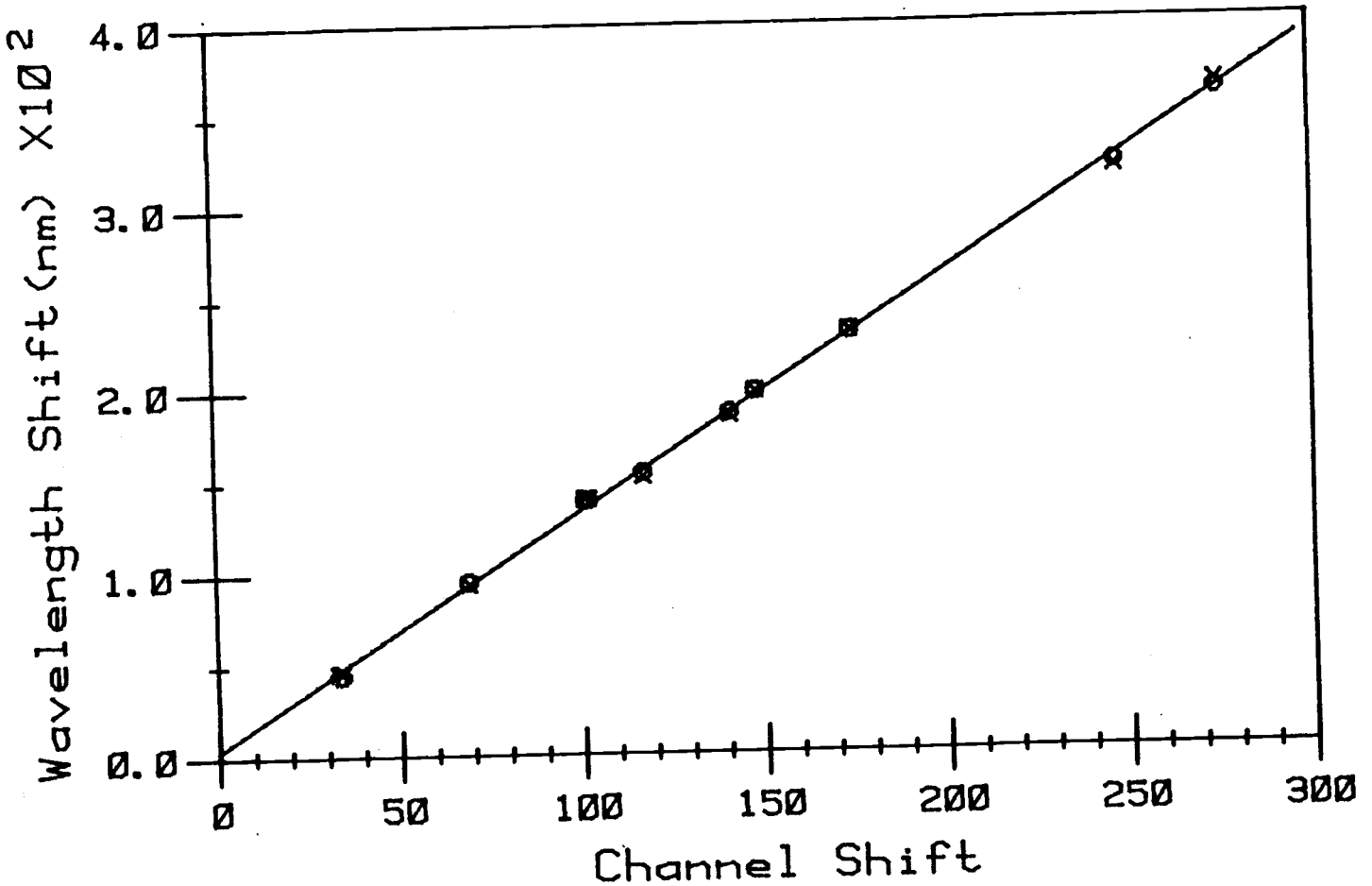

Figure AII.1 Channel shift versus wavelength shift of Hg atomic lines. Wavelength shifts are from A.I.P. Handbook (X's) and Rank et al. (1960) (O's).

Using the average of equations (AII.1) and (AII.2) and combining with equation (AII.3) yields

$$FSR = 0.488 \pm 0.004\text{Å} \text{ @ } 5461\text{Å} \qquad \text{(AII.4)}$$

The FSR of an interferometer changes with the wavelength of the incident radiation according to (Fabelinski and Chistyi, 1976)

$$FSR_{\lambda_2} = FSR_{\lambda_1} \left(\frac{\lambda_2}{\lambda_1} \right)^2 \quad . \qquad \text{(AII.5)}$$

Thus from equations (AII.4) and (AII.5), the FSR at 4880Å is

$$FSR = 0.390 \pm 0.004\text{Å} \text{ @ } 4880\text{Å} \quad . \qquad \text{(AII.6)}$$

APPENDIX III

Crystal	$\Delta\lambda_L$ (Å)	$\Delta\lambda_{T_2}$ (Å)
408	0.111 ± 0.001	———
413	0.111 ± 0.001	———
451	0.111 ± 0.001	———
751	0.111 ± 0.001	0.0491 ± 0.0005
834	0.111 ± 0.001	0.0500 ± 0.0005
751	0.111 ± 0.001	———
232-79	0.111 ± 0.001	———
235-79	0.111 ± 0.001	———

APPENDIX IV

ANNEALED CALCIUM DOPED SAMPLES

Scattering data from MB spectrometer

Conc.(mppm)	Scat Ratio	Error in S.R.
579.0	0.356E+05	0.400E+04
543.0	0.360E+05	0.400E+04
514.0	0.291E+05	0.400E+04
416.0	0.131E+05	0.370E+04
395.0	0.860E+04	0.370E+04
374.0	0.580E+04	0.370E+04
312.0	0.245E+04	0.900E+03
300.0	0.260E+04	0.900E+03
288.0	0.410E+04	0.900E+03
255.0	0.420E+04	0.140E+04
249.0	0.180E+04	0.140E+04
243.0	0.170E+04	0.140E+04

QUENCHED CALCIUM DOPED SAMPLES

QUENCHING TEMPERATURE = 550C

Scattering data from MB spectrometer

Conc.(mppm)	Scat Ratio	Error in S.R.
255.0	0.350E+01	0.600E+00
249.0	0.280E+01	0.600E+00
243.0	0.270E+01	0.600E+00
312.0	0.490E+01	0.700E+00
300.0	0.580E+01	0.700E+00
288.0	0.490E+01	0.700E+00
416.0	0.460E+01	0.800E+01
395.0	0.360E+01	0.800E+01
374.0	0.200E+02	0.800E+01
579.0	0.119E+02	0.400E+01
543.0	0.470E+01	0.400E+01
514.0	0.330E+01	0.400E+01

ANNEALED CADMIUM DOPED SAMPLES

Scattering data from MB spectrometer

Conc.(mppm)	Scat Ratio	Error in S.R.
0.8	0.159E+03	0.210E+02
0.8	0.118E+03	0.210E+02
0.8	0.128E+03	0.210E+02
1.2	0.811E+03	0.145E+03
1.2	0.964E+03	0.145E+03
1.2	0.110E+04	0.145E+03
1.5	0.350E+04	0.400E+03
1.4	0.320E+04	0.400E+03
1.3	0.390E+04	0.400E+03
2.5	0.670E+04	0.800E+03
2.3	0.610E+04	0.800E+03
2.1	0.520E+04	0.800E+03
5.0	0.117E+05	0.130E+04
4.6	0.109E+05	0.130E+04
4.2	0.920E+04	0.130E+04
3.5	0.174E+05	0.410E+04
3.0	0.136E+05	0.410E+04
2.6	0.920E+04	0.410E+04
14.9	0.480E+05	0.100E+05
14.4	0.520E+05	0.100E+05
13.9	0.670E+05	0.100E+05

QUENCHED CADMIUM DOPED SAMPLES

QUENCHING TEMPERATURE = 350C

Scattering data from MB spectrometer

Conc.(mppm)	Scat Ratio	Error in S.R.
0.8	0.380E+01	0.300E+01
0.8	0.270E+01	0.300E+01
0.8	0.860E+01	0.300E+01
1.2	0.310E+01	0.140E+01
1.2	0.370E+01	0.140E+01
1.2	0.580E+01	0.140E+01
1.5	0.123E+02	0.470E+01
1.4	0.910E+01	0.470E+01
1.3	0.183E+02	0.470E+01
2.5	0.806E+02	0.410E+02
2.3	0.165E+02	0.410E+02
2.1	0.916E+02	0.410E+02
5.0	0.341E+03	0.131E+03
4.6	0.792E+02	0.131E+03
4.2	0.200E+03	0.131E+03
3.5	0.369E+03	0.142E+03
3.0	0.134E+03	0.142E+03
2.6	0.113E+03	0.142E+03
14.9	0.770E+04	0.160E+04
14.4	0.450E+04	0.160E+04
13.9	0.580E+04	0.160E+04

ANNEALED LEAD DOPED SAMPLES

Scattering data from MB spectrometer

Conc.(mppm)	Scat Ratio	Error in S.R.
0.3	0.110E+01	0.300E+00
1.1	0.300E+01	0.100E+01
5.7	0.250E+01	0.100E+01
14.0	0.360E+01	0.700E+00
15.0	0.900E+01	0.300E+01
118.0	0.215E+05	0.170E+05
115.0	0.240E+05	0.170E+05
112.0	0.520E+05	0.170E+05
143.0	0.480E+05	0.230E+05
137.0	0.160E+05	0.230E+05
1.6	0.470E+01	0.600E+00

QUENCHED LEAD DOPED SAMPLES

QUENCHING TEMPERATURE = 550C

Scattering data from MB spectrometer

Conc.(mppm)	Scat Ratio	Error in S.R.
0.3	0.820E+01	0.200E+01
5.7	0.360E+01	0.140E+01
1.1	0.600E+01	0.210E+01
15.0	0.900E+01	0.310E+01
14.0	0.910E+01	0.410E+01
118.0	0.155E+02	0.600E+01
115.0	0.540E+01	0.600E+01
112.0	0.520E+01	0.600E+01
143.0	0.630E+01	0.600E+00
132.0	0.540E+01	0.600E+00
310.0	0.285E+02	0.860E+01
287.0	0.136E+02	0.860E+01
265.0	0.135E+02	0.860E+01
1.6	0.112E+02	0.600E+01

QUENCHED LEAD DOPED SAMPLES

QUENCHING TEMPERATURE = 350C

Scattering data from MB spectrometer

Conc.(mppm)	Scat Ratio	Error in S.R.
0.3	0.180E+01	0.800E+00
0.2	0.290E+01	0.800E+00
5.7	0.120E+01	0.200E+00
5.7	0.140E+01	0.200E+00
1.1	0.650E+01	0.700E+00
1.0	0.550E+01	0.700E+00
16.0	0.290E+01	0.200E+00
14.0	0.260E+01	0.200E+00
16.0	0.520E+01	0.600E+00
13.0	0.440E+01	0.600E+00
118.0	0.420E+01	0.900E+00
112.0	0.290E+01	0.900E+00
143.0	0.310E+01	0.300E+00
132.0	0.350E+01	0.300E+00
310.0	0.103E+03	0.680E+02
265.0	0.730E+01	0.680E+02
1.6	0.110E+02	0.200E+01
1.4	0.820E+01	0.200E+01

QUENCHED LEAD DOPED SAMPLES

QUENCHING TEMPERATURE = 200C

Scattering data from MB spectrometer

Conc.(mppm)	Scat Ratio	Error in S.R.
0.3	0.200E+01	0.100E+00
0.2	0.210E+01	0.100E+00
5.7	0.700E+00	0.200E+00
5.7	0.100E+01	0.200E+00
1.1	0.240E+01	0.400E+00
1.0	0.190E+01	0.400E+00
16.0	0.310E+01	0.200E+00
14.0	0.340E+01	0.200E+00
16.0	0.290E+01	0.100E+00
13.0	0.270E+01	0.100E+00
118.0	0.290E+04	0.100E+03
112.0	0.270E+04	0.100E+03
143.0	0.310E+04	0.160E+04
132.0	0.540E+04	0.160E+04
310.0	0.134E+05	0.400E+04
265.0	0.770E+04	0.400E+04
1.6	0.270E+01	0.600E+00
1.4	0.350E+01	0.600E+00

ANNEALED LEAD DOPED SAMPLES

Scattering data from SP spectrometer

Conc.(mppm)	Scat Ratio	Error in S.R.
287.0	0.130E+06	0.150E+05
140.0	0.410E+05	0.500E+04
115.0	0.190E+05	0.230E+04
90.0	0.430E+04	0.100E+04
58.0	0.200E+04	0.100E+04

ANNEALED CADMIUM DOPED SAMPLES

Scattering data from SP spectrometer

Conc.(mppm)	Scat Ratio	Error in S.R.
9.5	0.480E+05	0.600E+04
7.3	0.320E+05	0.400E+04

QUENCHED CADMIUM DOPED SAMPLES

QUENCHING TEMPERATURE = 550C

Scattering data from SP spectrometer

Conc.(mppm)	Scat Ratio	Error in S.R.
7.3	0.130E+04	0.100E+04
9.5	0.170E+04	0.100E+04